2022

Forged by giants: understanding the dwarf carbon stars

BOSTON UNIVERSITY

GRADUATE SCHOOL OF ARTS AND SCIENCES

Dissertation

FORGED BY GIANTS:
UNDERSTANDING THE DWARF CARBON STARS

by

BENJAMIN R. ROULSTON

B.S., Clarkson University, 2016
M.A., Boston University, 2018

Submitted in partial fulfillment of the

requirements for the degree of

Doctor of Philosophy

2022

Approved by

First Reader

J.J. Hermes, PhD
Assistant Professor of Astronomy

Second Reader

Paul J. Green, PhD
Astrophysicist
Smithsonian Astrophysical Observatory

Third Reader

Philip Muirhead, PhD
Associate Professor of Astronomy

This dissertation is dedicated to my childhood self, who spent the nights with stars in his eyes dreaming of what the future would hold.

Acknowledgments

First and foremost, I thank my wife, Katelyn. Without your support, I would never have been able to finish my Ph.D. You gave me a great deal of wisdom (and tough love) through every hiccup in my research and every rut I got in. You proofread more astronomy papers than most people outside the field could say, and I forever count that part of this Ph.D. is due to you.

Next, I want to thank Paul Green, my advisor at the Smithsonian Astrophysical Observatory. When I was a lowly first-year graduate student, I reached out to Paul, desperate to work on research I found exciting. He took me in, gave me two different projects, and helped me become the scientist I am today. Paul was invaluable for my success today, and I thank him for introducing me to dwarf carbon stars.

I also want to thank my BU advisor, J.J. Hermes. He brought me into his group, and his perspective has encouraged me to think about my projects in a new way, expanding past my original narrow field of research.

I thank my parents, for whom it probably feels like I have been in school for far too long. Regardless, you have always supported me in whatever paths I have chosen. As a child, you were my first support, letting me succeed without ever pressuring me to do better or more. If not for your pure support, I would never have been able to get here today. Thank you, Mom and Dad.

Finally, I must thank Katelyn again. Your support has kept me focused, determined, and balanced every day of these past six years. You are the most extraordinary person I know, and you outshine every star.

FORGED BY GIANTS:
UNDERSTANDING THE DWARF CARBON STARS

BENJAMIN R. ROULSTON

Boston University, Graduate School of Arts and Sciences, 2022

Major Professor: J.J. Hermes, Assistant Professor of Astronomy

ABSTRACT

Dwarf carbon (dC) stars are main-sequence stars with carbon molecular bands (C_2, CN, CH) in their optical spectra. They are an important class of post-mass transfer binaries since, as main-sequence stars, dCs cannot have produced carbon themselves. Rather, the excess carbon originated in an evolved companion, now a white dwarf, and was transferred to the dC. Because of their complex histories, dCs are an excellent sample for testing stellar physics, including common-envelope evolution, wind accretion, mass transfer efficiencies, and accretion spin-up. However, their fundamental properties remain a mystery, and this impedes efforts to use dCs to constrain the evolution of binary systems.

Here, I have investigated the observed properties of dCs, both as a population and as individual objects. Using multi-epoch spectroscopy, I constrained the dC binary fraction to be consistent with 100% binarity. The best-fit orbital separation distribution agrees with the few known dC orbital periods, and suggests a bimodal distribution (one sample with mean periods of hundreds of days, the other thousands of days). I also built a set of optical templates to find and classify additional dCs in spectroscopic surveys.

Further, I discovered periodic variability in photometry of 34 dCs, dramatically

increasing the number of measured periods. This allowed me to investigate mass transfer mechanisms that are likely to be important in the formation of dCs. Interestingly, some of these objects have short periods ($P < 2d$), indicating they have gone through a common-envelope phase. I explored the implications of these short-period dCs and how they will allow for constraints to be placed on the physics of common-envelope evolution.

Finally, I searched for signs of spin-up and activity in dCs using X-ray emission. From this, I found that dCs are consistent with being rapid rotators, similar to what is observed in samples of normal young dwarfs.

In summary, this dissertation presents the most extensive set of dC observational properties that has been compiled to date. I have confirmed the binary origin of dCs and linked some to post-common-envelope binaries. My work has provided a firmer foundation for the use of dCs to explore many essential astrophysical phenomena.

Contents

Dedication **iv**

Acknowledgements **v**

Abstract **vi**

List of Tables **xii**

List of Figures **xiii**

List of Abbreviations **xv**

1 Introduction **1**

1.1 Motivation 1

1.2 Binary Stars 2

1.2.1 Mass Transfer 3

1.2.2 Common-Envelope Evolution 6

1.3 Dwarf Carbon Stars 7

1.3.1 Binary Formation of dCs 11

1.3.2 Properties of dC Stars 13

1.4 Goals and Outline 15

1.5 Summary 17

2 Radial Velocity Variations of Dwarf Carbon Stars **18**

2.1 Motivation . . . 18
2.2 Dwarf Carbon Star Sample Selection . . . 19
2.3 Control Sample Selection . . . 23
2.3.1 Selection Criteria . . . 23
2.3.2 Property Matching . . . 23
2.3.3 Control Sample Issues . . . 24
2.4 Radial Velocity Analysis . . . 27
2.4.1 Cross-Correlation Method . . . 27
2.4.2 Cross-Correlation Errors . . . 28
2.4.3 dC and Control ΔRVs . . . 31
2.5 Statistical Comparison of ΔRV Distributions . . . 40
2.5.1 Anderson-Darling Test . . . 40
2.5.2 Extreme Deconvolution . . . 40
2.6 Binary Orbit Simulations . . . 43
2.7 Balmer Emission Lines . . . 48
2.8 Discussion . . . 50
2.9 Summary . . . 52

3 Photometrically Variable Dwarf Carbon Stars 53

3.1 Motivation . . . 53
3.2 Sample Selection . . . 56
3.3 Light Curve Processing . . . 57
3.4 Periodic Variability . . . 58
3.5 Spectroscopic Follow-up . . . 69
3.5.1 Spectroscopic Set-Up . . . 69
3.5.2 SDSS J151905.96+500702.9 . . . 70

3.5.3 SDSS J123045.53+410943.8 75
3.5.4 SBSS 1310+561 77
3.5.5 LAMOST J062558.33+023019.4 78
3.6 Common Envelope Connection 79
3.6.1 Binary Population Synthesis Models 81
3.6.2 BPS Comparison to Observed dC Sample 82
3.7 Summary 92
3.8 Summary 94

4 X-ray Properties of the Nearest Dwarf Carbon Stars 95
4.1 Motivation 95
4.2 Sample Selection 98
4.3 X-Ray Observations and Analysis 101
4.3.1 Individual Spectral Fits 104
4.3.2 X-ray Variability 108
4.3.3 Rotation-Activity Relationship 112
4.4 J0435 Spectral Energy Distribution 117
4.5 Discussion 122
4.6 Summary 126

5 Empirical Spectral Templates for Dwarf Carbon Stars and DA White Dwarfs 128
5.1 Motivation 128
5.2 PyHammer 131
5.2.1 PyHammer v1.0 131
5.2.2 PyHammer v2.0: SB2 132

5.3 Carbon Star and White Dwarf Templates 133
5.3.1 Carbon Star Templates 133
5.3.2 WD Templates 135
5.3.3 PyHammer Spectral Indices 138
5.4 Luminosity Stellar Templates 140
5.5 Spectroscopic Binary Templates 143
5.5.1 SB2 Radial Velocities 145
5.6 Accuracy 146
5.7 Updated PyHammer GUI 152
5.8 Discussion 155
5.9 Summary 157

6 Summary and Future Work **159**
6.1 Summary of Work 159
6.2 Future Work 164
6.3 Concluding Remarks 167

References **170**

Curriculum Vitae **185**

List of Tables

2.1 dC ΔRV Sample Properties 38

2.2 Control Sample ΔRV Properties 39

2.3 XD-GMM Component Fits 41

3.1 Light Curve Statistics of Selected dC Sample 57

3.2 Periodic dC Light Curve Properties 65

3.3 Properties of the WD in J1519 71

3.4 Radial Velocity Fits of Periodic dCs 79

3.5 Periodic dC Parallaxes, Distances, and Estimated Physical Parameters 85

4.1 Parallaxes, Distances and Bolometric Luminosities for Selected X-ray dCs 100

4.2 *Chandra* X-ray Observations Properties 103

4.3 J0435 Individual X-ray Model Fits 108

4.4 J0435 Fit X-ray Source Flux 108

5.1 Properties of dC Spectral Templates 133

5.2 Properties of DA WD Spectral Templates 137

5.3 New Spectral Indices for stellar classification 141

5.4 Accuracy of SB2 classifications in PyHammer 154

List of Figures

1.1 Bondi-Hoyle-Lyttleton Accretion Schematic 4

1.2 Wind-RLOF Schematic 5

1.3 TP-AGB Structure 8

1.4 AGB Thermal Pulse Diagram 10

2.1 r mag versus signal to noise for dC sample 22

2.2 Histograms of dC sample properties 25

2.3 Histogram of "multi-shift" Errors 29

2.4 Comparison of `FXCOR`-reported Errors to "multi-shift" Errors 30

2.5 dC RV Errors vs. r mag 32

2.6 Comparison of the dC RV Distribution to the Control Sample 34

2.7 Critical Period for RLOF for Varying dC Masses 36

2.8 Spectral Overplot for the dC with the Largest ΔRV 37

2.9 XD-GMM for the dC and Control Samples 42

2.10 MCMC of dC Orbital Fits for Unimodal log-normal Distribution . . . 46

2.11 MCMC of Control Orbital Fits for Unimodal log-normal Distribution 47

2.12 Corner Plot for Bimodal Separation MCMC Fit. 49

3.1 Light Curves and Power Spectra for Periodic dCs 60

3.2 SDSS Spectrum for SDSS J151905.96+500702.9 with RVs, Hα Equivalent Widths and Model Fits 73

3.3 SDSS Spectrum for SDSS J123045.53+410943.8 with RVs, Hα Equivalent Widths and Model Fits 75
3.4 Binary Population Syntheses Models for PCEB dCs with Model $\alpha\alpha$2 88
3.5 Binary Population Syntheses Models for PCEB dCs with Model $\alpha\alpha$. 90

4.1 Toomre Diagram for dCs 97
4.2 Color-magnitude diagram for Chemically Enhanced Stars 102
4.3 X-ray Spectrum and Fit for SBSS1310 105
4.4 X-ray Spectra and Model Fits for J0435 107
4.5 X-ray Model Fit Parameters for J0435 109
4.6 Unabsorbed Model Fluxs for J0435 110
4.7 ZTF Light Curves for J0435 113
4.8 X-ray Activity-Rotation Diagram for dCs 115
4.9 Spectral Energy Distribution and Fit for J0435 120

5.1 PyHammer Spectral Templates for dCs 136
5.2 PyHammer Spectral Templates for DA WDs 139
5.3 Physical Luminosity Spectral Templates 144
5.4 PyHammer Classification Accuracy 148
5.5 PyHammer SB2 Classification Accuracy 150
5.6 PyHammer SB2 Classification Confusion Matrix 153
5.7 PyHammer SB2 GUI 156

List of Abbreviations

ACS ..... Advanced Camera for Surveys

AGB ..... Asymptotic Giant Branch

APOGEE ..... Apache Point Observatory Galactic Evolution Experiment

AFD ..... Automatic Fourier Decomposition

BHL ..... Bondi-Hoyle-Lyttleton

BIC ..... Bayesian Information Criterion

BPS ..... Binary Population Synthesis

CE ..... Common-Envelope

CEE ..... Common-Envelope Evolution

CEMP ..... Carbon-Enhanced-Metal-Poor

dC ..... dwarf carbon star

Decl. ..... Declination

eBOSS ..... extended Baryon Acoustic Oscillation Sky Survey

FAP ..... False-Alarm Probability

FES ..... Few-Epoch Spectroscopy

FUV ..... Far-Ultraviolet

GUI. ..... Graphical User Interface

GMM ..... Gaussian Mixture Mode

HST ..... Hubble Space Telescope

IR ..... Infrared

KDE ..... Kernel Density Estimation

LAMOST ..... Large Sky Area Multi-Object Fiber Spectroscopic Telescope

LISA ..... Laser Interferometer Space Antenna

LS ..... Lomb-Scargle Periodogram

MCMC ..... Markov Chain Monte Carlo

MJD ..... Modified Julian Date

NUV ..... Near-Ultraviolet

PCEB ..... Post-Common-Envelope Binary

R.A. ..... Right ascension

RLFF ..... Roche-lobe Filling Factor

RLOF ..... Roche-lobe Overflow

RV ..... Radial Velocity

SB2 ..... Double-lines Spectroscopic Binary

sdB ..... subdwarf-B star

SES ..... Single-Epoch-Spectroscopy

SDSS ..... Sloan Digital Sky Survey

SED ..... Spectral Energy Distribution

TDSS ..... Time-Domain Spectroscopic Survey

TP-AGB ..... Thermally Pulsing Asymptotic Giant Branch

WD ..... White Dwarf

WFC3 ..... Wide Field Camera 3

wind-RLOF ..... Wind-Roche-lobe Overflow

XD ..... Extreme Deconvolution

ZTF ..... Zwicky Transient Facility

2MASS ..... Two Micron All Sky Survey

Chapter 1

Introduction

1.1 Motivation

Peculiar phenomena can often give insight into new and interesting physics and aid in our understanding of current problems in astronomy. This is often the result of research in a niche field that ends up with implications broader than intended and can be key to advancing outstanding problems.

This dissertation is one such culmination of research. At the onset of this work, the aim was to provide some new insights and constraints on dwarf carbon stars. However, as that study began revealing new results (which are interesting in their own right), it became clear that there was more to these dwarf carbon stars than initially assumed.

Expanding the original research scope and including new data and techniques led to the realization that these dwarf carbon stars could prove useful in the understanding of many important astrophysical phenomena (e.g., common-envelope evolution, wind-Roche Lobe overflow, mixing in stellar envelopes, and stellar spin-up and rejuvenation).

The research detailed in Chapters 2–5 builds and expands on the known properties of dwarf carbon stars. I provide the first constraints on the dwarf carbon star binary fraction and orbital separations, expand the known dwarf carbon star periods, and

examine the rapid rotation of dwarf carbon stars by studying their X-ray properties. I connect these results together and provide the support that some dwarf carbon stars are a new and exciting class of post-common-envelope binaries. A dwarf carbon star has the advantage that even without the white dwarf visible in the optical spectrum, we know it is in a binary system since the carbon bands are signs of obvious chemical enrichment. I make the case that dwarf carbon stars are a key sample where we can, for the first time, connect the pre- to post-common-envelope phases as is needed to understand the remarkable yet still poorly understood common-envelope evolution.

The rest of this chapter is devoted to providing background information related to the science and research of this dissertation. I describe the basics of single-star evolution, tracking the structural and chemical evolution as a star evolves off the main sequence to its end of life. I describe binary star systems and how their evolution can be quite different than that of the single star case. Finally, I introduce the dwarf carbon stars. I describe their history, formation theory, and known properties, as well as outstanding questions. Finally, in Section 1.4 I describe the motivating questions of this dissertation and how I have addressed those in the following chapters.

1.2 Binary Stars

Multiple star systems are ubiquitous in the Universe. Recent studies have put the multiplicity fraction of solar-like stars near 50% (Raghavan et al., 2010; Moe & Di Stefano, 2017). This multiplicity decreases toward later types, reaching 27% for M-dwarfs (Winters et al., 2019). Binary stars are the simplest of these multiple systems to study and can provide a plethora of physical insight into stellar astrophysics.

Many interesting astrophysical phenomena are the result of binary systems and their interactions, and this keeps binary stars a persistent field of research. Cata-

clysmic variables, Type Ia supernova, common-envelope evolution, and future potential Laser Interferometer Space Antenna (LISA; Amaro-Seoane et al., 2017) galactic gravitational wave sources are a few examples of current, high-interest binary star research topics.

What makes binary stars so useful and interesting is their ability to interact and the plethora of phenomena thereby generated. These interactions can be dynamical, changing the orbital parameters or the rotation of the components. The interactions can also be direct through mass transfer. More often than not, it is a combination of these two types that are involved in the evolution of a binary. Mass transfer is particularly interesting as it can not only lead to dynamical interactions but it can result in both structural and chemical changes of the accreting star.

1.2.1 Mass Transfer

Mass transfer is commonly categorized into four main types: Bondi-Hoyle-Lyttleton accretion (BHL; Hoyle & Lyttleton, 1939; Bondi & Hoyle, 1944), wind-Roche lobe overflow (wind-RLOF; Mohamed & Podsiadlowski, 2007), Roche-lobe overflow (RLOF; Paczyński, 1971), and via a common envelope (Paczynski, 1976). These are listed in order of increasing interaction, and some binaries may experience all four as the interactions lead to a shrinking of the orbit.

In BHL accretion (sometimes referred to as wind accretion), the donor provides a fast wind (at least the wind speed is much larger than the orbital velocity of the companion). This wind is assumed to be uniform in density and cold around the region of the accretor. As this material passes the accretor, it is gravitationally attracted and focused into an accretion line onto the accretor. Figure 1.1 shows a schematic of BHL accretion, including the paths of test particles.

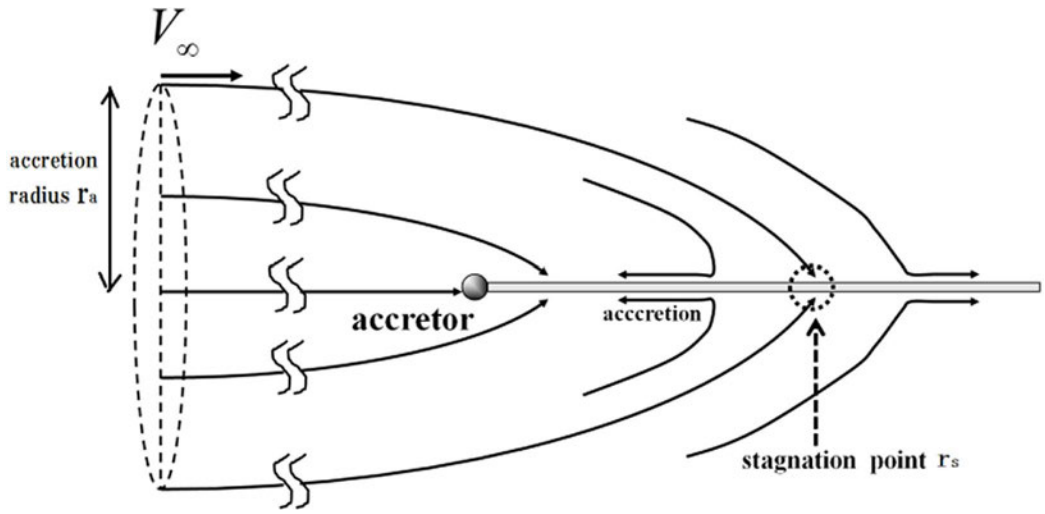

Figure 1.1: Schematic of Bondi-Hoyle-Lyttleton accretion reproduced from Ohsugi (2018) Figure 1. In the BHL accretion formalism, the donor wind provides the material to be accreted, with a wind speed much larger than that of the accretor orbital speed. BHL accretion assumes uniformly distributed cold gas, which, as it passes the accretor, is gravitationally attracted to the accretor. The material builds behind the accretor and is then accreted.

Note that the BHL accretion case is applicable only in the regime where the donor wind speed is much larger than that of the orbital speed. This is true in wide binaries that have long orbital periods (i.e., small orbital velocities). BHL accretion has the lowest accretion efficiencies of the four types considered in this chapter. See Matsuda et al. (2015) and Ohsugi (2018) for a detailed review and analysis of BHL accretion.

The wind-RLOF mode of mass transfer is similar to BHL accretion but describes the case where the wind speed is comparable to the orbital velocity. This is often the case in binary systems where the donor is an evolved asymptotic giant branch (AGB) star. AGB stars often have slow (but massive) winds with velocities of 5–30 $\mathrm{km\,s^{-1}}$ (Habing & Olofsson, 2004). These wind speeds are easily comparable to the orbital periods in binaries with separations between 3 AU and 110 AU, wide enough to avoid a common envelope during the red giant branch phase.

In the wind-RLOF case, the wind acceleration radius is beyond the Roche-lobe

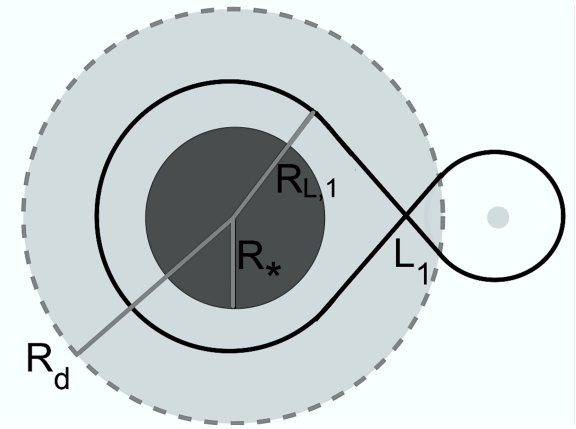

Figure 1.2: Schematic of wind-RLOF reproduced from Abate et al. (2013) Figure 1. Here R_* is the stellar radius, $R_{L,1}$ is the Roche lobe radius of the primary, R_d is the wind acceleration radius (corresponding to the dust formation radius in AGB stars), and L_1 is the inner Lagrangian point. In the wind-RLOF prescription, R_d is larger than $R_{L,1}$, causing the slow wind to be gravitational bound, leading to a focusing of the wind to the orbital plane and through L_1 onto the companion. Note that as the dust condensation temperature of carbon-rich dust is higher than that of oxygen-rich dust, R_d is closer to $R_{L,1}$ in AGB stars with $C/O > 1$.

of the donor star. The wind is bound to the donor, and can be gravitationally focused through the inner Lagrangian point and then accreted onto the companion star (a schematic can be seen in Figure 1.2). This allows wind-RLOF mass transfer to have accretion efficiencies much higher than the BHL accretion case. Simulations have shown that wind-RLOF in binaries with AGB primaries can have mass-transfer efficiencies of 40-50% (Abate et al., 2013; Saladino et al., 2018, 2019; Saladino & Pols, 2019). Wind-RLOF has also been shown to efficiently tighten the orbit (Saladino et al., 2018; Chen et al., 2018) so that more systems can be driven towards shorter periods and possibly evolve into a RLOF state.

Near the end of stellar evolution (e.g., AGB phase), a star can evolve past its Roche-lobe, the surface which separates material bound and unbound to the star. If the evolving star expands past the Roche-lobe, the material can be lost through the inner and outer Lagrangian points. If the material is lost through the inner

Lagrangian point (L_1 in Figure 1.2), it can be accreted by a binary companion. This is the RLOF case, which can either be stable or unstable depending on how both the donor star's Roche-lobe and radius adjust to the mass loss. The mass transfer can be unstable if the donor star's radius expands faster than its Roche lobe or if the donor star's radius shrinks slower than its Roche lobe. The unstable mass transfer will cause the orbit to shrink in an accelerating fashion. This will eventually lead to a common envelope.

1.2.2 Common-Envelope Evolution

RLOF is just one instability that can lead to the shortening of the orbital period to the extent that the companion star can enter the envelope of the more-evolved companion, where the cores orbit each other in a common envelope (CE; Paczynski, 1976; Ivanova et al., 2013). Common-envelope evolution (CEE) is a critical yet poorly understood process in the formation of many important astrophysical phenomena (e.g., gravitational wave sources, white-dwarf mergers, cataclysmic variables). As the companion is submerged in the envelope, it experiences drag and can transfer orbital energy and angular momentum into the envelope gas. The orbit thereby shrinks, bringing the cores closer together and, in theory, eventually ejecting the common envelope material. If the envelope is ejected before the cores merge, the resulting binary will have a substantially shortened period. This can be seen in many of the known types of short (and ultra-short) period systems. These include X-ray binaries, cataclysmic variables, AM CVn stars, white-dwarf mergers, some Type Ia supernovae, and most binaries with periods less than a few days.

CEE is still poorly understood, and there remain many open questions on the processes involved throughout the evolution itself. Theory and simulations have yet

to identify how the envelope can be completely ejected, and the source of the needed additional energy has not yet been successfully determined (Ivanova et al., 2013). Recent studies have used 3D hydrodynamic simulations to probe the physics of the CE, but the range of timescales and magnitudes involved make continuous simulations of the full CE computationally impossible (Ohlmann et al., 2016a,b; MacLeod et al., 2018b,c; Chamandy et al., 2018, 2020; MacLeod et al., 2022).

This is especially true of CE simulations with an AGB primary. There have been a few simulations of CE with an AGB star (e.g., Sand et al., 2020), but the increased size of the AGB radius only exacerbates the computational difficulties. However, these evolved AGB stars are likely crucial to understanding not only CEE, but the formation of many of the chemically enhanced stars.

1.3 Dwarf Carbon Stars

While the majority of stars exhibit similar elemental abundances, there are a variety of ways in which some stars can become chemically peculiar. An example of extrinsically formed peculiar stars are the subdwarf-B (sdB) stars, which are helium core burning stars with almost no hydrogen (Heber, 1986). These are thought to be formed via binary interactions in which the hydrogen envelope of a red giant branch star is removed (Maxted et al., 2001) leaving the helium core visible.

Stars can also be enhanced by internal processes if fusion products from the core can be brought to the surface, changing the observed composition. Examples include the so-called dredge-ups, which can happen at various stages of stellar evolution. The primary one I consider here is the third dredge-up near the end of the AGB phase.

AGB stars have a degenerate CO core with double fusion shells (moving outward from the core) of helium and hydrogen, as shown in Figure 1.3. As the hydrogen

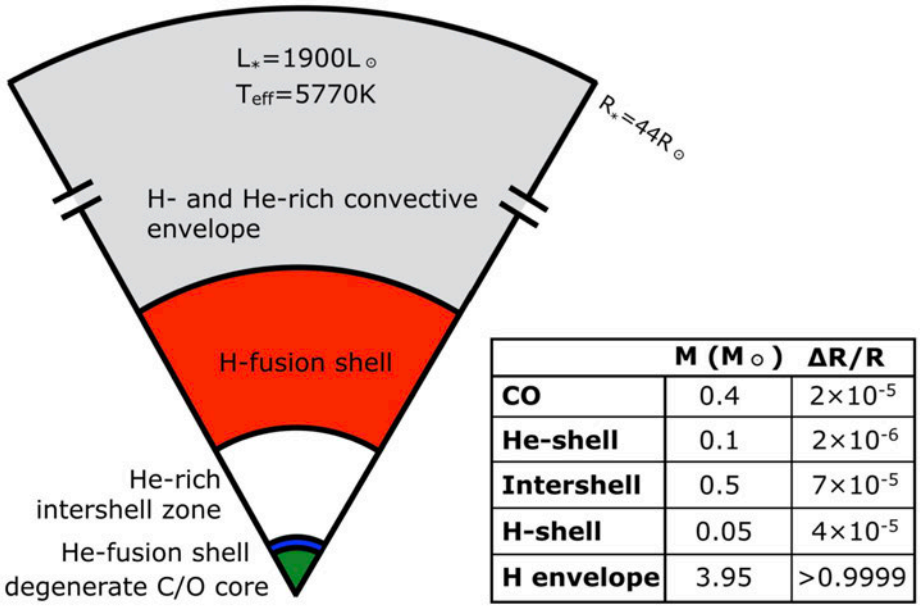

	M (M⊙)	ΔR/R
CO	0.4	2×10^{-5}
He-shell	0.1	2×10^{-6}
Intershell	0.5	7×10^{-5}
H-shell	0.05	4×10^{-5}
H envelope	3.95	>0.9999

Figure 1.3: TP-AGB stellar structure schematic reproduced, with permission of IOP Publishing Limited through PLSclear, of Figure 18.1 from *Understanding Stellar Evolution* (Lamers & M. Levesque, 2017). In a TP-AGB star there is a degenerate CO core surrounded by a helium fusion shell. Above this shell is the helium rich intershell region, followed above by the larger hydrogen fusion shell. Note that all of these regions together represent about a hundredth of a percent of the total stellar radius at this stage.

shell (which produces most of the energy) continues to fuse H into He, the helium shell surrounding the core continues to grow. Eventually, the helium shell experiences runaway fusion, driving the expansion of the envelope material above.

This He-shell "flash" and expansion means the star is now in the thermally pulsing AGB (TP-AGB) phase. Helium shell fusion causes the inter-shell region to become strongly convective, dredging helium fusion products to the surface, i.e., the third dredge-up. As the expansion continues, the pressure in the helium shell will drop, eventually stopping its energy production. The layers contract again with hydrogen shell fusion resuming, and the cycle repeats. Figure 1.4 gives a schematic overview of this pulse cycle.

Each successive thermal pulse becomes stronger, reaching deeper into the intershell zone, and the stellar radius increases (Iben & Renzini, 1983). As helium shell fusion products are brought to the surface, it is possible that the envelope carbon abundance increases until C/O > 1 (for reference, the Sun has C/O ≈ 0.6; Asplund et al., 2021). Since C preferentially binds with O in the form of CO, C_2 and CN bands only appear when C/O> 1, forming a giant C star (see Wallerstein & Knapp (1998) and Lloyd Evans (2010) for two detailed reviews on C stars).

Only stars with initial masses in the range $\sim 2-4M_{\odot}$ may become a C star during part of their TP-AGB phase (Kalirai et al., 2014). It has therefore been assumed that all C stars are giants currently in their TP-AGB phase and have dredged up carbon produced in their cores, polluting their atmospheres with an atmospheric C/O ratio above unity. This made it quite surprising when Dahn et al. (1977) found the first *main-sequence* C star, G77-61. G77-61 is characterized by the typical C star bands of C_2 and CN, indicating atmospheric C/O > 1.

A dwarf carbon (dC) star cannot have yet experienced fusion to create C enhance-

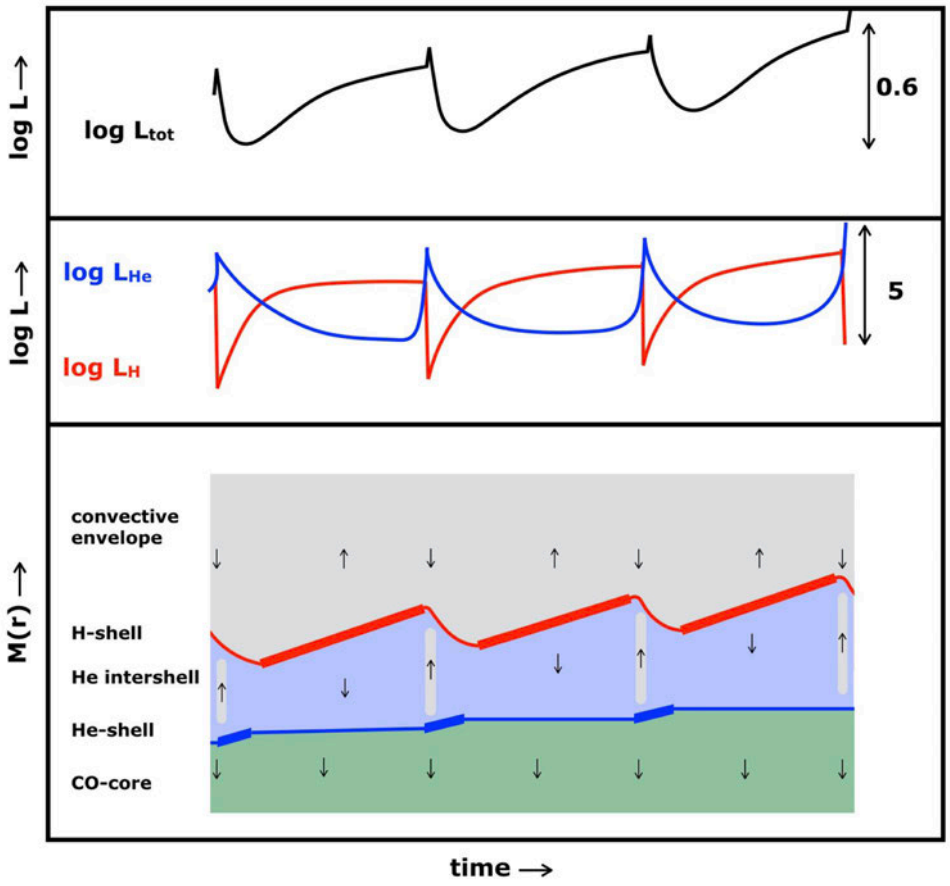

Figure 1.4: Schematic of thermal pulses during the TP-AGB reproduced, with permission of IOP Publishing Limited through PLSclear, of Figure 18.3 from *Understanding Stellar Evolution* (Lamers & M. Levesque, 2017). The top panel shows the change in the total luminosity across a few pulse cycles. The middle panel shows the luminosity from each of the hydrogen and helium fusion shells. The bottom panel shows the details of the thermal pulses in an AGB star. The degenerate CO core is in green, with the helium shell in blue and the hydrogen shell in red. The thick lines for the shells show what is dominant at that time. The light purple is the intershell region, and regions shaded in grey are convective, with arrows indicating the expansion or contraction of each region. During a thermal pulse the helium shell dominates the energy production leading to an expansion of the intershell region and convection that can bring helium fusion products to the surface convective region.

ment, or the third dredge-up, since it is a main-sequence star. Dahn et al. (1977) put forth a few explanations of this C enhancement on the main sequence, with the favored being that G77-61 was in a binary system and had experienced C-enhanced mass transfer. Today, G77-61 is no longer the only known dC, with close to 1000 known in the literature. The majority of these dCs come from the Green (2013) and Si et al. (2014) samples, which were found from all-sky spectroscopic surveys.

1.3.1 Binary Formation of dCs

In the mass transfer formation scenario, the progenitor of the currently observed dC is in a binary system with a more massive star that evolved through the TP-AGB phase. This TP-AGB star experienced intrinsic carbon enhancement and became a giant C star itself. The AGB C star has a massive, slow, carbon-enhanced wind that can be accreted by the dC progenitor, bringing its C/O > 1 and forming a dC. The TP-AGB companion then evolves further, expelling its envelope via a wind, leaving behind its CO core as a white dwarf (WD). The WD then cools over gigayear time scales, usually beyond detection in optical spectra (Dahn et al., 1977; Dearborn et al., 1986).

Indeed, this mass-transfer scenario became the preferred theory when Dearborn et al. (1986) found G77-61 to be a radial velocity (RV) binary with an orbital period of 245.5 d. Since then, there have been almost a dozen "smoking gun" systems found in which the WD companion is sufficiently hot to be visible in the optical spectra as a spectroscopic composite (Heber et al., 1993; Liebert et al., 1994; Green, 2013; Si et al., 2014).

The requirement for a dC to be formed via mass transfer from a late AGB star suggests that BHL accretion or wind-RLOF is primarily responsible for their for-

mation. This is because wind-RLOF is easiest in binaries with an evolved AGB component. Indeed, many of the other known chemically peculiar stars have had their observed formation rates reproduced well by considering wind-RLOF. Abate et al. (2013) performed simulations of the formation of the carbon-enhanced-metal-poor (CEMP) stars. CEMP stars are metal-poor ([Fe/H]< -1.0) stars with enhanced carbon ([C/Fe]> 0.7) (Aoki et al., 2007).

Saladino et al. (2019) and Saladino & Pols (2019) also performed simulations finding that AGB binaries with wind-RLOF were consistent with the observed properties of the CEMP, CH, and Ba stars. CH stars are subgiant and giant C stars with strong molecular CH bands, but otherwise weak metal lines (Jorissen et al., 2016). Ba stars (originally termed Ba II) are typically K-type giants with over-abundances of Ba and other *s*-process elements as well as slight (C/O ~ 1) carbon enhancement (Bidelman & Keenan, 1951; Merle et al., 2016).

All of these stars, including dCs, are the result of efficient mass transfer from an AGB companion. As main-sequence carbon-enhanced stars, dC are the most likely progenitors of the more evolved CEMP, CH, and possibly the Ba stars. These stars, being more luminous than dCs, have been studied via RV campaigns, which have shown increased binarity compared to normal O-rich stars, indicating they have likely also experienced mass transfer from an unseen companion (Sperauskas et al., 2016). Ba and CH stars show periods from RV analysis of 1–20 years (Escorza et al., 2019).

Blue straggler stars are another class similar to dCs in that they may have experienced mass transfer from a previous AGB companion. Blue straggler stars in a cluster color-magnitude diagram are more luminous and bluer than the main-sequence turnoff (e.g., Gosnell et al. 2019). While some are likely formed in mergers or collisions, most

blue straggler stars are thought, like dC stars, to be the result of mass transfer from a giant to a main-sequence dwarf. Most blue straggler stars are found in wide binaries with periods of order 1000 days, consistent with expectations of mass transfer from an AGB star onto a main-sequence companion (Chen & Han, 2008; Gosnell et al., 2014), which leaves a CO-core WD remnant (Paczyński, 1971). Those blue straggler stars that form after mass transfer from a red giant branch star typically have a shorter binary period (of order 100 days; Chen & Han, 2008) and a He-core WD companion. Chen & Han (2008) showed for some simulations that the companion can accrete up to $0.4\,M_{\odot}$. The salient point relevant to dC stars is that significant mass is typically gained in these encounters.

1.3.2 Properties of dC Stars

While dC stars are now known to be numerous, details of their properties remain sparse, especially compared to the other chemically enhanced stars mentioned above. This is especially true of their orbital properties. At the onset of this dissertation research, there were only six orbital periods for dCs in the literature. The first is of the dC prototype G77-61, found to be a single-line spectroscopic binary with an orbital period of 245.5 d (Dearborn et al., 1986). The central source of the Necklace Nebula was found to be a binary with a dC, which has a photometric period of 1.16 d (Corradi et al., 2011; Miszalski et al., 2013). The three longest period dCs in the literature are those from Harris et al. (2018) who found astrometric binaries with periods of 1.23 yr, 3.21 yr, and 11.35 yr. Most recently, Margon et al. (2018) found a dC with a photometric period of 2.92 d and confirmed this as the orbital period with spectroscopic follow-up.

de Kool & Green (1995) modeled the space density of dCs, and they predicted the dC period distribution to be bimodal, with peaks near 10^2–10^3 d and 10^3–10^5 d, consistent with the known periods listed above. de Kool & Green (1995) also found that the production of dCs is strongly dependent on metallicity, finding no dCs should be formed in systems with initial metallicity greater than half of solar (i.e. [Fe/H]>-0.3). This is in agreement with metallicity measurements of G77-61, where Plez & Cohen (2005) found [Fe/H] $= -4.0$, making G77-61 one of the lowest metallicity stars known. This also has been supported by Farihi et al. (2018) who used a combination of Sloan Digital Sky Survey (SDSS; York et al., 2000; Blanton et al., 2017) based RVs and *Gaia* DR1 proper motions and found that 30–60% of dCs to be halo objects, which are traditionally metal-poor.

The known dC periods span from ~ 1 d to ~ 4100 d, indicating different formation pathways. The longest dC periods that are of order 10s of years likely experienced only standard BHL accretion or wind-RLOF. These periods are consistent with other types of post-mass-transfer systems, such as the blue straggler stars. The dCs with current periods $\lesssim 10$ d would have likely experienced CEE since the TP-AGB envelope expands to several 100s of solar radii. However, what mass transfer mechanism is responsible for the formation of dCs, and how often, remains an open question. For example, how often do dCs experience a CE phase that results in a short period as seen in the dC from Margon et al. (2018)?

This is just one example of the dearth of known dC properties. In addition, there are no known eclipsing dC systems, corresponding to there being no dynamically measured dC masses. Masses can be estimated from color-magnitude fits, but these are based on normal O-rich type relations and may not be accurate for dCs. Currently,

there are no published model atmospheres for dCs[1]. There are no published dC C/O ratios and only one dC with a measured metallicity (G77-61; Plez & Cohen, 2005). Clearly, there is a need for a broad study of dC properties to fill the gaps in the understanding of their formation.

1.4 Goals and Outline

The goal of this dissertation is to provide the broadest understanding of dCs and their properties. This was done by using a variety of observational and computational techniques, which have addressed the following questions:

Questions 1, 2, and 3

1 What is the binary fraction of the dwarf carbon stars?

2 Are the orbital properties consistent with a single formation mechanism: carbon-enriched mass transfer?

3 What does the separation distribution imply for the mass transfer mechanisms that can form dwarf carbon stars, and in what systems can this occur?

These questions are addressed in Chapter 2 using spectroscopic data taken as part of the SDSS-IV's Time-Domain Spectroscopic Survey. Using repeat epochs of optical spectra, I construct a RV variation distribution for a sample of dCs. Fitting this distribution with binary star models, I infer the binary properties of the dC population.

[1]There are model atmospheres for *giant* C stars. The difference in surface gravity between these and dCs, together with the differing origin of their C/O ratios and evolutionary states, make them unsuitable for use in dC studies.

Question 4

4 What is the formation pathway for the extremely short period (P $<$ 1d) dCs?

Previously, there was a dearth of known orbital periods and solutions for dCs. This has made it hard to determine any conclusive evolutionary pathway for dCs. In Chapter 3, I use light curves from large photometric surveys to search for new dC periods, finding dozens more than previously known. Follow-up spectroscopic observations confirm two photometric periods as orbital periods, setting the stage for a new sample of post-common-envelope dCs.

Question 5

5 Do the X-ray properties of dCs show they have increased activity from mass transfer spin-up, or rather from tidal locking in close orbits?

I address this question in Chapter 4 by using *Chandra* observations of dCs. I search for signs of chromospheric activity and compare the observed sample of X-Ray emitting dCs to those with known periods from Chapter 3. The insight on short-period dCs from Chapter 3 provides a challenge in determining if accretion induced spin-up alone can rejuvenate dCs.

Question 6

6 How do the optical spectral features of dCs change with effective temperature, and how does this affect their detection?

There currently exists no published model atmospheres for dCs. However, there exist a large number of dC spectra in the SDSS at medium resolution. Using these spectra, I built a set of dC templates with high signal-to-noise based on their observed

spectral features. Using these templates, I also built a set of dC-WD spectroscopic binary templates for use in finding new composite binary dCs. Chapter 5 contains this work and compares the dCs to the normal (O-rich) spectral sequence relating to their temperatures.

1.5 Summary

This dissertation provides the largest and newest set of dC star properties, mainly focused on their binarity. While these results are interesting in the context of dC star formation, they prove to be interesting and applicable to a wider range of outstanding astrophysical problems. A few examples include studying and constraining wind-RLOF, CEE, stellar atmospheric mixing, and accretion induced spin-up. This dissertation provides the groundwork for a rich future of exploring dCs in the wider context of binary and stellar evolution.

Chapter 2

Radial Velocity Variations of Dwarf Carbon Stars

This chapter analyzes repeat spectroscopy of dCs from the SDSS-IV. Using these repeat spectra, I measure the RV variations for a large sample of dCs. I model these variations with a few binary star populations. From these models, I show that the best fitting model for the RV variations suggests a near 100% binary fraction for the dCs. In addition, my models produce estimated separation distributions of the dCs, using both single-peaked and bimodal distributions that correspond well to the known dC periods. The contents of this chapter have been published in Roulston et al. (2019).

2.1 Motivation

As discussed in Chapter 1, dCs are known to be numerous, but the details of their properties remain sparse. This is especially true of their orbital properties. As of the time of the research in this chapter, only six dCs had known periods, and of those, only four had a spectroscopic or astrometric orbital fit. Further confusing matters is that the six known dC periods span a large range of periods, from 4146 d (11.35 yr; Harris et al., 2018) down to 1.16 d (Miszalski et al., 2013).

This period span, from $\sim$ 1 d to $\sim$ 4100 d, suggests very different mass transfer

histories as well as orbital evolution differences. The longest dC periods that are of order tens of years likely experienced only standard RLOF or wind-RLOF. These periods are consistent with other types of post-mass-transfer systems, such as the blue straggler stars. The dCs with periods $\lesssim 10\,\mathrm{d}$ would have likely experienced CEE since the TP-AGB envelope expands to several hundred solar radii. However, which mass transform mechanism is responsible for the formation of dCs, and how often remains an open question. For example, how often do dCs experience a CE phase that results in a short period, as seen in the dC from Miszalski et al. (2013) and, Margon et al. (2018)?

In this chapter, I describe multi-epoch spectroscopy for a large sample of dC stars observed by the SDSS, to measure the dC binary frequency, which should be near unity in this mass transfer scenario. As was the case in Whitehouse et al. (2018), my SDSS sampling lacks enough epochs to determine individual orbital parameters. However, with a significantly larger sample of 240 dC stars, I used the distribution of RV variations and Markov Chain Monte Carlo (MCMC) methods to characterize the dC population's binary fraction and the separation distribution as was done by Maoz et al. (2012) and Badenes & Maoz (2012) for binary WD systems. With this newly characterized binary fraction and dC separations, I discuss the questions of dC formation, including what formation mechanisms are important in the observed dC population.

2.2 Dwarf Carbon Star Sample Selection

dCs for this study were selected from the Green (2013) and Si et al. (2014) carbon star samples. Green (2013) identified carbon stars by visual inspection of single-epoch SDSS spectra compiled from the union of (1) SDSS DR7 spectra (Abazajian

et al., 2009) having strong cross-correlation coefficients with the SDSS carbon star templates and (2) SDSS spectra with a DR8 pipeline class of STAR and subclass including the word carbon (Aihara et al., 2011). From within this carbon star parent sample, definitive main sequence dwarfs were selected by having significant proper motions ($\geq 3\sigma$ and 11 mas yr^{-1}) in the catalog of Munn et al. (2004) and/or having SDSS spectra visibly identifiable as composite DA/dC spectroscopic binaries (there are 3 DA/dC composites in the sample). Si et al. (2014) selected dCs using a label propagation algorithm from SDSS DR8, yielding 96 new dC stars DQ white dwarfs stars, which also show carbon bandheads, were removed by visual inspection.

In this work, which aims to measure RV variability, the primary additional selection criterion was that the selected dC stars have more than one epoch of spectroscopy in the SDSS as of November 2017. The majority of such objects were intentionally targeted for a second epoch of spectroscopy with the Time Domain Spectroscopic Survey (TDSS; Morganson et al., 2015), a subprogram of the SDSS-IV extended Baryon Acoustic Oscillation Sky Survey (eBOSS; Dawson et al., 2016) project. Within TDSS, the main single-epoch-spectroscopy (SES) program (Morganson et al., 2015) — along with its pilot survey, dubbed SEQUELS within SDSS-III (Ruan et al., 2016) — primarily targets optical point sources (unconfirmed quasars and stars) for a first epoch of spectroscopy based on variability. However, within several "few-epoch spectroscopy" (FES) subprograms, TDSS also acquires repeat spectroscopic observations for subsets of known stars and quasars that are of particular astrophysical interest. The FES programs are described by MacLeod et al. (2018a) and include several classes of quasars and stars, including dC stars, re-targeted to study their spectroscopic variability. For the dC FES program, all 730 SDSS dC stars from Green (2013) were selected as well as another 99 dC stars found by Si et al. (2014), totaling 829 unique dC stars provided

as candidates for spectroscopy by the SDSS-IV eBOSS project. About 40% of those stars were observed by the end of the eBOSS survey.

The observations for this work (for both the dC and the control samples) are from a combination of SDSS-I/SDSS-II and SDSS-III/SDSS-IV spectroscopic data. SDSS-I/SDSS-II spectra were taken with the legacy SDSS spectrograph. These data have a wavelength range of 3900–9100Å with a resolution of $R \sim 2000$, corresponding to $69 = \mathrm{km\,s^{-1}}$ per pixel. The new eBOSS spectrograph (Smee et al., 2013) in SDSS-III/SDSS-IV has improved qualities. This spectrograph covers the 3,600–10,400Å range and has a resolution of $R \sim 2500$. This spectrograph has a resolution of 1.7Å per pixel.

I then searched the SDSS database (using the CasJobs query tool) for spectroscopy from DR14 (Abolfathi et al., 2018) for the dC stars that have been observed in the dC FES program. I also checked the DR14 database for all dC stars in the Green (2013) sample in search of any dC stars that may have been observed more than once, but not as part of the TDSS FES program. The final sample contains FES spectra obtained up until October 31, 2017 and spectra from DR14.

I visually inspected all spectral epochs and removed any spectra that had strong broad artifacts. The final sample for this study was 240 dCs with a total of 540 spectra within the SDSS (as some dCs have > 2 epochs).

Figure 2.1 shows the correlation between r mag (Fukugita et al., 1996) and the median spectroscopic signal-to-noise ratio (S/N). The color axis is the Modified Julian Date (MJD) of each epoch, and a clear distinction can be seen between the early epochs and later epochs in regards to S/N due to the enhanced capabilities of the BOSS spectrograph.

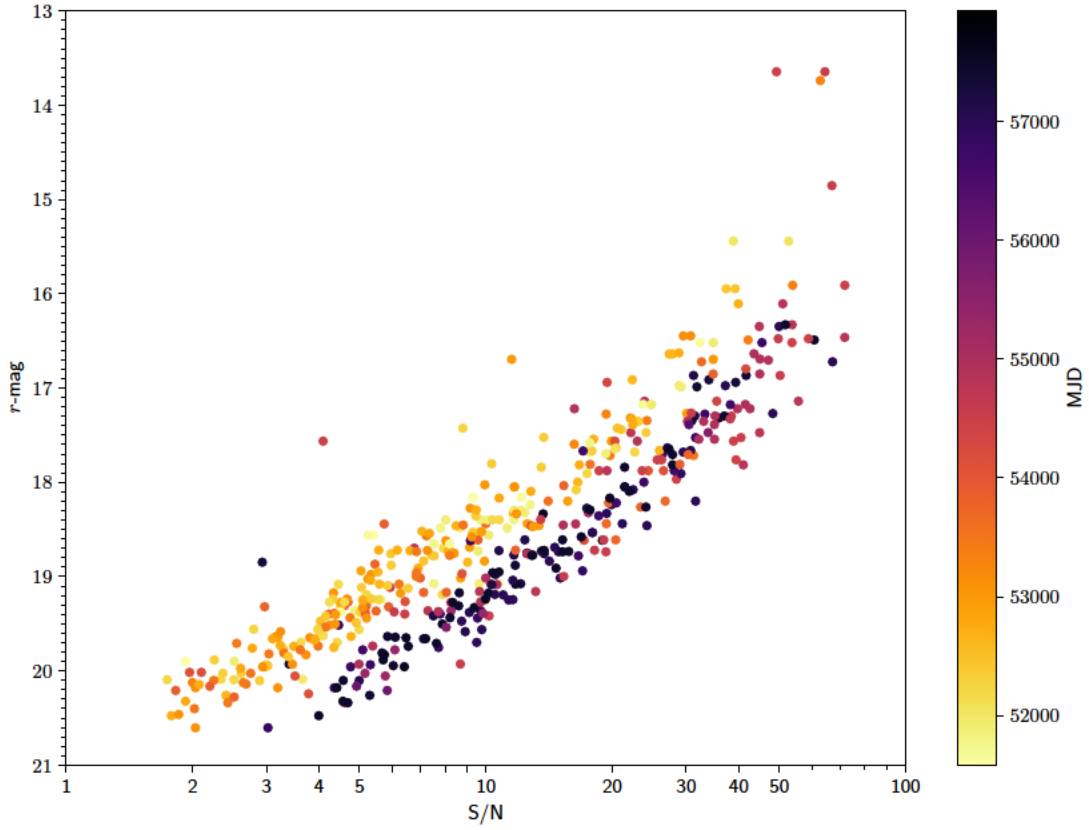

Figure 2.1: Optical r-band magnitude as a function of the median spectroscopic signal-to-noise ratio for my sample. Dots are colored by spectroscopic epoch in modified Julian days (MJD). The improved S/N of later epochs (using the BOSS rather than the legacy SDSS spectrograph) is evident. As expected, there is a close correlation between brightness and S/N.

2.3 Control Sample Selection

2.3.1 Selection Criteria

The control sample was selected from the SDSS DR14 catalog using the properties of the dC sample as selection criteria. The control sample criteria were as follows: (1) objects must have CLASS=STAR from the SDSS spectroscopic pipeline (2) a significant proper motion detection following the criteria of Green (2013)[1] (3) select only stars within the 2 – 98% parameter ranges of the dC sample (i.e., total proper motion between 11 and 143 milliarcseconds yr^{-1}, SDSS r mag between 15.9 and 20.3, and a $g-r$ color between 0.375 and 1.908 using extinction-corrected magnitudes and colors). All carbon stars (including dCs) were removed from the sample by SDSS CLASS and SUBCLASS keywords and by matching to all known dCs. Since their binary fraction is likely to be highly biased, I further removed stars originally targeted for reasons of X-ray emission or variability.[2] Finally, all control stars were required to have a match in the Gaia DR2 data release (Gaia Collaboration et al., 2018). These criteria returned 9,822 stars that had more than one SDSS spectrum for a total of 21,820 spectra.

2.3.2 Property Matching

To reduce the effects of different properties between the dC sample and the control sample, I matched the control stars to each dC by finding the normalized "distance"

[1] Proper motion in at least one coordinate larger than 3σ where σ is the proper motion uncertainty in that coordinate, and total proper motion larger than 11 $\mathrm{mas\,yr}^{-1}$.

[2] I removed from the control sample any eBOSS_TARGET0 stars that are selected by variability as TDSS targets (8). Most of these variables are RR Lyr or close eclipsing binaries and some are dC stars. I further removed stars where LEGACY PrimTarget keyword contained ROSAT or where BOSS ANCILLARY_TARGET1 = QSO_VAR, QSO_VAR_LF or QSO_VAR_SDSS. Finally, common proper motion binaries were removed by eliminating control stars with BOSS ANCILLARY_TARGET2 = SPOKE2.

in a "four-property space": r mag, $g - r$ color, Gaia DR2 total proper motion, and Gaia DR2 parallax.[3]

This distance matching was performed by creating a "normalized coordinate" out of each of the four properties. This coordinate was constructed by subtracting the minimum property value, then dividing by the maximum value for the property. This approach scales all of the values for each property into the range of $[0, 1]$ based on the dC sample so that all of the properties are similarly weighted.

These coordinates were used to find the distance from each dC to all of the control stars. These distances, once sorted, give the closest matching control stars for each individual dC based on the chosen four properties. With the control sample sorted for closest matching properties to the dC sample, I drew the closest matches for each dC to create the final, property-matched control sample to analyze along with the dC sample. Figure 2.2, compares histograms of these four properties (and errors on proper motion and parallax) for the dC and control samples.

2.3.3 Control Sample Issues

The control sample, even given the matching process used, is not perfect for several reasons.

(1) The SDSS stellar sample was produced by a hodgepodge of different targeting programs, some of which may skew the ΔRV distribution.

(2) It could be more difficult to detect binarity in the control sample because the single spectrum of an unresolved binary contains (by definition) both components. If the two components have significantly different main-sequence spectral types or evolutionary stages (e.g., giant + dwarf), then one component is much more luminous

[3]I used parallax rather than distance due to the subtleties of converting Gaia DR2 parallaxes to distance as noted in Luri et al. (2018)

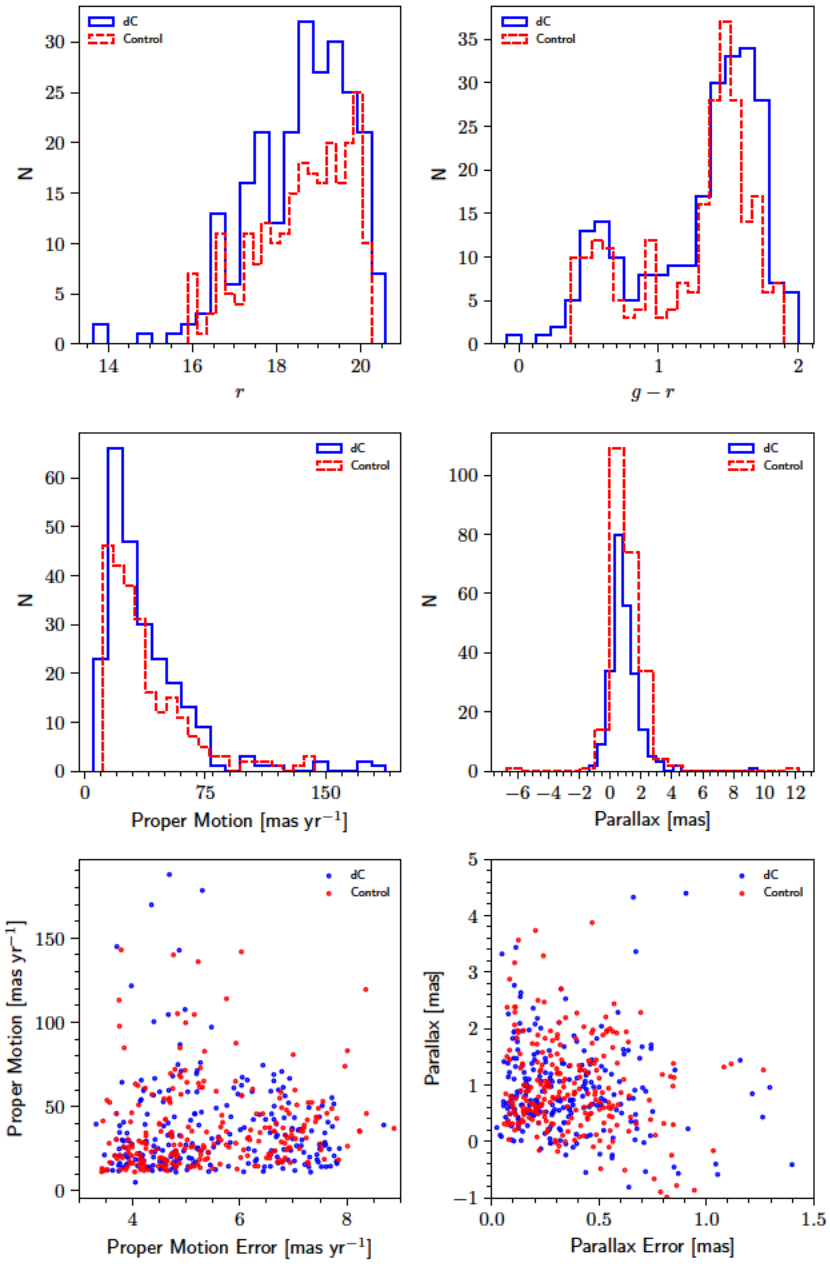

Figure 2.2: Comparison plot for the four properties used to match the control sample to the dC sample. The first four panels are histograms of the four properties used in the control sample matching process. The dC sample is in solid blue lines, and the control sample is in dashed red lines. The matching process is designed to recreate the dC histograms with the control sample. The bottom two panels are scatter plots of total proper motion and parallax with their associated errors..

than the other — similar to the dC systems expected, which likely contain a white dwarf too cool to detect in most spectra. However, if the two components have close spectral types (e.g., a K7+M2 binary), they contribute similarly to the spectral flux. Thus, the observed velocity changes are muted because if one component is approaching, the other is receding at any epoch. There are techniques that could mitigate this issue such as attempting to fit the sum of two spectral templates to each spectrum (e.g., as proposed by El-Badry et al. 2018, but this approach would be effective only for some combinations of mass ratios and S/N.

(3) The control sample has a significantly different MJD sampling than that of the dC sample. A majority of the control sample was observed in the earliest versions of the SDSS and have ΔMJDs between spectroscopic epochs on average of 100 days. Most of the dC stars have been specifically targeted by TDSS for repeat spectroscopy during SDSS-IV; so, they have a ΔMJD distribution of typically 1000s of days. While this sampling does affect the range of periods my methods are sensitive to, it should not impact the results. Since I am searching for close binary systems which have large ΔRVs and, therefore, short periods, the control sample's accessible ΔMJD distribution would only impede the ability to detect wide binary systems for which the sensitivity is already severely limited by the RV errors as shown in Section 2.4.2.

The first two items are observational and may diminish the discriminating power of the tests. Other intrinsic differences may complicate the analysis and interpretation of the results. For instance, dCs are expected to have a 100% binary fraction, but a very narrow range of companion masses (all white dwarfs, therefore, strongly peaked near $0.6\,M_{\odot}$). By contrast, the control sample has a certain binary fraction, but the distribution of companion masses in those binaries will have a wider range. The orbital properties of binaries in the control sample may also have a wider range. It

is also expected that the dC has interacted with its (former AGB) companion (e.g., either by wind accretion or Roche lobe overflow) which sets upper (and perhaps even lower) limits on the orbital separation. The only effective limit on orbital separation in the control sample is that the pair be spatially unresolved ($\lesssim 2''$).

2.4 Radial Velocity Analysis

2.4.1 Cross-Correlation Method

I measured RV variations (ΔRV) using the `IRAF`[4] (Tody, 1986) package `FXCOR` that cross-correlates between a template and object spectrum following the methods of Tonry & Davis (1979).

Each spectrum was visually inspected to ensure the S/N was sufficiently high for cross-correlation as well as to identify wavelength regions with corrupt data. I also searched for any problematic features that could affect the cross-correlation. Those objects that had corrupted regions were marked and individually run through the cross-correlation, ignoring those corrupted regions. The rest of the sample was cross-correlated in a batch, all using the same constraints and regions.

Each epoch combination's cross-correlation function was manually inspected to check the quality of the cross-correlation. In a small ($\sim$10%) fraction of cases, the cross-correlation function is best fit manually. If the cross-correlation function could not be fit (e.g., no peak in the CCF is preferred), that epoch combination was removed from the sample.

[4]IRAF is distributed by the National Optical Astronomy Observatories, which are operated by the Association of Universities for Research in Astronomy, Inc., under a cooperative agreement with the National Science Foundation.

2.4.2 Cross-Correlation Errors

To validate the cross-correlation process, I ran a variety of tests. The first was to verify and, if possible, minimize the reported errors from `FXCOR`.

To minimize uncertainties in the radial velocity measurements given by the cross-correlation, I used two techniques: (1) direct cross-correlation of one object against itself across different epochs and (2) cross-correlation of each epoch for one object against an SDSS C star template spectrum. For each method I also experimented with changing the regions sampled (e.g., only narrow atomic lines, excluding the carbon bands, or only including carbon bands).

From all combinations, I found the best method to be the direct cross-correlation between two epochs for a single object using the spectrum in the range of 4000 Å−7000 Å, ignoring telluric line regions, which is the method I adopt for this work. I use one epoch (the early MJD) as the "template" and the other epoch (the later MJD) as the "object". This method produces some benefits over using the usual template method: (1) This cross-correlation directly provides the ΔRV shift. (2) Since I use the same dC as the template and the object spectra, the ΔRV errors are reduced because a star is its own perfect template. (3) The SDSS C star template spectrum is for AGB C stars; there are no templates for dC stars.

The second test performed was to determine if the reported values and errors from `FXCOR` are believable for both dC and control spectra. This test involved finding "multi-shift" errors for the objects by trying to recover applied shifts between different epochs. I did this by shifting the later epoch by 30 different velocities between -100 km s^{-1} and 100 km s^{-1}. Then, using the same cross-correlation setup as I used to measure the ΔRVs, I see how well `FXCOR` was able to recover the applied shift.

`FXCOR` was generally able to recover the applied shift in both the dC and control

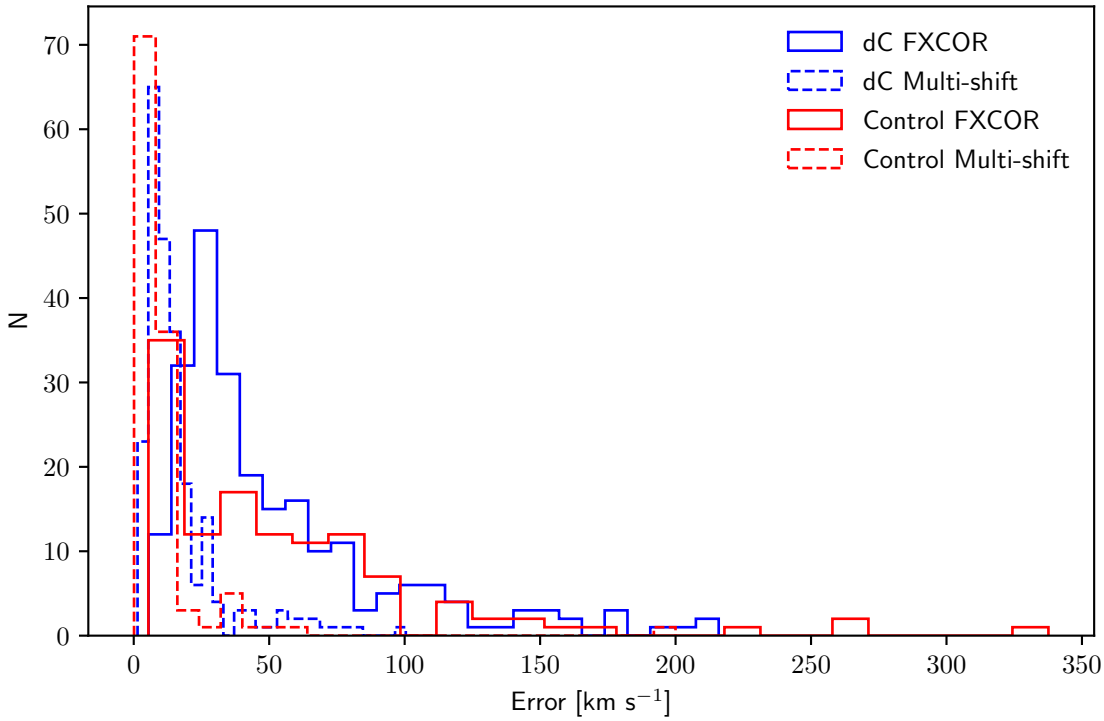

Figure 2.3: Histogram of reported `FXCOR` errors and "multi-shift" errors for both the control (red) and dC samples (blue). The errors reported by `FXCOR` are generally larger than the "multi-shift" errors.

samples. However, the reported errors from `FXCOR` generally are overestimated. By comparing each object's `FXCOR`-measured shift for each of the 30 different applied shifts, I determined "multi-shift" errors for each sample as the RMS of the measured − applied shift (see Figure 2.3).

Figure 2.3 presents histograms for the reported `FXCOR` errors and the measured "multi-shift" errors for both the dC and control samples. The top panel (a) shows how across the sample, the errors are smaller for the "multi-shift" errors than those reported by `FXCOR`. The bottom panel (b) displays that as `FXCOR` error increases, so do the "multi-shift" errors (a plausible result as spectral S/N is a key factor in the error).

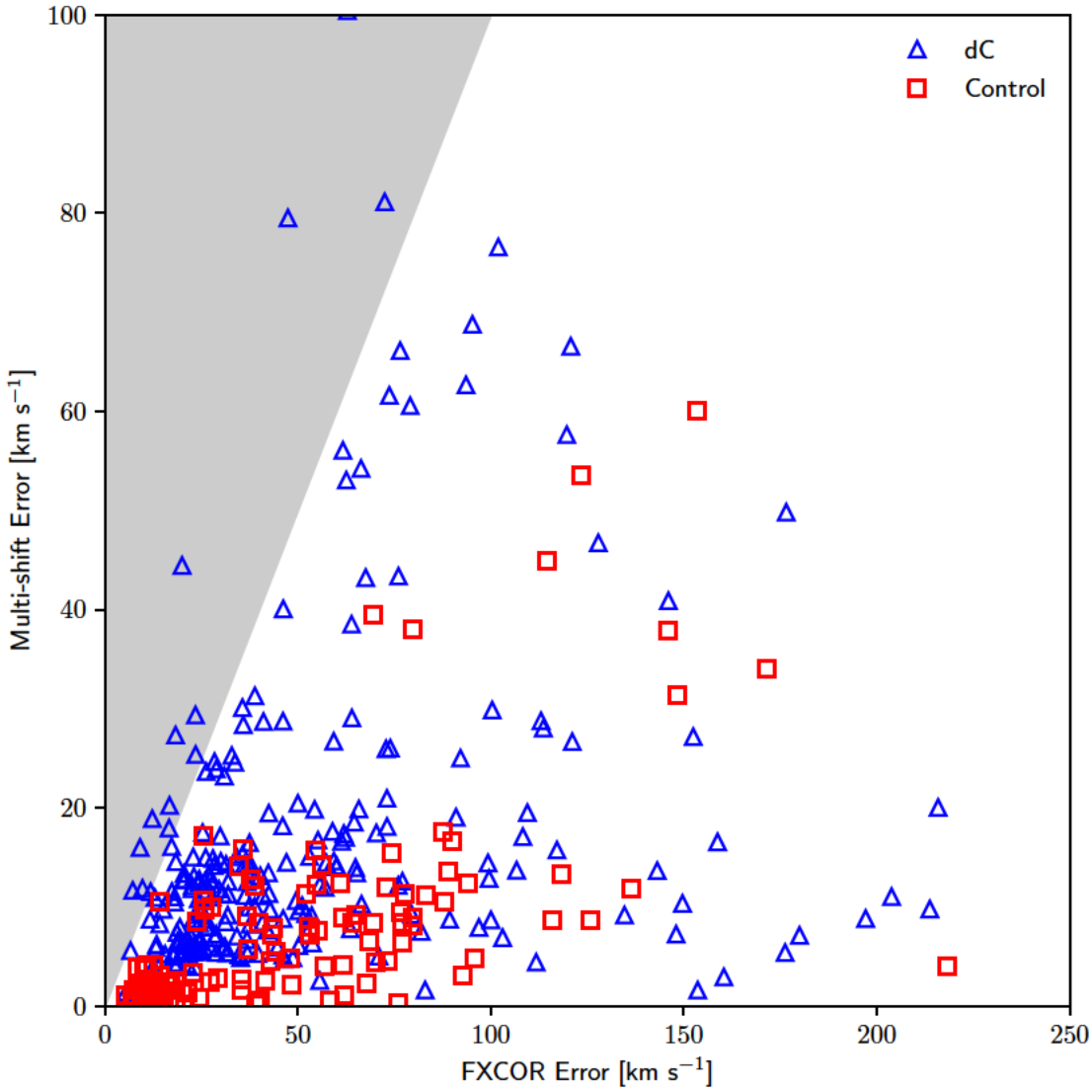

Figure 2.4: Multi-shift vs. FXCOR-reported errors further show a poor correlation. The shaded region shows those objects where the FXCOR-reported errors are smaller; very few objects lie in this region.

Kleyna et al. (2002) also found that FXCOR errors are overestimated. In their paper, they applied a multiplicative constant re-scaling factor of 0.35 to the FXCOR errors. Using the "multi-shift" errors, I found that the combined dC and control samples have an average scaling factor of 0.32. This scaling is consistent with the value from Kleyna et al. (2002).

However, I do not adopt the "multi-shift" errors throughout the rest of the analysis. I use the FXCOR reported errors knowing they are overestimated. This conservative error approach allows the rest of the findings to be shown as not relying on scaling down the errors.

Assuming $1.0 M_{\odot}$ + WD, edge-on system, given mean ΔRV errors of ≈ 28 km s^{-1}, the longest period that this method is sensitive to is ~ 15 yr. This is much longer than all of the control ΔMJD distribution, and longer than most of the dC ΔMJD distribution, so the sampling is not the limiting factor, the errors are (which is what is expected). I control for this by including the ΔMJD distribution in the modeling of Section 2.6 for both the control and dC samples. This involves using the ΔMJD distribution to sample the modeled observations so they represent real observations.

Figure 2.5 shows the relationship between the brightness (r mag) and the ΔRV errors from the cross-correlation. Brightness (and by proxy S/N) determines the ΔRV errors, and bluer objects tend to have smaller errors (again because these stars are usually brighter and have better S/N).

2.4.3 dC and Control ΔRVs

The dC and control samples were both cross-correlated using the same method. For every object, each possible combination of epochs was cross-correlated (with the earlier epoch as the template and the later epoch as the object). From all possible

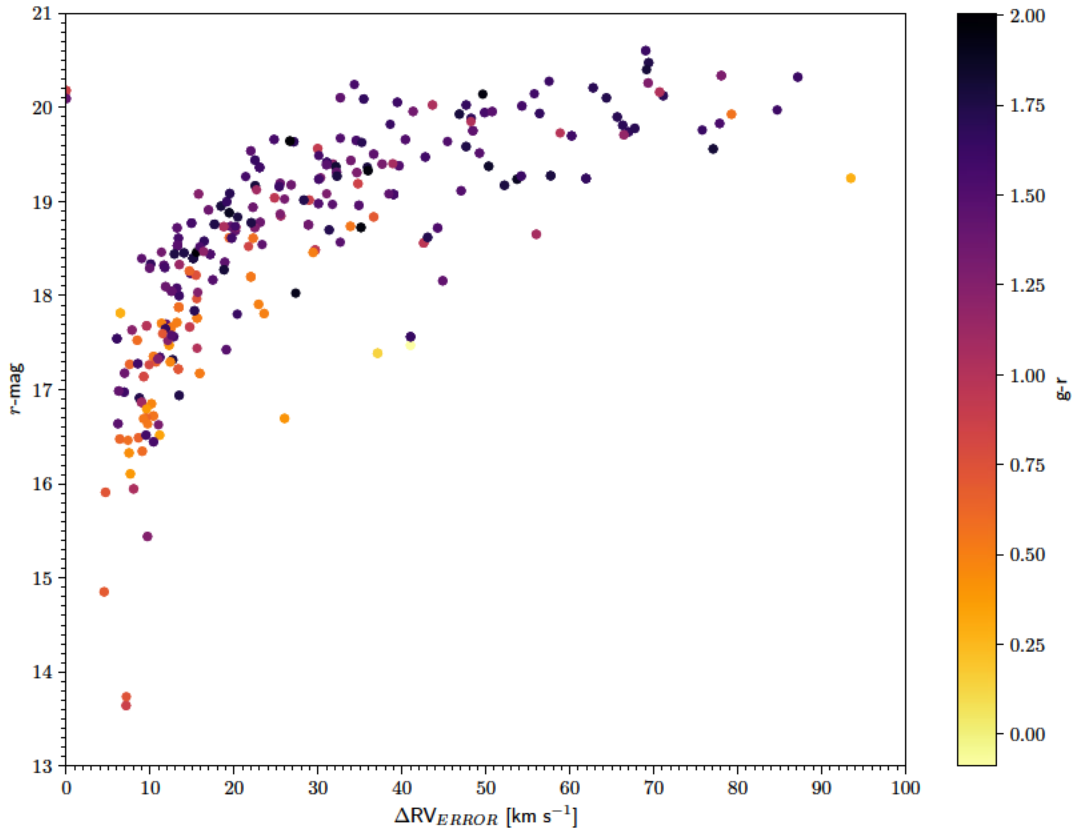

Figure 2.5: Optical r-band magnitude as a function of the radial velocity variation (ΔRV) errors obtained when directly comparing two epochs of dC stars in the sample. Fainter stars have larger errors, as expected, since these tend to have poor spectroscopic S/N (see Fig2.1). Optical $g-r$ color is denoted for each object by color.

combinations for an object, I selected the maximum ΔRV for the statistical analysis. The samples consist mostly of objects that have only two epochs of spectroscopy. Only a handful (N $\sim$ 30) of objects in either sample have more than two epochs.

Extremely large ΔRV values (e.g., >600 km s^{-1}) in a binary with a main-sequence component are suspect as in such cases it is expected that extremely close orbits and strong signs of interactions and mass transfer. Therefore, any object whose ΔRV was measured to be larger than this value was manually cross-correlated again and had its cross-correlation function manually fit to try and obtain a better ΔRV. If the cross-correlation is unsuitable for fitting, the object was removed from the sample (this only resulted in the removal of two dCs and three control stars).

Figure 2.6 is a normalized (note the log scale) histogram showing the ΔRV measurements for both the dC (blue) and control (red) samples. The same bins are used for each of the samples. This figure demonstrates that both samples have a central core whose width is dominated by errors. The dC sample, however, has a tail of high ΔRV systems that extends beyond this core. These systems likely represent close binary systems.

In the dC sample, I define these high ΔRV systems as those objects which display ΔRV values $\geq$ 100 km s^{-1}. Stars that display such high ΔRV values are indicative of close binary orbits. To confirm these large ΔRV systems, which should have visible shifts in their spectra, these large ΔRVs were inspected by shifting the later epoch by the measured ΔRV amount and visually checking to determine if features in the spectrum align.

Given that these systems display no strong signs of interaction (such as explosive variability or an accretion disk continuum emission component), few if any of the dCs are likely to have filled their Roche lobes and be transferring mass to the presumed

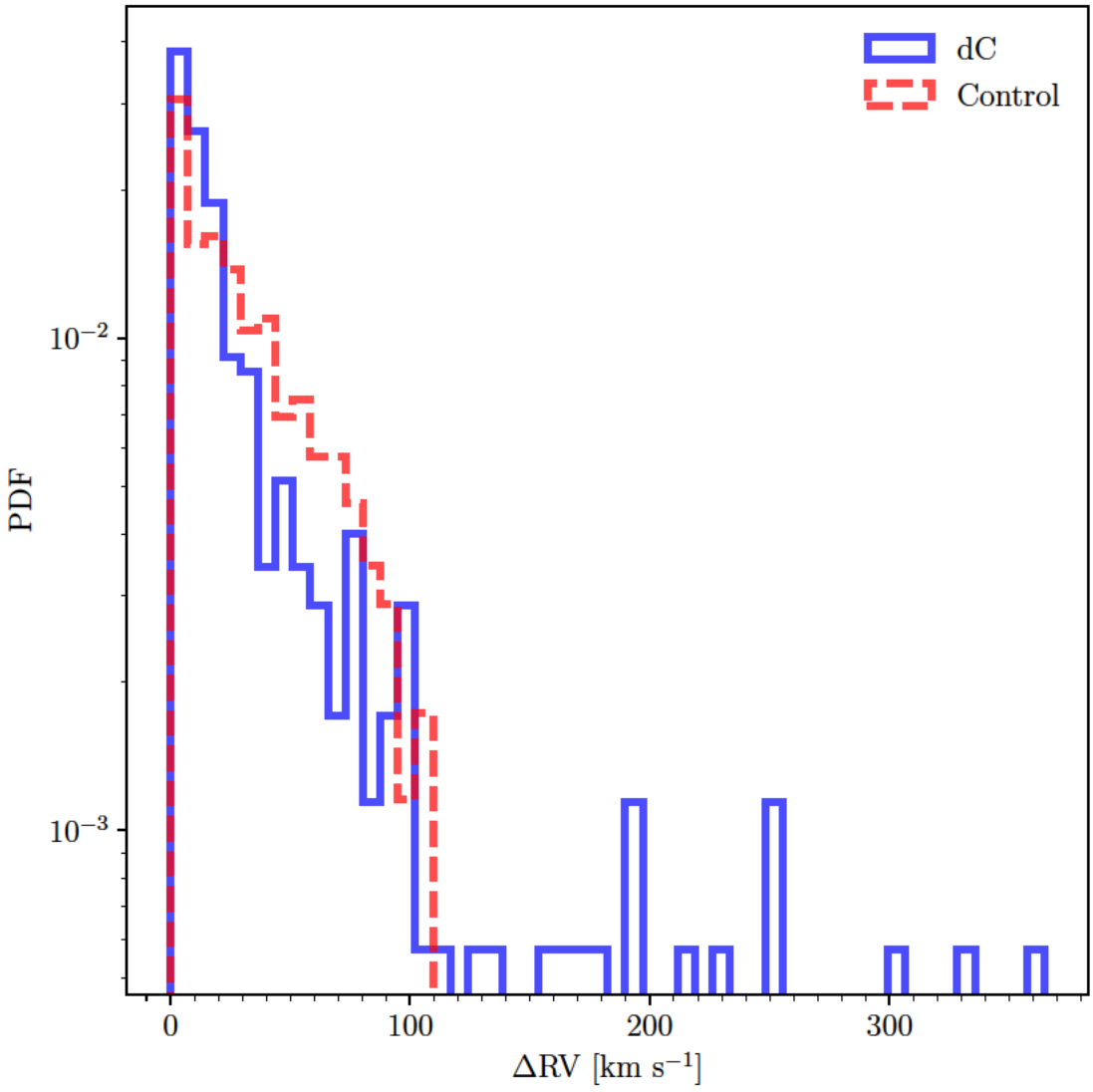

Figure 2.6: Normalized ΔRV histogram for both of the finalized dC and control samples. The wider flaring of the base for the dC sample suggests that dCs are in close binaries.

white dwarf companion. Figure 2.7 shows the largest possible ΔRV in which it is expected the dC would be filling its Roche lobe (for varying dC masses and a $0.5M_{\odot}$ WD). Using equation 2 of Eggleton (1983), I calculate the separation for a main-sequence star of each mass to fill its Roche lobe and calculate the corresponding critical ΔRV and period (ΔRV_{crit}, P_{crit}) that corresponds to the Roche lobe limit. This calculation assumes circular orbits (which should be expected for the dCs) and that the dC is the perfect case of an edge on system ($i = 90°$). The figure suggests that while some dCs have detected large ΔRVs; none are expected to be near the Roche lobe limit edge-on.

Figure 2.8 shows spectra for the dC with one of the largest measured ΔRVs. Both epochs are plotted with the early epoch in black and the late epoch in red. The top panel is of the original spectrum as observed by the SDSS. The bottom panel presents the same epochs, but the later epoch (red) has been shifted by the measured ΔRV = -252 ± 15 km s^{-1} amount. After this shift, the absorption features in the spectrum align confirming this measured ΔRV. All pre-BOSS spectra in this figure have been smoothed by a box-car of 20 pixels, and all later spectra have been smoothed by a box-car of 15 pixels so the SDSS legacy spectra match the resolution of the new BOSS spectrograph; because otherwise, there is a spurious appearance of variability.

Table 2.4.3 and Table 2.4.3 list the properties for the dC and control sample respectively. Only the first 10 rows for each are shown, the full machine-readable tables are available online.

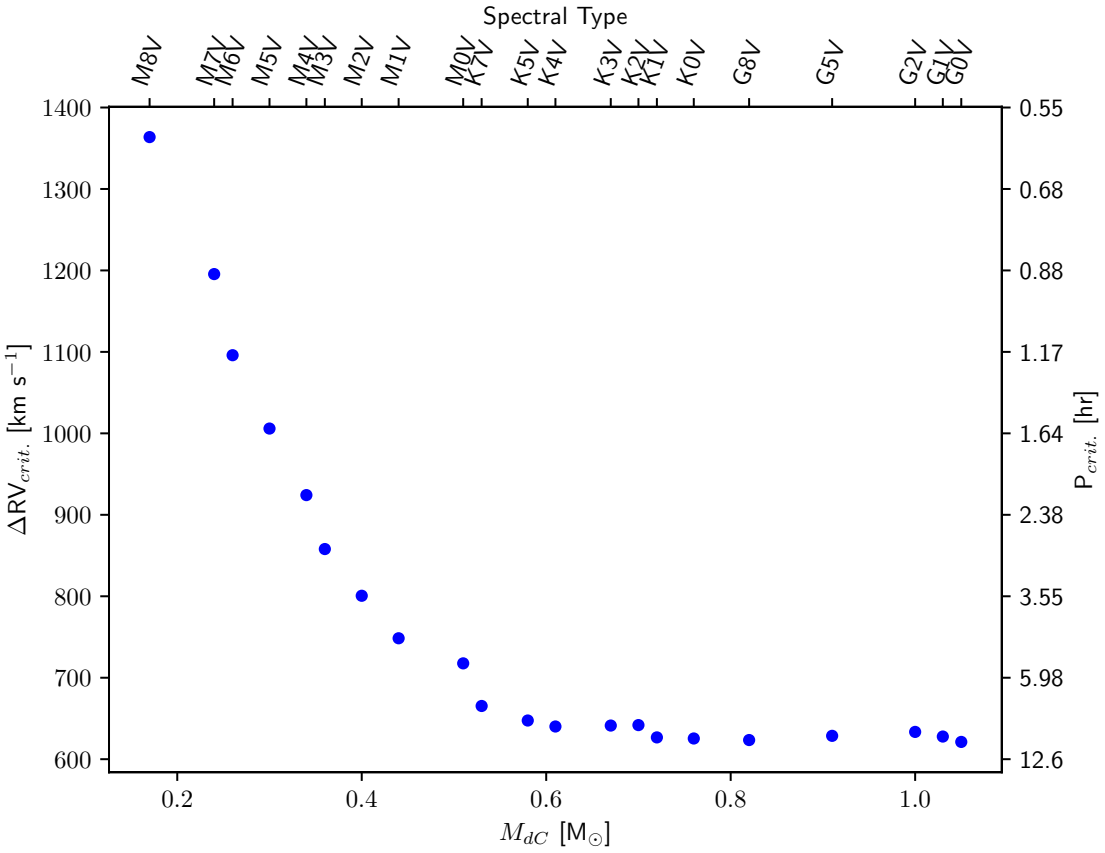

Figure 2.7: The maximum possible value of ΔRV for a range of the expected possible dC masses with a 0.5M$_\odot$ WD companion. I define this maximum ΔRV to be when the dC fills its Roche lobe. Using the equation of Eggleton (1983), I calculate the separation for a main-sequence star of each mass to fill its Roche lobe. Also indicated are the corresponding spectral type for each mass and the corresponding period (which is a minimum) for each of the maximum ΔRVs.

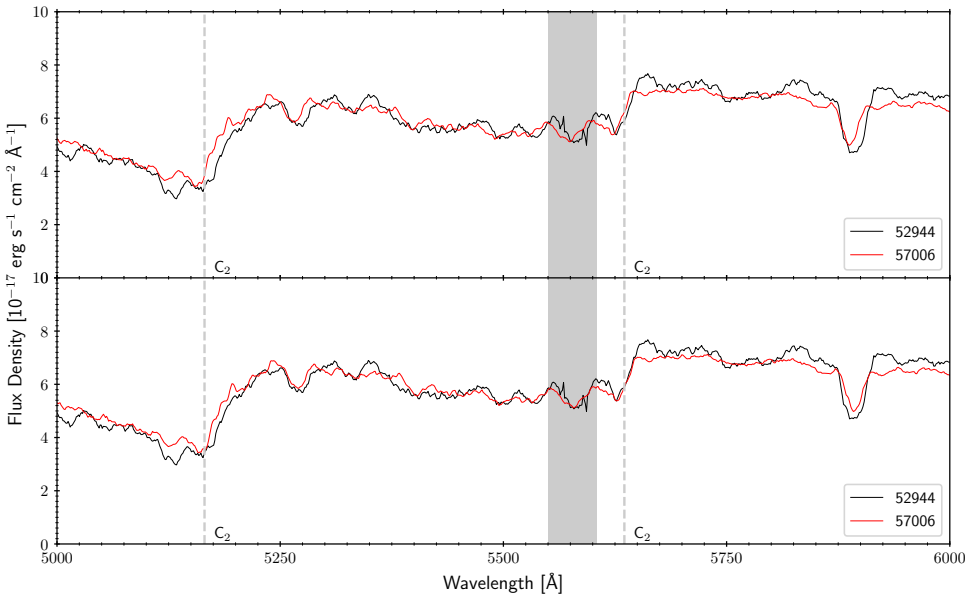

Figure 2.8: Smoothed spectra of both epochs for the dC with one of the largest measured ΔRV, (α_{J2000},δ_{J2000}) = (9.33893°, +0.20685°). The early epoch is in black, and the later epoch is in red. TOP: shows both epochs as measured in the SDSS. BOTTOM: shows the same spectra, but the late epoch (red) has been shifted by the measured ΔRV = -252 ± 15 km s^{-1}. After shifting, the absorption lines clearly align between epochs confirming this ΔRV and lending evidence that this dC is in a close binary orbit. The gray region is between 5550 Å and 5604 Å and covers the span of the OI night sky line which may contaminate the flux in that region. Locations of the C_2 bands in this wavelength range are shown.

Table 2.1: dC property table. Each object can be identified by its SDSS plate-mjd-fiberID combination as well as its celestial coordinates. Included in this table are r mag, $g-r$ color, and the measured ΔRV and errors. This table is sorted on α_{J2000} and each dC is given an index starting at 1. This index links each dC star to the corresponding control star from the matching process. Shown here are the first 10 dC stars.

Index	α_{J2000} [Deg]	δ_{J2000} [Deg]	r	$g-r$	Plate1	MJD1	FiberID1	Plate2	MJD2	FiberID2	ΔRV [km s^{-1}]	ΔRV$_{error}$ [km s^{-1}]
1	0.0626	28.1693	17.97	0.74	2824	54452	253	7696	57655	83	5	13
2	0.1483	-0.1875	18.74	1.42	1489	52991	156	7850	56956	704	-18	22
3	0.9212	23.9270	16.94	1.74	2801	54331	201	7665	57328	734	25	14
4	1.2380	1.1606	18.33	1.14	1490	52994	364	7862	56984	626	6	11
5	3.1909	-1.0895	19.47	1.59	687	52518	297	7863	56975	804	44	33
6	6.8651	6.6597	17.47	0.41	3106	54714	139	3106	54738	131	14	25
7	7.3310	0.7206	18.84	0.7	1087	52930	504	7855	57011	424	26	31
8	9.3389	0.2069	19.01	0.88	1495	52944	353	7868	57006	812	-252	15
9	9.9056	15.4863	18.48	0.95	419	51812	346	419	51868	346	11	26
10	10.8422	0.4788	16.72	0.55	1904	53682	495	7870	57016	562	13	8

Note — A machine-readable version of the full table is available online with the publication Roulston et al. (2019).

Table 2.2: Control sample property table. Each object can be identified by its SDSS plate-mjd-fiberID combination as well as its celestial coordinates. Included in this table are r mag, $g-r$ color, and the measured ΔRV and errors. This control table is sorted on the index which links each control star to the corresponding dC from the matching process. Shown here are the first 10 control stars that correspond to the first 10 dC stars in Table 2.4.3.

Index	α_{J2000} [Deg]	δ_{J2000} [Deg]	r	$g-r$	Plate1	MJD1	FiberID1	Plate2	MJD2	FiberID2	ΔRV [km s^{-1}]	ΔRV$_{error}$ [km s^{-1}]
1	47.6415	-0.2745	17.91	0.73	2068	53386	74	7255	56597	160	1	9
2	172.5454	20.1782	18.7	1.43	3170	54859	640	3170	54907	582	-54	26
3	0.9212	23.9269	16.94	1.74	2801	54331	201	7665	57328	734	-18	19
4	35.3647	-0.2364	18.22	1.18	704	52205	234	703	52209	30	-53	19
5	170.6615	45.6529	19.65	1.57	3216	54853	143	3216	54908	156	66	55
6	6.8651	6.6597	17.47	0.41	3106	54714	139	3106	54738	131	22	11
7	10.6953	-0.6110	18.83	0.7	1905	53613	213	1905	53706	219	32	27
8	113.8683	41.4378	19.07	0.92	3658	55205	890	5941	56193	884	12	38
9	44.3177	0.9009	18.39	0.95	1512	53035	590	1512	53742	579	-2	26
10	108.2489	38.7804	16.77	0.54	2938	54503	6	2938	54526	18	3	8

Note — A machine-readable version of the full table is available online with the publication Roulston et al. (2019).

2.5 Statistical Comparison of ΔRV Distributions

2.5.1 Anderson-Darling Test

I used a standard, two-sample Anderson-Darling (AD; Scholz & Stephens, 1987) test to determine the similarity between the dC and control ΔRV distributions. From the measured dC and control ΔRVs, the null hypothesis that the dC and control ΔRVs are drawn from the same distribution can be rejected at the 99.95% level ($\log p = -3.31$).

2.5.2 Extreme Deconvolution

A drawback of the AD test is that it does not take measurement uncertainties into account when comparing two distributions. For example, two distributions can look dissimilar if their uncertainties are different even if their true underlying distributions are identical. To ensure that the wider ΔRV observed in the dC sample in Figure 5 is not simply due to differences in the measurement uncertainties (since the dCs have larger errors, as seen in Figure 2.3, likely a result of the C_2 and CN bands), I use the extreme deconvolution (XD) method of Bovy et al. (2011) to deconvolve the underlying distribution of the ΔRV measurements. This XD method employs a Gaussian Mixture Model (GMM) to infer the underlying distribution from a set of heterogeneous, noisy observations or samples while incorporating the errors.

I tested the number of components for the XD-GMM for both the dC and control samples using the Bayesian Information Criterion (BIC) of each model. The BIC approach suggests that the dC sample is best modeled by a mixture of three Gaussians. However, the third Gaussian component for the dC population converges to a small normalization and an unphysically large width; so, I constrain the dC sample to be fit with two components. This decision allows for a central core and for a possible large ΔRV tail that contains close binary systems. The control sample is best fit by a

Table 2.3: Values of the component fits for the XD-GMM for both the dC and control samples. Listed are the mean (μ) and standard deviations (σ) of each component as well as the weights (α; $\Sigma_i \alpha_i = 1$).

Parameter	dC	Control
α_1	0.688	1.00
μ_1 [km s^{-1}]	2.02	9.69
σ_1 [km s^{-1}]	251.53	1035.82
α_2	0.312	
μ_2 [km s^{-1}]	2.36	
σ_2 [km s^{-1}]	12365.92	

single Gaussian as determined by the BIC. Table 2.5.2 lists the parameters for these fit components for both the dC and control XD-GMMs.

Figure 2.9 shows the results of the XD analysis, displaying both XD-GMMs for the two samples (smooth curves) and the histogram of the measured ΔRVs (both the smooth PDFs and histograms have been normalized to an integral of one). This figure demonstrates that both the dC and control samples have a core in their ΔRV distribution, but the dC distribution has a much broader wide component that flares out from the core.

The width of the single component as fit to the control sample is wider than that narrow component of the dC sample. At the risk of over-interpreting this difference, I mention several effects that could contribute to this difference. First, I have used the `FXCOR` reported errors, which in Section 2.4.2 were shown to be overestimated. Since the control sample is primarily from legacy SDSS spectra with lower S/N (therefore larger errors), this overestimation is larger and may inflate the error-deconvolved core of the control distribution. Second, the single control sample fit component must accommodate the full range of single and multiple systems. Third, the narrow core of the dC sample could be real; perhaps, some fraction of dC binary orbits have

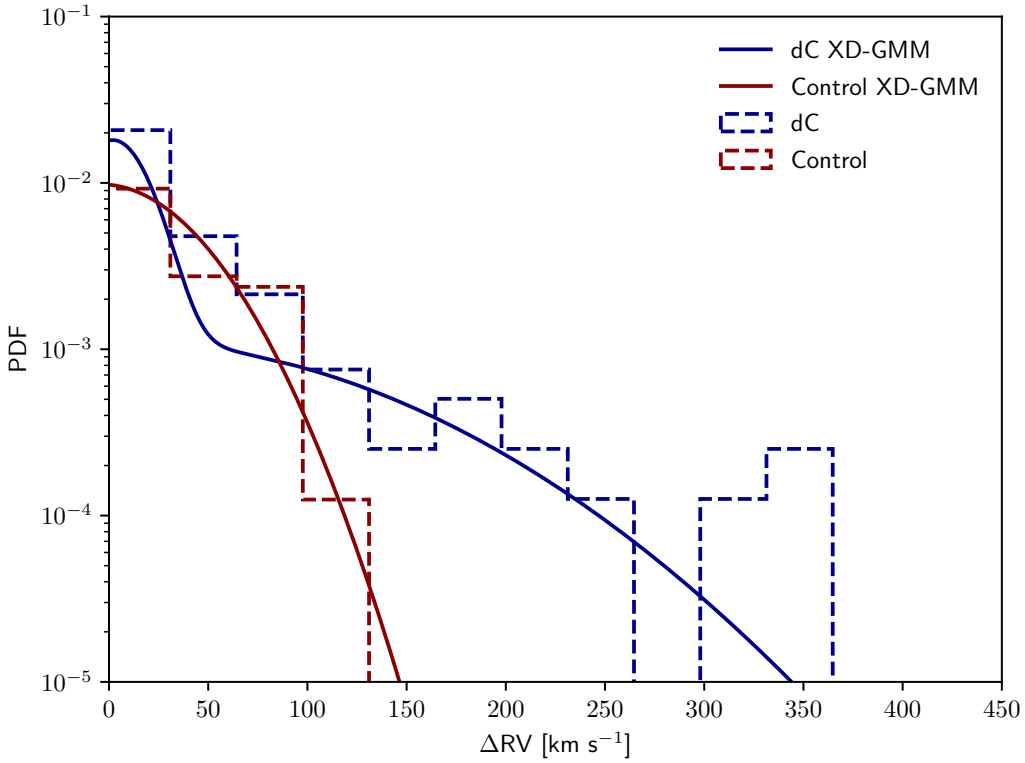

Figure 2.9: XD-GMM for both the dC and control samples. The histograms are the measured ΔRV values from this work with the dCs in blue and the control sample in red. The smooth curves are the XD-GMM PDFs generated from the ΔRV values (taking into account the ΔRV errors) with the dCs in blue and the control sample in red (note the logarithmic scale). A central core is visible in both the dC and control samples, but the dC has an extended tail that extends from the core. This large ΔRV tail is indicative of close binaries amid the dC population.

actually widened due to processes related to mass transfer. Chen et al. (2018) report that some wider binaries may undergo BHL accretion and further separate since the orbit-synchronized rotation of the giant star could serve as an angular momentum reservoir. However, a narrower core for the control sample should still be expected since a substantial fraction should be single stars.

It should be noted that this XD method simply uses the GMM method with errors to determine the underlying PDF as a mixture of Gaussians but does not imply or impose any physical meaning or model on the data. However, it clearly allows the determination that the dC sample has a tail that extends far beyond that of the control sample and is indicative of close binary systems included in the dC population.

2.6 Binary Orbit Simulations

While this sample lacks sufficient epochs per dC to fit individual orbits, I can use the ΔRV distribution to model the binary fraction and separation distribution. Assuming a primitive dC mass distribution further allows us to characterize the expected period distribution of the dC sample. I use a MCMC method to compare these simulations to the ΔRV distribution found in this work for both the dC and control samples.

Since little is known of dC orbital properties outside of G77-61, I made some physically-driven assumptions. First, I assumed that the dC orbits have been circularized ($e = 0$) since it is expected that all of them to have undergone mass transfer. Second, I used the observed ΔMJD distributions of each sample to simulate the observations and to sample the modeled ΔRVs. Third, I assumed that the WD mass distribution follows that found by Kepler et al. (2007) (i.e., a combination of four Gaussian components. The dominant component is centered on 0.58 $M_{\odot}$ with a width of 0.047 $M_{\odot}$). I used the distribution for the hot WD sample in Kepler et al.

(2007) since they state the distribution for the cooler WDs is not reliable. I also assumed a probability density function (PDF) that is uniform over $\cos i$ in order to determine the PDF for $\sin i$. Finally, since there are no known constraints on the dC mass distribution, I assumed a uniform PDF over the range of $0.2 M_{\odot}$ and $1.0 M_{\odot}$, simply assuming that dCs span the same range of masses as normal main-sequence stars of the same $g - r$ color distribution. Since the control sample was selected to cover the same magnitude and color range as the dC stars, I used the same mass distribution as the dCs. The other model assumptions are also held to keep the model simplified.

With these assumed PDFs, I simulated a population of stars and sampled those orbits to obtain a simulated ΔRV distribution. Comparing the simulated ΔRV distribution to the measured one allows the MCMC to map the separation distribution parameter space.

For the first simulation, I assumed that the stars that are binaries have separations that follow a log-normal distribution with unknown mean μ and standard deviation σ, as shown in Equation 2.1. I placed no constraints on the model parameters, aside from those required by the log-normal PDF (i.e., $\sigma \geq 0.0$ km s^{-1} and $0.0 \leq f_b \leq 1.0$), and allowed the MCMC walkers to explore the parameter space freely.

$$f(a) = \frac{1}{a\sigma\sqrt{2\pi}} \exp\left(-\frac{(\ln a - \mu)^2}{2\sigma^2}\right) \tag{2.1}$$

Using the Goodman & Weare (2010) algorithm, I ran 100 MCMC walkers for 1,000,000 steps. This approach allowed the walkers to explore all of the parameter space and sample the posterior of the model, which I checked for with the convergence of the chains. Figure 2.10 shows the resulting MCMC posterior distributions for the three model parameters for the dCs. Figure 2.11 shows the same plot for the control

sample.

From Figures 2.10 & 2.11, the simulations show that the dC stars have an enhanced binary fraction as compared to the control sample (95% vs. 60%). The dC binary fraction fit is consistent (within the uncertainties) with a binary fraction of 100%, indicating that dwarf carbon stars are indeed the results of binary mass transfer.

The resulting separation distribution from the dC MCMC simulation has a mean of 0.39 AU, a variance of 0.28 AU, and a median of 0.36 AU. These distances correspond to mean periods of 79-100 days depending on dC mass (G77-61 has a period of 245 days) and a minimum period for this distribution is on order 2.5 days (consistent with Margon et al. (2018), who found a dC with a period of 2.9 days using photometry from the Palomar Transient Factory). The separation distribution generated by the MCMC results in periods that are consistent with the few periods known of individual dC systems.

However, de Kool & Green (1995) predicted that dC stars should follow a bimodal period distribution with one peak between $10^2 - 10^3$ days and another at $10^3 - 10^5$ days. Therefore, I also modeled a bimodal mixture model (made of two log-normal separation distributions) of the form in Equation 2.2. For this model, I use the most likely dC binary fraction of 95%.

$$f(a) = \frac{\alpha}{a\sigma_1\sqrt{2\pi}} \exp\left(-\frac{(\ln a - \mu_1)^2}{2\sigma_1^2}\right) + \frac{1-\alpha}{a\sigma_2\sqrt{2\pi}} \exp\left(-\frac{(\ln a - \mu_2)^2}{2\sigma_2^2}\right) \tag{2.2}$$

In Equation 2.2, μ_i and σ_i are the same parameters as in the unimodal distribution, and α is the mixing parameter in this mixture model that controls how much of each distribution contributes to the total PDF. As before, I place no constraints outside of those required by the log-normal PDFs and required by the mixing parameter (i.e.

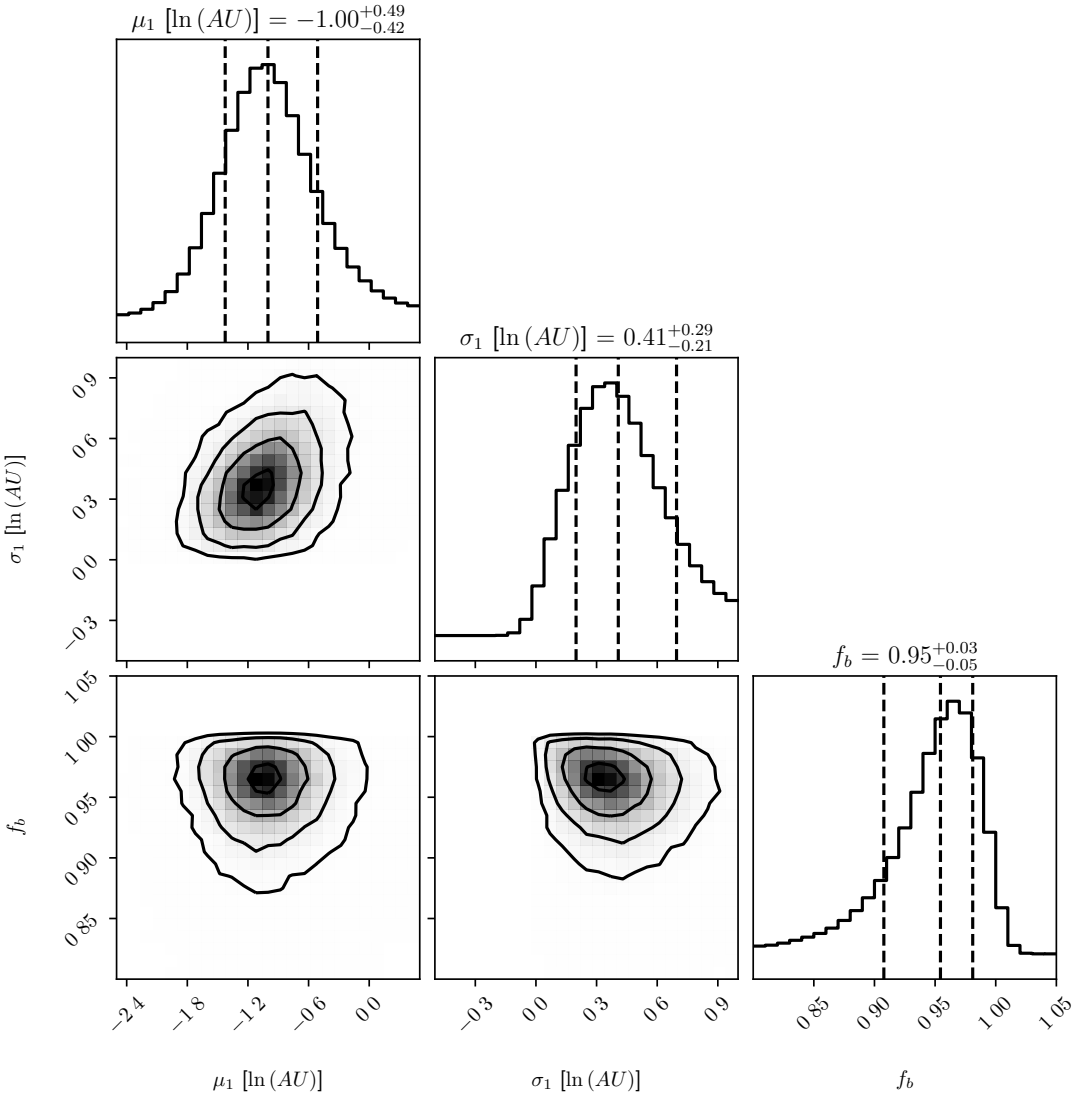

Figure 2.10: The posterior distributions for the model parameters (μ, σ, f_b) for the unimodal log-normal distribution from the dC sample MCMC simulation. Vertical dashed lines represent the 1σ range and the median ($50th$ percentile). Values are the natural logarithm (ln) of the separation in units of AU.

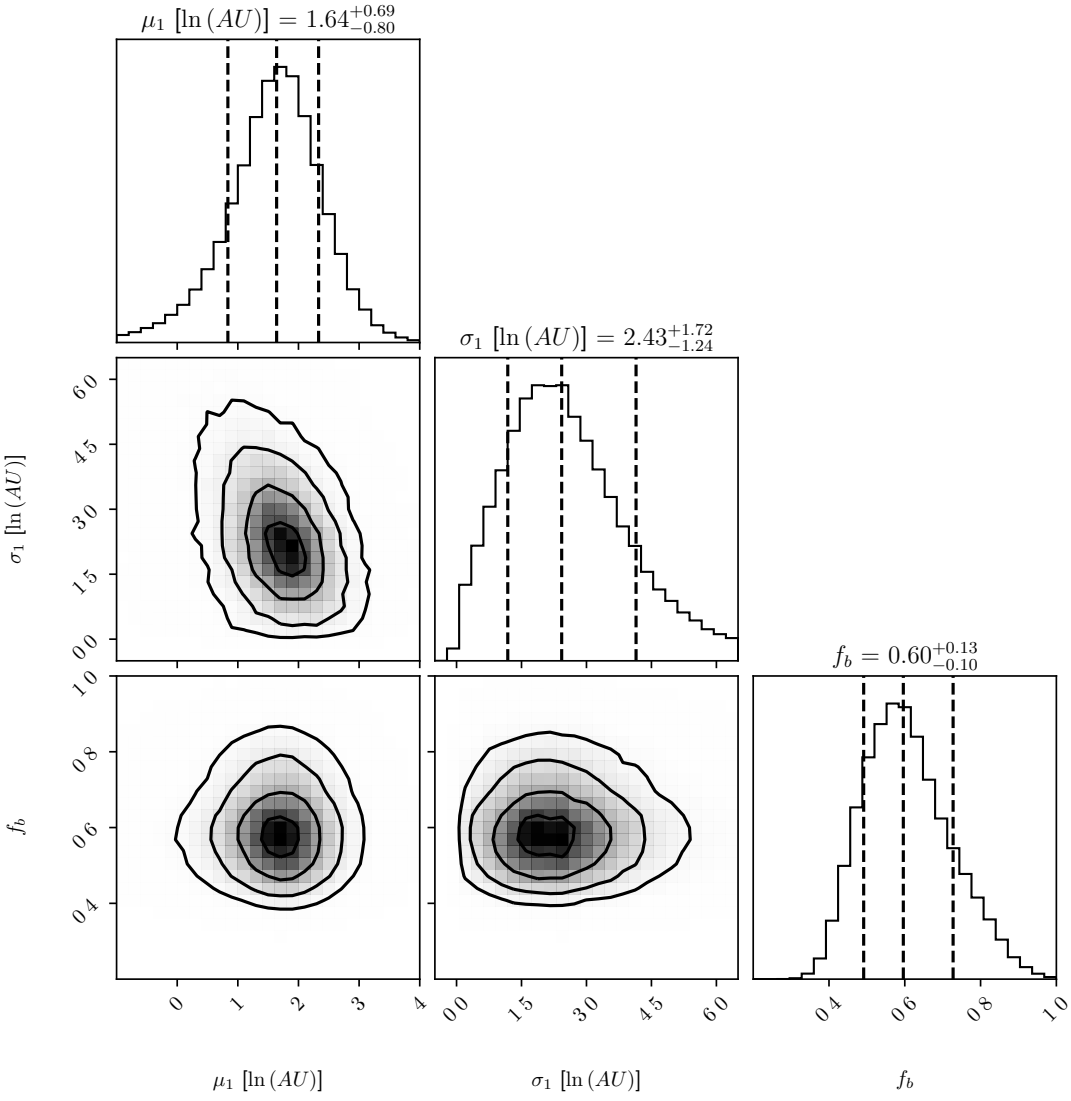

Figure 2.11: The posterior distributions for the model parameters (μ, σ, f_b) for the unimodal log-normal distribution from the control sample MCMC simulation. Vertical dashed lines represent the 1σ range and the median ($50th$ percentile). Values are the natural logarithm (ln) of the separation in units of AU.

$0.0 \leq \alpha \leq 1.0$).

This bimodal distribution MCMC simulation was run for 100,000 steps with 100 walkers. The reduction in steps is required by the increased computational load when drawing from this bimodal PDF distribution. While this change does reduce the number of points in the parameter space, the MCMC walkers still mapped the posterior quite well, which I checked for with the convergence of the chains.

Figure 2.12 shows the MCMC posterior distributions for the bimodal mixture model for all five of the model parameters for the dC sample. In this bimodal mixture model, the total separation distribution has a mean of 0.71 AU and a variance of 1.45 AU. This distribution gives (for the previously stated uniform dC mass range) a range of the mean period of 298-413 days. Although the number of measured dC periods is quite sparse, the period distribution (calculated from the separation distribution) is in agreement with those few periods in the literature.

These results are promising, but improvements are possible. One significant improvement can be achieved by measuring dC masses via orbital fits from a follow-up spectroscopy campaign. Fitting an orbit to even a few dCs will place initial physical constraints on the dC mass distribution. With a more physical and realistic dC mass distribution, the models and MCMC simulations can fit a more accurate separation distribution than can be done with the currently used uniform mass distribution.

2.7 Balmer Emission Lines

The multi-epoch spectra present an opportunity to survey the dC sample for Hα emission line strength and variability. Balmer line emission has been observed in dCs, and Green (2013) found that about 2.6% of dCs showed Hα emission.

There are 10 objects with Hα emission in this sample. Balmer line emission might

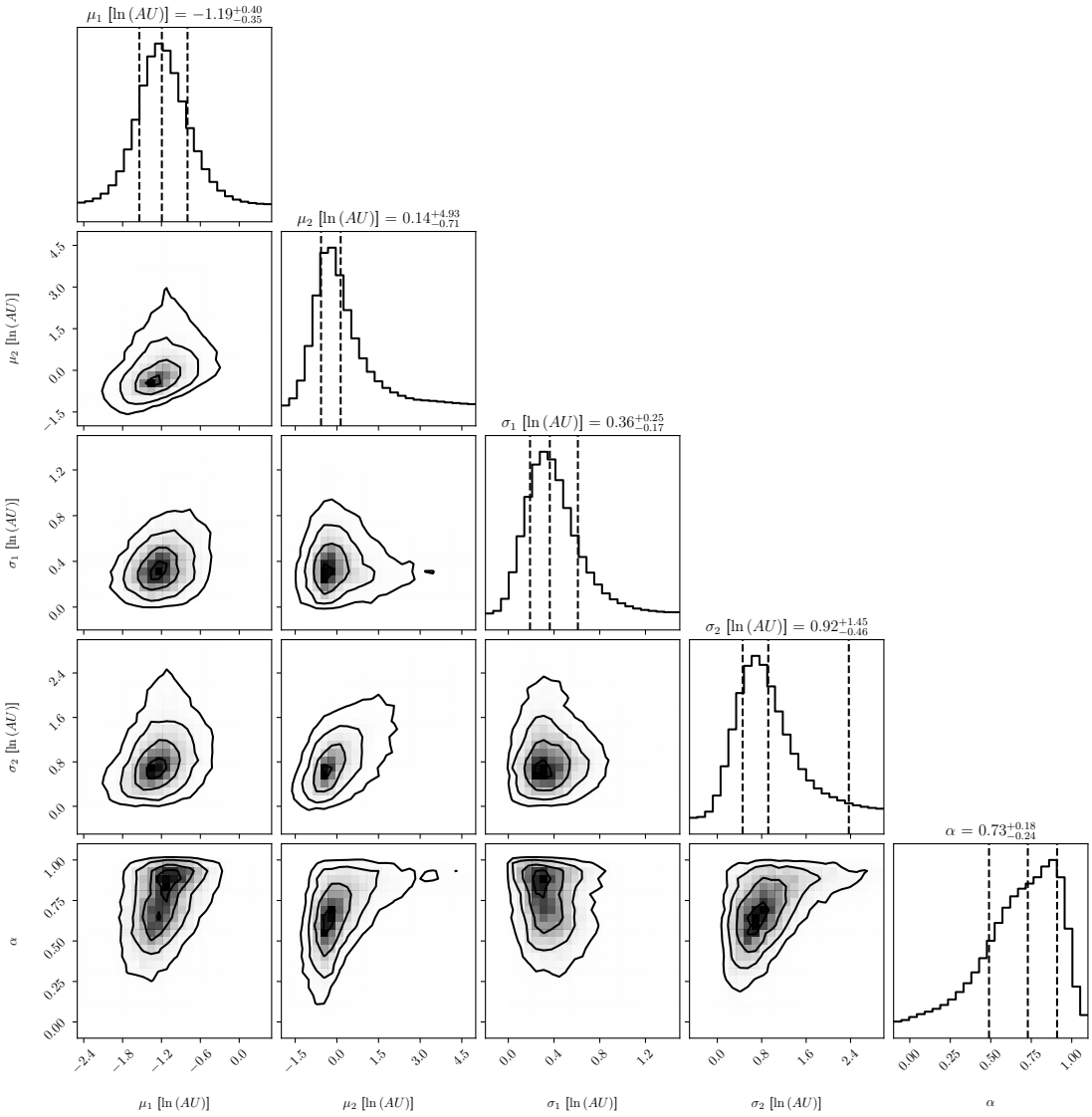

Figure 2.12: The posterior distributions for all five of the model parameters $(\mu_i, \sigma_i, \alpha)$ for the bimodal mixture model of log-normal distributions from the MCMC simulations. Vertical dashed lines represent the 1σ range and the median (50^{th} percentile). Values are the natural logarithm (ln) of the separation in units of AU (α is a dimensionless mixture parameter).

be expected among dCs for several reasons: (1) coronal emission that may be a result of increased activity from spin-up during the accretion phase of the dC evolution — valid for recent (< 1 Gyr) interactions before the dC has spun-down again., (2) irradiation of the dC by a hot white dwarf companion, or (3) spin-orbit coupling in a close WD/dC binary.

To explore case 1, in a related effort, I have been analyzing *Chandra* observations of a small sample of dC stars to test whether their X-ray emission is consistent with dynamo rejuvenation by accretion spin-up (see Chapter 4).

If the emission is from case 2, it is expected to detect the WD component in the dC spectra. Indeed, all four of the DA/dCs show emission in their spectra. The remaining six of the Hα emission line dCs are of the "normal" type (i.e., no visible WD in the spectrum). Hα emission is variable in only one normal dC and in none of the DA/dCs. Since close orbits should be required for cases 2 and 3, I have been pursuing further multi-epoch spectroscopy for emission-line systems.

2.8 Discussion

Using multi-epoch spectroscopy I have measured the RV variations of an SDSS sample of dC stars. Through MCMC methods, the models were able to constrain the binary fraction and construct the separation distribution of this dC population that best recreates the observed ΔRV.

I presented the best parameters for two separation models: a unimodal log-normal distribution and a bimodal mixture model of log-normal distributions. Both models result in close binary separation distributions with means less than 1 AU, corresponding to mean periods on the order of 1 year (varying depending on dC mass).

The sample contains a handful of objects with large ($\geq$ 100 km s^{-1}) ΔRV mea-

surements that are indicative of close binary systems. These objects will be targeted for future spectroscopy to constrain orbital parameters thereby better characterizing the separation distribution. In addition, orbital fits will also allow us to determine the masses of the dCs assuming a WD component.

Badenes et al. (2018) analyze the RV variability of main-sequence stars and report that the binary fraction is likely higher for more metal-poor stars. Carbon stars are suspected to form more easily at lower metallicity; indeed, about 20% of stars with [Fe/H]< -2 show carbon enhancement (e.g., Christlieb et al. 2001; Lee et al. 2013), but that frequency is increasing rapidly as metallicity decreases (Placco et al., 2014). Close binaries (< 10 AU) also show increases in lower metallicity populations (Moe et al., 2019). The dC in G77-61 is thought to be extremely metal-poor (Gass, 1988). The measured dC ΔRV distribution being wider than the control sample could in part be due both to low metallicity and to evolutionary effects since dC stars are carbon-enhanced by binary mass transfer. If the mass transfer results in inward evolution of the binary, then that should further widen the ΔRV distribution for dCs. Binaries with an AGB primary can be at large separations and still, via wind-RLOF, lose orbital angular momentum, evolve towards direct RLOF and/or tidal friction towards a CE phase (Chen et al., 2018). Therefore, the fraction of binaries that result in mass transfer in a CE phase and a tight binary configuration may be quite large. The dC stars present a population of post mass transfer binaries that are unusually easy to identify, but may represent just a tiny fraction of such stars — those sufficiently cool and with large enough C/O to produce C_2 and/or CN bands. In some cases, the AGB evolution may have been truncated during the CE phase before significant carbon dredge up. A much larger space density of post-mass transfer M dwarfs may remain unidentified until massive multi-epoch RV surveys become available.

2.9 Summary

In this chapter, I used a large survey of repeat spectra of dCs to constrain their orbital properties as a population. By measuring and constructing the RV variability distribution for the dCs and a comparable control sample, I was able to use a variety of methods to determine the following:

1. Using the extreme deconvolution method I found that the dC ΔRV distribution contains two components, a central core and a large ΔRV tail. A comparable control sample is best fit by a single component. The large ΔRV tail is indicative of close binaries amid the dC population.

2. Fitting binary system population models to the dC ΔRV distribution results in a binary fraction of 95%, within the errors of the expected 100% for the binary formation pathway of dCs. This suggests that the formation of dCs is indeed via mass transfer of carbon right material onto a normal main-sequence star.

3. Fitting a bimodal separation model to the dC ΔRV distribution results in the two components having mean separations of 0.3 AU and 1.15 AU. Assuming a standard WD mass of $0.6\,M_{\odot}$ and with a dC mass range of $[0.2\,M_{\odot},\ 1.0\,M_{\odot}]$ results in mean periods ranging from [250 d, 500 d]. Outliers in the dC ΔRV represent the closest systems that may have undergone a common-envelope phase and do not seem to be represented by this model fit.

4. Based on the model separation distribution and the observed dC ΔRV distribution there is not one single method of mass transfer, but dCs may experience any one of wind accretion, wind-RLOF, RLOF, and even accretion during a CE phase. In some cases, a single dC may experience all of these mass transfer mechanisms as the orbit evolves bringing the two components closer together.

Chapter 3

Photometrically Variable Dwarf Carbon Stars

In this chapter, I searched for and analyzed photometrically periodic dCs in the Zwicky Transient Facility. As few dC periods have previously been known, I aimed to find a new sample of periodic dCs and use them to constrain the dC formation pathway further. From almost 900 dCs with light curves, I found 34 dCs with previously unknown periodic variability. Interestingly, a majority of these periods are $< 2\,\mathrm{d}$, implicating these dCs as post-common-envelope binaries. I explore the possibility of whether the dCs could have accreted enough carbon-rich mass via the CE phase and how the dC properties compare to the wider population of post-common-envelope binaries. I also performed multi-epoch follow-up spectroscopy for a few of these new periodic dCs, confirming their photometric periods as orbital. Finally, I provide motivation for more follow-up of these dCs, as they represent an exciting new population for studying a variety of astrophysical processes, including CEE. The contents of this chapter have been published in Roulston et al. (2021).

3.1 Motivation

Until 2021, the known dC periods spanned from $\sim 1\,\mathrm{d}$ to $\sim 4100\,\mathrm{d}$, indicating different formation pathways. The longest dC periods that are of order tens of years

likely experienced only standard RLOF or possibly wind-RLOF. These periods are consistent with other types of post-mass-transfer systems, such as the blue straggler stars. The dCs with periods $\lesssim 10\,\mathrm{d}$ would have likely experienced CEE (Paczynski, 1976; Ivanova et al., 2013) since the TP-AGB envelope expands to several hundreds of solar radii. Of interest is how CEE affects dC formation.

Once the CE phase has started, the plunge-in of the lower-mass companion (in our case, the future dC) would truncate the evolution of the AGB by ejection of its envelope. If this happens before the TP-AGB phase and the third dredge-up, the C enhancement needed for dC formation will not occur. However, if the CE begins after the AGB companion has already become a C-giant, then it may be possible for the main-sequence companion to accrete enough C-rich material from the CE to become a dC (depending on the accretion efficiency and duration). If the accretion efficiency is not high enough, however, the main-sequence companion will not accrete enough material from the CE alone, requiring some combination of CE evolution with efficient mass transfer before the CE phase that is sufficient to transform an O-rich main-sequence star into a C-rich dC.

Significant accretion of mass and angular momentum from the AGB companion could result in significant spin-up and subsequent activity in some dCs (Green et al., 2019b). If there are dCs left in very tight orbits with the WD remnant, they may show tidally locked rotation periods (synchronous rotation), as well as tidal distortions causing ellipsoidal variations in photometric light curves. A search for periodicity in photometrically variable dCs could reveal some systems useful for constraining their evolution.

Another motivation to study variability in dCs is that no dC masses have yet been dynamically determined because there are no known eclipsing dC systems. It

may be possible to estimate dC masses from optical or infrared (IR) colors (see Section 3.6.2), but these estimates have uncharacterized systematics due to differences between normal O-rich stars and C stars in the optical and IR regions.

This lack of eclipsing dC systems highlights the importance of photometric surveys to search for the first well-characterized eclipsing dC systems. These systems could, when combined with RV follow-up, provide the first reliable dC mass measurements and help us understand more about the amount, and composition, of accreted mass needed to form a dC.

Margon et al. (2018) conducted a search for periodic dCs using the Palomar Transient Factory (PTF; Law et al., 2009; Rau et al., 2009), finding just one periodic dC. However, they clearly highlighted the potential for large photometric surveys to find periodic dCs, particularly dCs with short periods that should have experienced the strongest phases of CE mass transfer. In their recent work, Whitehouse et al. (2021) conducted an RV survey of seven dCs with Hα emission, finding short orbital periods for all of them (six new periods). In addition, they found photometric periods with similar lengths as the orbital periods in the range of 0.2–5.2 d. Their light curve modeling suggests that the source of variability in their dCs is stellar rotation and spots. As with the new photometrically periodic dCs in this chapter, these dCs must have experienced a CE phase with the former AGB companion.

In this chapter, I report on a unique sample of close binary dCs — implicating them as post-common envelope binaries (PCEBs) and likely pre-CVs — discovered from their periodic photometric variability in the Zwicky Transient Facility. In Section 3.2 I describe the sample of dCs selected to search, and in Section 3.3 I detail the process for cleaning and preparing the raw light curves. In Section 3.4 I describe the process for finding which dCs have detected periodic signals. In Section 3.5 I

present spectroscopic follow-up for four of the periodic dCs in this chapter. Finally, in Section 3.6 I present comparisons of these short-period dCs to binary population synthesis models to understand how a common-envelope phase relates to dC formation.

3.2 Sample Selection

To search for variability in as many dCs as possible, I compiled a list of all dCs from the current literature. The largest contributor (747 dCs, 79%) is the Green (2013) sample of carbon stars from the SDSS. I also selected a smaller number of dCs from Si et al. (2014), who found 96 new dCs using a label propagation algorithm from SDSS DR8, and from Li et al. (2018) who selected carbon stars from the Large Sky Area Multi-Object Fiber Spectroscopic Telescope survey (LAMOST; Cui et al., 2012) using a machine learning approach. The resulting final sample consists of 944 dCs.

With the compiled sample, to ensure that any periodic candidate was indeed a dwarf carbon star, I used Gaia EDR3 parallaxes, proper motions (Gaia Collaboration et al., 2021) and distances (Bailer-Jones et al., 2021). I required that each periodic C star had $M_G > 5$ mag from Gaia EDR3 based either on (1) significant parallax $\varpi/\varpi_{\rm err} > 5$ (27/34 periodic dCs) or (2) a significant proper motion ($\mu/\sigma_\mu > 5$) which sets an upper limit on the dC distance by limiting its transverse velocity to be less than an assumed Galactic escape velocity (Smith et al., 2007) of about 600 km/s (7/34 periodic dCs).

Table 3.1: Statistics of the light curves in the three ZTF filters. For each filter the number of stars, the mean number of epochs, the standard deviation of the number of epochs, the mean magnitude, and the mean magnitude error are reported.

Filter	$N_{\rm stars}$	$< N_{\rm epochs} >$	$\sigma_{\rm N_{epochs}}$	$<$ mag $>$	$< \sigma_{\rm mag} >$
ZTF g	833	185	204	19.32	0.11
ZTF r	867	269	237	18.07	0.05
ZTF i	554	31	22	17.81	0.05

3.3 Light Curve Processing

Using the list of dCs, I cross-matched the sample to the Zwicky Transient Facility DR5 (ZTF; Bellm et al., 2019; Masci et al., 2019; Graham et al., 2019). I required a match to be within $2''$ of the target coordinates and each star having ≥ 10 epochs in the available ZTF filters.

From the resulting matches detected within each filter, I grouped all sources within the match distance to ensure all epochs for each dC were included. The final sample of light curves resulted in 833 dCs with ZTF g light curves, 867 dCs with ZTF r light curves, and 554 dCs with ZTF i light curves. For each light curve, I only used epochs for which the ZTF flag `catflags` $== 0$ (no ZTF flags), ensuring every epoch is of high quality. I summarize the light curve sample for each filter in Table 3.3.

I checked for any epochs which appear to be discrepant by performing an outlier removal on all the light curves. I first select from the raw light curve the brightest and faintest 5% of epochs. Within this brightest and faintest 5%, I calculate the median magnitude of each (i.e. the median of the 5% brightest and 5% faintest) and the mean error of that same brightest and faintest 5%. I then removed any outliers that were 2σ brighter than the median of the brightest 5%, and removed those 2σ fainter than the median of the faintest 5%. If this selection dropped the number of epochs below 10, I removed that light curve from the analysis. This treatment rejects

most artifacts without removing genuine astrophysical variability.

I checked the light curves for each dC, in each filter, to determine if each dC had detected variability by examining how the mean magnitude changed across the observed light curve time span. A small number of dCs that show no periodic variability in my analysis in Section 3.4 (and a few periodic dCs) show signs of non-periodic variability, as well as secular, long-term trends. These non-periodic but variable dCs are of interest and may be signs of flaring, variable obscuration, or perhaps accretion onto the WD companion. They warrant further investigation, but I do not discuss them further in this dissertation.

The light curves that show long-term trends of brightening or dimming on timescales of hundreds of days cause the mean magnitude to vary over the entire time span of the light curve. This variable mean magnitude can cause issues with the period search. Therefore, I removed these long-term trends by fitting out a third-order polynomial to the raw light curve.

3.4 Periodic Variability

For each light curve, I searched for periodic signals down to a minimum period of 0.1 d using the Lomb-Scargle periodogram (LS; Lomb, 1976; Scargle, 1982). I used the Astropy (Astropy Collaboration et al., 2018) implementation of the LS algorithm (VanderPlas et al., 2012; VanderPlas & Ivezić, 2015). I selected the highest peak, and if this peak corresponds to an observational alias (1d, 29.5d, 1yr, etc.) or a harmonic of one of these aliases (1/2, 1/3, 1/4, 1/5, 2, 3, 4, 5), I removed that signal from the light curve and recalculated the periodogram until the highest-power frequency was not an alias (I counted a frequency not as an alias if it was more than 150 frequency bins away from the pure alias frequency, i.e. more than 0.005 d^{-1} away from an alias).

For the highest remaining peak, I calculated the false-alarm probability (FAP; VanderPlas, 2018). I required that $\log(\mathrm{FAP}) \leq -5$ in at least one filter for the selection a specific dC as a periodic candidate, more conservative than e.g., the $\log(\mathrm{FAP}) \leq -3$ used in the recent ZTF periodic variable catalog of Chen et al. (2020).

For the dCs which have light curves selected as periodic candidates, I checked for any possible harmonic confusion in the found period. For each dC, in each filter, I plot a power spectrum from the LS analysis. This is used to determine how strong the highest-power frequency is compared to the $\log(\mathrm{FAP})$ limit and the background peaks. Figure 3.1 shows an example power spectrum for an object with a very strong periodic signal and shows clear peaks (with 1-d aliasing) above the background, and the resulting phased light curve. The complete figure set (90 figures) is available in the online journal.

In some cases, the strongest peaks were aliases, typically harmonics of 1 month, that overwhelmed the power spectrum. For these dCs, I inspected each power spectrum in conjunction with phased light curves. If another non-alias peak (i.e., with a frequency more than 0.005 d^{-1} away from an alias) was found in the power spectrum meeting the FAP limit, that new peak was selected as the period for that dC. If no non-alias peaks could be found, the dC candidate was removed from the sample.

Some dCs show strong periodic signals in one filter, but do not reach the FAP limit in the other available filters. For these dCs, if one filter has a period that meets the FAP limit and that period is visible in the other filter, I include that second filter even if its FAP does not meet the limit. This makes it possible for some dCs to have a $\log(\mathrm{FAP}) \geq -5$ in a filter if they have $\log(\mathrm{FAP}) \leq -5$ in another filter.

For all periodic dC candidates selected after inspection of their power spectra, I

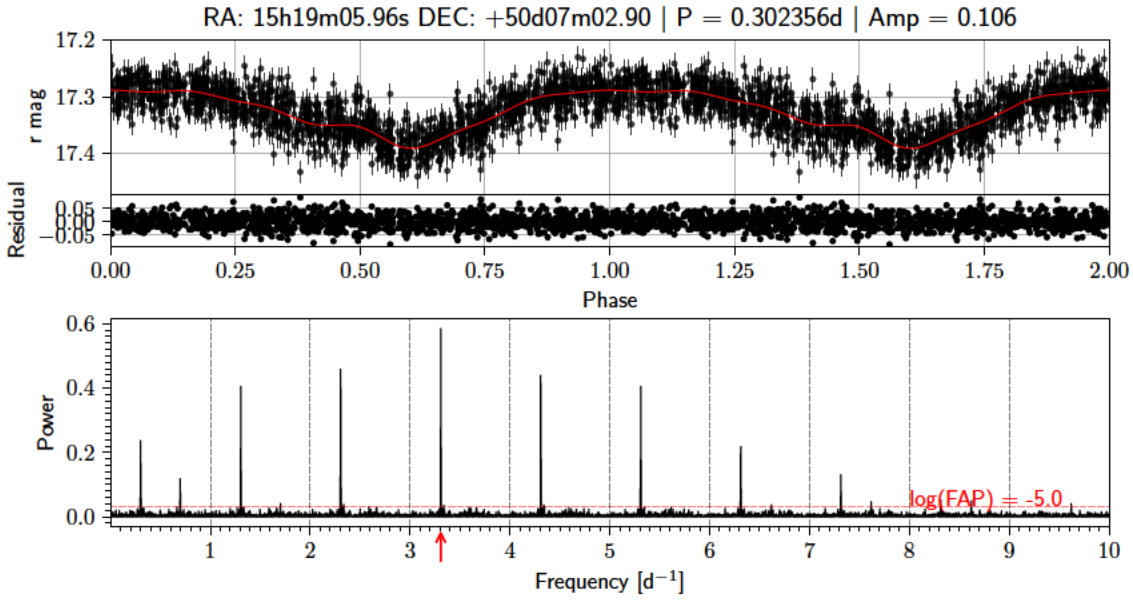

Figure 3.1: Phased light curves and power spectra for all periodic dC candidates. This example light curve and power spectrum is for the dC SDSS J151905.96+500702.9. This dC shows a clear and strong signal at $3.3\,\mathrm{d}^{-1}$ (with 1-d aliasing) that stands out above the low noise background in the power spectrum. The red horizontal line represents the peak height needed for a signal to meet the $\log(\mathrm{FAP}) \leq -5$ criterion. Grey vertical dashed lines mark the 1-d aliases caused by gaps in data collection, and the best period from the analysis is marked by an arrow. The highest significance peak is used to fold the observed light curve, yielding the phase-folded light curve in the top panel. Each light curve is plotted twice in phase to clearly show the periodic variability. The data are shown as the black points with their respective error bars, and the best-fitting model (see Section 3.4) is marked by the red solid line. The residuals are shown below the light curve. The complete figure set (35 figures) is available in the online journal.

plotted phased light curves folded on the highest selected peak period. In addition, I plotted 8 different harmonics of that period (1/2, 1/3, 1/4, 1/5, 2, 3, 4, 5) to check for aliases caused by gaps in the observational coverage. Using this plot, I calculated model-fit statistics (χ^2) and selected which period harmonic has the best model fit. I used the best period to phase the light curve, to which the final periodic model is fitted with.

The best-fit models were computed using the automatic Fourier decomposition (AFD) method, as detailed in Torrealba et al. (2015). I set an upper limit on the number of Fourier series terms of $n_{max} = 6$ to reduce over-fitting. No significant non-harmonic terms were included; though one dC, LAMOST J062558.33+023019.4, showed different peaks in its power spectrum between the g and r filters with the second highest peak in each filter being the highest peak in the other. The best AFD model was used to calculate the amplitude and epoch of the brightest time (t_0) for each light curve. I removed any dC for which the folded light curve shows no clear periodic signal or for which the amplitude of the variability was less than 0.005 mag. For dCs with multiple filters, I used the period from the filter with the strongest detection as the selected period and force the fits in the other filters to this fixed period. Some filters may not have a clear detection from the signal found in another filter, resulting in model fits with large errors for that filter. Figure Set 1 contains the folded light curves, models, and power spectra for all the periodic dC candidates.

Table 3.4 contains the properties for this final periodic dC sample. I estimated errors for the best found period using a MCMC method. For each dC, in each filter with a detected period, I started 50 MCMC walkers in a Gaussian around the detected period. I sampled the walkers for 10,000 steps each, at each step using the phase dispersion minimization technique (Stellingwerf, 1978) to calculate the likelihood at

each walker position. I used the 1σ of the marginalized period distribution as the photometric period error for that dC. However, this is only a statistical error and does not account for the possibility that I have selected an alias rather than the true period.

The final dC sample contains 34 individual dCs that are periodic in at least one ZTF filter. Given the wide initial orbits necessary for progenitor dC systems to avoid truncation of the TP-AGB phase before enough C-rich material can be transferred, it is remarkable that 19 (56%) of these dCs have periods $< 1\,\mathrm{d}$ (and 28 (82%) of these dCs have periods $< 2\,\mathrm{d}$), indicating they should have experienced a CE phase. The likely origins of the variability in these dCs include spot rotation on the dC or tidal distortion of the dC atmosphere from being in a close orbit with a WD. Since many of these dCs have short periods, I assume that these systems would have experienced a CE phase and have circularized and synchronized (Hurley et al., 2002). However, if the light curve variability is from the dC being tidally distorted, the detected period would be half the orbital period (even with $2\times$ longer true orbital periods, these systems should still have experienced a CE phase).

In addition, the 1 d aliasing caused by the observing window function causes peaks at frequencies of $\pm 1\,\mathrm{d}^{-1}$. These alias peaks can also meet the log (FAP) limit (see Figure 3.1), and while I take the highest significance peak from the filter which produces the best fitting model (via a χ^2 fit) there is a possibility this is the wrong period. This can only be solved by either low cadence photometry or confirming the photometric period with RV follow-up. For example, the dC SBSS 1310+561 has $\pm 1\,\mathrm{d}^{-1}$ aliases the meet the log (FAP) limit. In my initial search using ZTF DR3 data, the g and r filters had different highest peaks, with the best period in the g filter being $\sim$5.18 d and the best period in the r filter being $\sim$0.838 d. These are separated exactly by the

$1\,\mathrm{d}^{-1}$ aliasing of the window function, with the r filter providing a better model fit. However, using the newest (and larger) ZTF DR5 data set results in both the g and r filters having the same highest peak, at $5.1878 \pm 0.0012\,\mathrm{d}$. Whitehouse et al. (2021) confirmed this as the period with their RV observations of this dC.

The recent work by Whitehouse et al. (2021) included modeling of light curves for their sample of periodic dCs. They examined whether spot rotation, tidal distortion or irradiation by a hot WD companion could be the source of the photometric variability in their dC sample. They found that for periods near and longer than 1 d, both tidal distortion and irradiation are reduced to levels that would not be detectable in the light curves. While tidal distortion could be detectable for the shortest period dCs here ($0.1 < \mathrm{P} < 0.2\,\mathrm{d}$), the predicted amplitudes at these periods from Whitehouse et al. (2021) are larger than those found in this sample (as was the case for their sample). The irradiation modeling of Whitehouse et al. (2021) (which assumes a WD temperature from 30,000 K to 20,000 K) predicts amplitudes large enough to be detected. However, the majority of the dC amplitudes found here are smaller than predicted by those models, suggesting irradiation is not the source of variability for most of these dCs. Additionally, the majority of the dCs in my sample are mid- and late-type dCs (see Roulston et al., 2019) which do not have a visible WD in their optical spectra. This sets a limit that for these types, the WD must be cooler than about 10,000 K, reducing the irradiation effects below the detection limits. Only the composite dC+WD systems which have a hot WD (like SDSS J151905.96+500702.9) may have detectable irradiation effects. This leaves spot rotation as the most likely source of variability in my periodic dC sample. However, the origin of the variability in these dCs is not truly confirmed without comparison to spectroscopic RV follow-up.

Finally, as the ZTF survey continues to accrue more data I expect to find more

photometrically variable dCs from the current sample of known dCs. However, even given a favorable inclination (say $i > 85°$) the ZTF errors are too large for the detection of an eclipse of a cool WD in these systems. Using my estimated dC radii and luminosities and assuming a WD companion with a standard mass of $0.6M_{\odot}$ and temperature of 7000K (the WD component in the optical spectra should be visible if it is any hotter than this) there would only be expected an average primary eclipse depth of 0.005 mag. This is below the detection threshold with ZTF, with the dCs having median errors of 0.019 mag, compared to their median amplitude of 0.059 mag. The Vera Rubin Observatory's LSST survey (Ivezić et al., 2019) is expected to have errors of approximately 0.005 mag for a point source with r = 19.0, which may allow for the detection of dC eclipses. However, the majority of known dCs reside outside the LSST footprint, with 17% below the declination cut off of $\delta = +2°$ (Ivezić et al., 2019). Detection and characterization of the first eclipsing dC system will likely require dedicated observations with high cadence and low photometric noise.

Table 3.2: Periodic properties of dwarf carbon stars found in this chapter. For each dC, I list light curve properties of the observed ZTF filter, the mean magnitude and mean magnitude error. I include the selected best period, the logarithm of the false-alarm-probability for that period, the amplitude of variability from the best fit model at that period, and the time of light curve maximum brightness. Finally, I include a few diagnostics including the number of terms in the model fit and the resulting reduced χ^2 of the model.

Index[a]	R.A. (J2016.0)	Decl. (J2016.0)	Filter	$N_{\rm good}$	$N_{\rm rejects}$	$<$ mag $>$ [mag]	$<\sigma_{\rm mag}>$ [mag]	P [d]	$\sigma_{\rm P}$ [d]	$\log_{10}$ FAP	Amp [mag]	$\sigma_{\rm Amp}$ [mag]	t_0 [d]	σ_{t_0} [d]	$N_{\rm terms}$	$\chi^2_{\nu,\rm fit}$
1*	00h47m06.76s	+00d07m48.80s	g	183	0	19.81	0.12	12.614	0.010	>-1.0	0.044	0.051	59217.686	0.022	1	1.18
2	00h47m06.76s	+00d07m48.80s	r	243	1	18.352	0.043	12.614	0.010	-8.9	0.058	0.015	59217.383	0.022	1	0.87
3*	01h31m19.05s	+37d20m25.30s	g	179	2	18.555	0.037	1.376804	0.000079	>-1.0	0.055	0.015	59066.1913	0.0014	1	2.42
4*	01h31m19.05s	+37d20m25.30s	i	27	0	16.906	0.020	1.376804	0.000079	>-1.0	0.026	0.022	58746.5621	0.0014	1	1.73
5	01h31m19.05s	+37d20m25.30s	r	236	1	17.266	0.017	1.376804	0.000079	-21.1	0.0553	0.0063	59067.5006	0.0014	1	2.17
6	02h35m30.65s	+02d25m18.58s	g	209	1	17.993	0.031	1.65926	0.00019	-3.3	0.050	0.012	59232.6027	0.0017	1	2.26
7	02h35m30.65s	+02d25m18.58s	r	229	1	16.673	0.015	1.65926	0.00019	-10.1	0.0416	0.0080	59232.6126	0.0017	2	2.37
8	02h54m14.24s	+26d21m54.19s	g	255	2	15.598	0.012	0.190058	0.000018	-11.5	0.0351	0.0043	59232.01892	0.00019	1	9.73
9	02h54m14.24s	+26d21m54.19s	r	262	3	14.529	0.010	0.190058	0.000018	-4.7	0.0228	0.0033	59232.00485	0.00019	1	10.03
10	04h16m05.11s	+50d28m28.52s	g	293	0	14.375	0.013	6.8083	0.0018	-7.5	0.0212	0.0044	59228.4734	0.0070	1	1.66
11	04h16m05.11s	+50d28m28.52s	r	317	1	13.601	0.012	6.8083	0.0018	-6.6	0.0163	0.0054	59227.6972	0.0070	2	1.20
12*	05h02m40.82s	+40d23m23.59s	g	72	0	18.414	0.037	4.42791	0.00096	>-1.0	0.060	0.025	58750.1829	0.0045	1	2.32
13	05h02m40.82s	+40d23m23.59s	r	294	0	17.124	0.019	4.42791	0.00096	-32.6	0.0646	0.0063	59233.0912	0.0045	1	1.81
14	06h25m58.34s	+02d30m19.43s	g	157	0	14.589	0.015	7.6080	0.0014	-13.6	0.0660	0.0067	59227.6546	0.0077	1	3.51
15	06h25m58.34s	+02d30m19.43s	r	176	2	13.885	0.010	7.6080	0.0014	-16.6	0.0497	0.0043	59227.4415	0.0077	1	7.68
16	07h44m47.66s	+51d38m31.76s	g	220	2	17.506	0.022	1.534684	0.000071	-1.4	0.0435	0.0084	59230.5473	0.0015	1	3.88
17	07h44m47.66s	+51d38m31.76s	r	279	1	16.122	0.011	1.534684	0.000071	-20.5	0.0426	0.0055	59232.0743	0.0015	2	3.62
18*	08h11m57.14s	+14d35m33.00s	g	116	2	16.035	0.014	0.750413	0.000041	>-1.0	0.0150	0.0069	59230.04781	0.00075	1	2.42
19	08h11m57.14s	+14d35m33.00s	r	210	0	15.742	0.013	0.750413	0.000041	-14.3	0.0541	0.0059	59232.20075	0.00075	1	3.11
20*	09h14m58.08s	+21d56m39.65s	g	108	0	16.839	0.016	1.23573	0.00014	>-1.0	0.0366	0.0090	59231.8032	0.0012	1	7.97

Table continued on next page

(continued)

Index[a]	R.A. (J2016.0)	Decl. (J2016.0)	Filter	$N_{\rm good}$	$N_{\rm rejects}$	$<$ mag $>$ [mag]	$<\sigma_{\rm mag}>$ [mag]	P [d]	$\sigma_{\rm P}$ [d]	$\log_{10}$ FAP	Amp [mag]	$\sigma_{\rm Amp}$ [mag]	t_0 [d]	σ_{t_0} [d]	$N_{\rm terms}$	$\chi^2_{\nu,\rm fit}$
21	09h14m58.08s	+21d56m39.65s	r	202	2	15.330	0.010	1.23573	0.00014	-7.1	0.0471	0.0045	59231.8045	0.0012	1	7.59
22*†	09h33m24.58s	-00d31m44.07s	g	107	0	15.308	0.013	1.15693	0.00014	>-1.0	0.0091	0.0072	59231.8412	0.0012	1	3.66
23†	09h33m24.58s	-00d31m44.07s	r	268	3	13.989	0.011	1.15693	0.00014	-14.2	0.0196	0.0036	59231.4432	0.0012	1	1.75
24*	09h40m26.28s	+36d25m48.81s	g	261	1	19.79	0.12	1.9573	0.0012	>-1.0	0.070	0.040	59228.7471	0.0023	1	1.32
25*	09h40m26.28s	+36d25m48.81s	i	22	0	17.740	0.038	1.9573	0.0012	>-1.0	0.004	0.044	58627.9758	0.0023	1	1.50
26	09h40m26.28s	+36d25m48.81s	r	581	3	18.241	0.038	1.9573	0.0012	-14.6	0.044	0.0082	59230.8844	0.0023	1	1.35
27*	12h02m46.01s	+54d19m29.24s	g	249	0	20.68	0.21	1.15516	0.00024	>-1.0	0.045	0.074	59231.1841	0.0012	1	1.14
28*	12h02m46.01s	+54d19m29.24s	i	22	0	18.397	0.053	1.15516	0.00024	>-1.0	0.038	0.065	58651.6814	0.0012	1	0.92
29	12h02m46.01s	+54d19m29.24s	r	460	0	18.917	0.073	1.15516	0.00024	-5.9	0.056	0.019	59231.3031	0.0012	1	0.71
30	12h08m53.35s	-00d08m47.99s	g	59	0	19.66	0.10	0.350882	0.000012	-5.7	0.214	0.076	59234.43466	0.00035	1	0.63
31*	12h08m53.35s	-00d08m47.99s	r	92	1	18.701	0.063	0.350882	0.000012	>-1.0	0.019	0.037	59231.29497	0.00035	1	1.62
32*	12h10m06.99s	+58d43m18.34s	g	441	1	17.998	0.038	0.183532	0.000010	>-1.0	0.005	0.011	59232.46412	0.00018	1	1.79
33*	12h10m06.99s	+58d43m18.34s	i	25	0	16.577	0.014	0.183532	0.000010	>-1.0	0.074	0.020	58652.08785	0.00018	1	13.89
34	12h10m06.99s	+58d43m18.34s	r	616	5	16.868	0.017	0.183532	0.000010	-7.6	0.0366	0.0055	59232.47201	0.00018	2	5.62
35*†	12h23m57.62s	+55d01m51.43s	g	856	3	19.074	0.078	0.336288	0.000032	>-1.0	0.072	0.036	59231.38908	0.00034	6	1.26
36*†	12h23m57.62s	+55d01m51.43s	i	53	0	16.977	0.020	0.336288	0.000032	>-1.0	0.034	0.026	58675.06583	0.00034	2	1.00
37†	12h23m57.62s	+55d01m51.43s	r	1001	4	17.399	0.022	0.336288	0.000032	-16.2	0.0257	0.0057	59231.46542	0.00034	2	1.20
38	12h30m45.52s	+41d09m43.45s	g	682	4	18.362	0.041	0.882519	0.000020	-14.6	0.0545	0.0089	59231.23169	0.00088	1	1.76
39*	12h30m45.52s	+41d09m43.45s	i	46	0	15.788	0.015	0.882519	0.000020	>-1.0	0.016	0.012	58647.83545	0.00088	1	1.06
40	12h30m45.52s	+41d09m43.45s	r	624	0	16.566	0.019	0.882519	0.000020	-57.7	0.0417	0.0042	59229.43135	0.00088	1	1.10
41*	13h03m59.18s	+05d09m38.62s	g	105	0	18.361	0.039	1.84149	0.00014	>-1.0	0.048	0.021	59229.5733	0.0018	1	2.12
42*	13h03m59.18s	+05d09m38.62s	i	23	0	16.757	0.019	1.84149	0.00014	>-1.0	0.041	0.027	58651.6711	0.0018	1	3.87
43	13h03m59.18s	+05d09m38.62s	r	124	0	17.101	0.020	1.84149	0.00014	-10.5	0.070	0.015	59231.6633	0.0018	2	2.10
44	13h12m42.27s	+55d55m54.84s	g	403	4	15.845	0.014	5.1878	0.0012	-8.1	0.0439	0.0068	59229.5411	0.0053	3	6.00

Table continued on next page

(continued)

Index[a]	R.A. (J2016.0)	Decl. (J2016.0)	Filter	$N_{\rm good}$	$N_{\rm rejects}$	$<{\rm mag}>$ [mag]	$<\sigma_{\rm mag}>$ [mag]	P [d]	$\sigma_{\rm P}$ [d]	$\log_{10}$FAP	Amp [mag]	$\sigma_{\rm Amp}$ [mag]	t_0 [d]	σ_{t_0} [d]	$N_{\rm terms}$	$\chi^2_{\nu,{\rm fit}}$
45	13h12m42.27s	+55d55m54.84s	i	35	0	13.560	0.014	5.1878	0.0012	-1.1	0.034	0.016	58659.3606	0.0053	1	1.19
46	13h12m42.27s	+55d55m54.84s	r	402	2	14.121	0.012	5.1878	0.0012	-28.1	0.0343	0.0035	59230.0028	0.0053	1	2.50
47	13h31m23.61s	+48d26m24.37s	g	314	4	20.276	0.154	0.203571	0.000043	-5.5	0.43	0.12	59231.42815	0.00021	6	2.13
48*	13h31m23.61s	+48d26m24.37s	i	29	0	18.194	0.040	0.203571	0.000043	>-1.0	0.020	0.041	58661.03320	0.00021	1	0.55
49*	13h31m23.61s	+48d26m24.37s	r	437	4	18.640	0.045	0.203571	0.000043	>-1.0	0.008	0.012	59233.29307	0.00021	1	1.14
50*	14h09m53.08s	-06d11m41.71s	g	184	1	15.275	0.014	0.319873	0.000014	>-1.0	0.0114	0.0060	59231.23975	0.00032	1	3.87
51*	14h09m53.08s	-06d11m41.71s	i	20	0	13.995	0.014	0.319873	0.000014	>-1.0	0.011	0.018	58652.94999	0.00032	1	1.88
52	14h09m53.08s	-06d11m41.71s	r	260	0	14.268	0.013	0.319873	0.000014	-5.6	0.0208	0.0067	59232.20001	0.00032	2	1.62
53	14h15m15.24s	+51d41m28.01s	g	322	0	20.64	0.20	0.272819	0.000018	-5.2	0.197	0.062	59231.22128	0.00027	1	1.06
54*	14h15m15.24s	+51d41m28.01s	i	35	0	19.47	0.11	0.272819	0.000018	>-1.0	0.040	0.098	58711.95424	0.00027	1	1.48
55*	14h15m15.24s	+51d41m28.01s	r	539	1	19.67	0.11	0.272819	0.000018	>-1.0	0.026	0.026	59231.27530	0.00027	1	0.69
56*	15h11m44.58s	+38d59m10.46s	g	509	2	18.768	0.055	0.335548	0.000082	>-1.0	0.009	0.014	59202.32548	0.00034	1	2.09
57*	15h11m44.58s	+38d59m10.46s	i	45	0	16.702	0.017	0.335548	0.000082	>-1.0	0.010	0.016	58733.05657	0.00034	1	1.18
58	15h11m44.58s	+38d59m10.46s	r	570	1	17.217	0.020	0.335548	0.000082	-5.2	0.0179	0.0066	59202.22985	0.00034	2	1.23
59	15h15m42.72s	+52d01m45.47s	g	529	7	18.661	0.044	0.332473	0.000097	-5.0	0.067	0.019	59231.21797	0.00033	3	2.37
60*	15h15m42.72s	+52d01m45.47s	r	527	6	17.253	0.018	0.332473	0.000097	>-1.0	0.0092	0.0046	59231.48893	0.00033	1	3.45
61	15h19m05.93s	+50d07m03.14s	g	1279	5	17.609	0.023	0.302356	0.000021	-10.2	0.0184	0.0052	59231.41069	0.00030	2	1.18
62	15h19m05.93s	+50d07m03.14s	i	104	0	17.005	0.021	0.302356	0.000021	-11.6	0.132	0.017	58733.12921	0.00030	2	3.19
63	15h19m05.93s	+50d07m03.14s	r	1281	6	17.325	0.018	0.302356	0.000021	-238.8	0.1061	0.0072	59233.23027	0.00030	6	2.03
64	15h24m34.12s	+44d49m55.84s	g	236	1	20.85	0.19	0.251714	0.000012	-5.1	0.36	0.12	59231.38694	0.00025	3	1.22
65*	15h24m34.12s	+44d49m55.84s	i	23	0	18.693	0.065	0.251714	0.000012	>-1.0	0.009	0.079	58669.14143	0.00025	1	0.74
66*	15h24m34.12s	+44d49m55.84s	r	448	1	19.206	0.067	0.251714	0.000012	>-1.0	0.025	0.018	59233.37775	0.00025	1	1.16
67*	15h25m04.49s	+32d25m10.90s	g	412	3	21.06	0.20	0.13712	0.000013	>-1.0	0.27	0.13	59232.50195	0.00014	5	1.96
68*	15h25m04.49s	+32d25m10.90s	i	97	0	19.198	0.083	0.13712	0.000013	>-1.0	0.030	0.045	58733.08198	0.00014	1	2.62

Table continued on next page

(continued)

Index[a]	R.A. (J2016.0)	Decl. (J2016.0)	Filter	$N_{\rm good}$	$N_{\rm rejects}$	$<$ mag $>$ [mag]	$<\sigma_{\rm mag}>$ [mag]	P [d]	$\sigma_{\rm P}$ [d]	$\log_{10}$ FAP	Amp [mag]	$\sigma_{\rm Amp}$ [mag]	t_0 [d]	σ_{t_0} [d]	$N_{\rm terms}$	$\chi^2_{\nu,{\rm fit}}$
69	15h25m04.49s	+32d25m10.90s	r	1001	3	19.557	0.088	0.13712	0.000013	-5.4	0.070	0.016	59232.43462	0.00014	1	2.11
70*	15h30m59.26s	+45d12m00.33s	g	504	1	18.095	0.032	13.587	0.011	>-1.0	0.0389	0.0082	59090.790	0.018	1	2.65
71*	15h30m59.26s	+45d12m00.33s	i	36	0	16.059	0.014	13.587	0.011	>-1.0	0.027	0.014	58721.469	0.018	1	1.61
72	15h30m59.26s	+45d12m00.33s	r	528	4	16.579	0.014	13.587	0.011	-25.6	0.0295	0.0036	59062.217	0.018	1	1.87
73*	15h35m32.92s	+01d10m16.22s	g	31	0	21.02	0.19	0.173866	0.000037	>-1.0	0.14	0.21	59038.20950	0.00018	1	0.80
74*	15h35m32.92s	+01d10m16.22s	i	23	0	18.514	0.053	0.173866	0.000037	>-1.0	0.019	0.062	58667.09530	0.00018	1	1.53
75	15h35m32.92s	+01d10m16.22s	r	177	0	19.061	0.085	0.173866	0.000037	-8.0	0.233	0.037	59231.42104	0.00018	1	2.33
76*	16h37m18.63s	+27d40m26.63s	g	544	4	19.295	0.064	1.22790	0.00010	>-1.0	0.048	0.022	59232.4009	0.0012	2	1.74
77*	16h37m18.63s	+27d40m26.63s	i	48	0	16.759	0.016	1.22790	0.00010	>-1.0	0.035	0.025	58732.2916	0.0012	3	1.21
78	16h37m18.63s	+27d40m26.63s	r	578	1	17.424	0.018	1.22790	0.00010	-7.5	0.0191	0.0043	59232.1419	0.0012	1	1.34
79*	16h59m02.30s	+25d05m49.00s	g	250	2	21.08	0.19	0.287694	0.000030	>-1.0	0.242	0.097	59232.53484	0.00029	2	2.65
80*	16h59m02.30s	+25d05m49.00s	i	54	0	18.769	0.056	0.287694	0.000030	>-1.0	0.049	0.043	58751.08757	0.00029	1	1.52
81	16h59m02.30s	+25d05m49.00s	r	628	6	19.358	0.064	0.287694	0.000030	-5.7	0.083	0.025	59232.43645	0.00029	3	2.73
82*†	19h23m55.93s	+44d58m32.20s	g	719	10	17.286	0.019	0.146029	0.000013	>-1.0	0.0058	0.0039	59194.06850	0.00015	1	2.82
83*†	19h23m55.93s	+44d58m32.20s	i	56	0	16.009	0.014	0.146029	0.000013	>-1.0	0.011	0.011	58748.21787	0.00015	1	1.74
84†	19h23m55.93s	+44d58m32.20s	r	1077	2	16.285	0.013	0.146029	0.000013	-15.3	0.0150	0.0032	59194.01389	0.00015	2	1.68
85	22h08m10.01s	+25d17m30.17s	g	218	2	15.724	0.014	0.422469	0.000014	-20.4	0.0454	0.0055	59223.02886	0.00042	1	20.78
86	22h08m10.01s	+25d17m30.17s	i	48	0	14.122	0.014	0.422469	0.000014	-3.0	0.032	0.012	58750.73006	0.00042	1	1.19
87	22h08m10.01s	+25d17m30.17s	r	291	1	14.548	0.014	0.422469	0.000014	-40.7	0.0541	0.0043	59228.94681	0.00042	1	2.20
88	23h41m30.74s	+15d19m43.20s	g	507	5	18.338	0.036	0.134337	0.000019	-97.1	0.1437	0.0088	59233.04549	0.00013	1	1.83
89	23h41m30.74s	+15d19m43.20s	i	81	0	17.513	0.028	0.134337	0.000019	-8.9	0.094	0.018	58751.30804	0.00013	1	1.36
90	23h41m30.74s	+15d19m43.20s	r	541	2	17.687	0.024	0.134337	0.000019	-121.7	0.1205	0.0059	59233.04603	0.00013	1	1.62

[a] — Rows marked with an * have a light curve with no detectable variability at the given period in this filter. The model fit for this filter is unreliable. dCs marked with †, while meeting all the criteria to be included, have suspect periods due to having more than 1% of the periodogram above the power needed to have $\log({\rm FAP}) \leq -5$.

3.5 Spectroscopic Follow-up

To constrain the origins of the photometric variability I have begun spectroscopic follow-up of the periodic dCs discovered here. I report spectroscopic follow-up for four of these dCs: SDSS J151905.96+500702.9, SDSS J123045.53+410943.8, LAMOST J062558.33+023019.4 (referenced further on as J1519, J1230, J0625 respectively) and SBSS 1310+561.

3.5.1 Spectroscopic Set-Up

The dCs J1519 and J1230 were observed with the Binospec spectrograph on the MMT telescope (Fabricant et al., 2019). For all observations, I used the 0.85″ slit with the 600 l mm^{-1} grating centered on 7250 Å, giving coverage from 6000 Å to 8000 Å covering Hα and the CN bands. The reduced spectra have a dispersion of 0.61 Å pix^{-1} with R≈3590. All Binospec data were reduced using the standard Binospec reduction pipeline[1] (Kansky et al., 2019).

The dC J0625 was observed with the Magellan Echellette (MagE; Marshall et al., 2008) spectrograph on the Magellan Baade Telescope. All observations used the 0.85″ slit and were reduced using the MagE reduction pipeline[2] (Chilingarian, 2020). The reduced spectra cover from about 3200 Å to 10000 Å with R≈4500.

Observations for SBSS 1310+561 were acquired at the 1.5m Fred Lawrence Whipple Observatory (FLWO) telescope with the FAST spectrograph (Fabricant et al., 1998) using the 600 l mm^{-1} grating and the 1.5″slit, which provides wavelength coverage from 6000 Å to 8000 Å at 1.5 Å spectral resolution.

[1] https://bitbucket.org/chil_sai/binospec/wiki/Home
[2] https://bitbucket.org/chil_sai/mage-pipeline/src/master/

3.5.2 SDSS J151905.96+500702.9

One of the more interesting dCs in the periodic sample found in this chapter, with photometric periodicity detected with highest significance, is SDSS J151905.96+500702.9 (also known as CBS 311; I use J1519 in the rest of this chapter), a dC+DA spectroscopic composite binary. J1519 was discovered by Liebert et al. (1994) and has been studied on numerous occasions (Farihi et al., 2010; Green, 2013; Whitehouse et al., 2018; Ashley et al., 2019; Roulston et al., 2019; Green et al., 2019b). However, this is the first reporting of its periodic variability.

J1519 ($r = 17.3\,\mathrm{mag}$) has four epochs of optical spectra in the SDSS, with the most recent spectrum shown in the top panel of Figure 3.2. The spectrum of J1519 shows a dC with a hot DA WD companion, as well as Hα emission. Whitehouse et al. (2018) and Roulston et al. (2019) found RV variability using few-epoch spectroscopy with ΔRV_{max} of 46.8 ± 15.8 km s^{-1} and 44 ± 20 km s^{-1}, respectively. Farihi et al. (2010) conducted a study of WD–red dwarf systems, including J1519, using the *Hubble Space Telescope*. They found J1519 to be unresolved, placing the constraint on its separation of $< 10\,\mathrm{au}$.

J1519 WD Model Fits

Since J1519 is a spectroscopic dC+DA composite, WD model atmospheres can be fit to the WD component to fit T_{Eff} and $\log(g)$ using the SDSS spectra. Bédard et al. (2020) fit WD models and found fit values of $31230 \pm 210\,\mathrm{K}$ and 7.97 ± 0.05 respectively.

Farihi et al. (2010) found that spectroscopically determined WD parameters are often biased due to a cool companion. To update the fits of Bédard et al. (2020), I performed my own model atmosphere fits to the DA component of J1519 using the synthetic WD model atmospheres of Levenhagen et al. (2017). I first fit the late-type

Table 3.3: Best fit model parameters for the DA component of SDSS J151905.96+500702.9. Each parameter lists the source used: (1) this chapter (2) from evolutionary models of Fontaine et al. (2001)

Parameter	Value	Error	Source
$T_{\rm eff}$ [K]	31000	500	(1)
$\log g$ [dex]	7.85	0.05	(1)
M [$M_\odot$]	0.57	0.02	(2)
R [$R_\odot$]	0.015	0.001	(2)
$T_{\rm cool}$ [Myr]	7.7	0.2	(2)

[a] — Parameter fixed during fitting.

dC (dCM) template of Roulston et al. (2020) to the SDSS spectrum of J1519 by finding the best-fit velocity, shifting the template, and then scaling it to the flux near Hα. I then removed the dC spectrum from the total spectrum, leaving just the WD component. I then fit the visible Balmer lines from Hβ and blue-ward to the entire grid of WD model spectra. I interpolated the grid of WD model spectra to include half-steps in the model space. The best-fitting model parameters for $T_{\rm Eff}$ and $\log(g)$ were 31000±500 K and 7.85±0.05, respectively, and can be seen in Figure 3.2. The black line is the single SDSS spectrum with the highest S/N shifted to the rest-frame, and the blue line is the best fit WD model spectrum. I did not use Hα for the WD fit as the dC component contributes most to the spectrum in emission. In addition, I did not use the H9 line, as only half of the line is visible in the SDSS spectrum.

The WD temperature of my fit is in good agreement with that of Bédard et al. (2020). However, my fit values of $\log(g)$ is 0.12 dex lower, resulting in both the WD mass and cooling age being lower than those in Bédard et al. (2020). For the purposes of this chapter, I adopt my fit values of $\log(g)$ and $T_{\rm Eff}$. The WD properties I use can be found in Table 3.5.2, with the mass, radius, and cooling age coming from the models of Fontaine et al. (2001).

J1519 Radial Velocities

Although RV variability has been detected in J1519, there are no published RV orbital fits for this system. Based on the photometric analysis, I found a period of 0.302356 ± 0.000021 d (~ 7 hr) for J1519. Therefore, I conducted spectroscopic monitoring of J1519 using the MMT spectroscopic setup as was described in Section 3.5.1. On the nights of 2020 August 19 and 20, I observed a sequence of 21×200 s exposures, on the night of 2020 August 22 I observed 27×200 s exposures, and on the nights of 2021 April 21 and 23 I observed 24×230 s exposures. The exposures on each night were then co-added in threes, resulting in seven final epochs on the first two nights, nine epochs on the third night, and eight on each of the last two nights for a combined total of 39 epochs (with about 600 s total exposure each), with an average S/N ≈ 5 for all epochs in the continuum region near Hα.

Since the full spectrum includes both stellar components, I measured the RV from the Hα emission line, presumed to come from the dC atmosphere alone. First, for each epoch, I re-scaled the late-type (dCM) dC template of Roulston et al. (2020) to the flux in the MMT spectrum in the region of 6300–6500 Å. I then used this as the model for the dC continuum level of that epoch, which was used to calculate the Hα emission line center, equivalent width, and associated errors. The RV measurements have an average error of approximately 5 km s^{-1}, and the equivalent width measurements have an average error of approximately 0.18 Å.

Figure 3.2 shows the measured RV (middle) and Hα equivalent widths (bottom) for J1519. To fit the RV curve, I used the `rvfit` program which uses a simulated adaptive annealing procedure, the details of which can be found in Iglesias-Marzoa et al. (2015). I left all parameters free to be fit, with the solution quickly converging to a circular orbit. I, therefore, refit the RV curve leaving all parameters free again

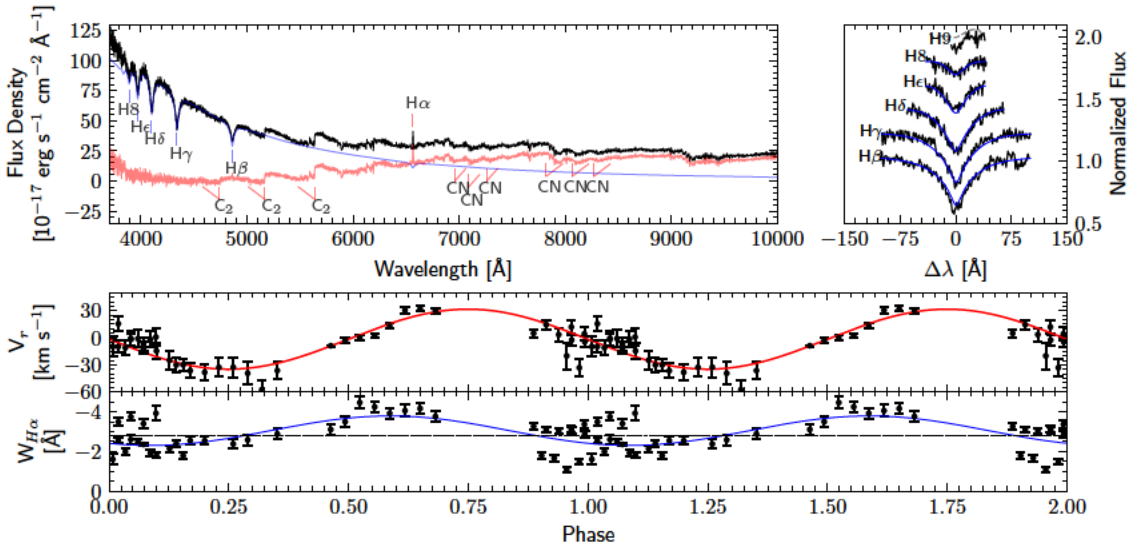

Figure 3.2: TOP: SDSS spectrum for the dC+DA SDSS J151905.96+500702.9, in black. The hot WD is visible, as are the carbon bands of C_2 and CN. The spectrum also shows Hα emission. The best-fitting model atmosphere to the DA component of the dC+WD composite J1519 is shown in blue, with the inset to the right showing a zoomed-in, stacked view of the Balmer lines used in the model fit (the black lines are the normalized flux of the WD component, and the blue lines are the best fitting model atmosphere, dashed grey lines means that the Balmer line was not used in the fit due to poor quality). The resulting dC component — simply the observed spectrum with the WD model subtracted — is shown in red. MIDDLE: RV as measured from the Hα line for J1519, phased on the time of periastron passage from the RV fit, and the fit RV period of 0.327526 d. The red solid line represents the best-fitting model. BOTTOM: Equivalent widths measured from the Hα line, phased on the fit RV period of 0.327526 d. The blue curve is the best-fit model to the data of a single sinusoid. The y-axis has been inverted so that smaller equivalent width values (more emission) are up.

except for the eccentricity, which I fix to $e = 0.0$. The resulting best-fit model can be seen in Figure 3.2 (red curve) and the fit parameters can be found in Table 3.5.5.

The best-fitting orbital period from the RVs (0.327526 ± 0.000012 d) is longer than the best photometric period by 0.025170 ± 0.000024 d (about 36 minutes). Fixing the period in the RV fitting procedure to that of the photometric period results in a poorer model fit, with the longer period model being a better fit at the 3.2σ level. The best-fit semi-amplitude of $K_2 = 33.3 \pm 1.4$ km s^{-1} ($\Delta RV_{\rm max} = 2K = 66.6$ km s^{-1}) is in agreement with the RV variations found by Whitehouse et al. (2018) and Roulston et al. (2019), as their random epochs likely did not catch the true RV amplitude. However, the low measured semi-amplitude suggests an extremely low inclination of this system, with $i \approx 10^{\circ}$ if I take the estimated dC mass of 0.41 $M_{\odot}$ from Section 3.6.2.

One possible explanation for a longer orbital period than the photometric period is that J1519 was spun up by the accretion that it experienced and has not yet synchronized the rotation and orbital periods in the approximate 8 Myr since mass transfer stopped (assuming the mass transfer ceased at the same time the WD formed). Green et al. (2019b) analyzed *Chandra* observations of J1519 (as well as five other Hα emission dCs) and found it to show X-ray emission consistent with having a short rotation period, which would lend support to the accretion spin-up scenario. Deeper photometric imaging and RV follow-up, particularly of the WD component, could even better characterize this system. It is clear, however, that this dC has both photometric and RV variability on a <0.33-d timescale, indicating it most likely has a short orbital period and formed through a CE event.

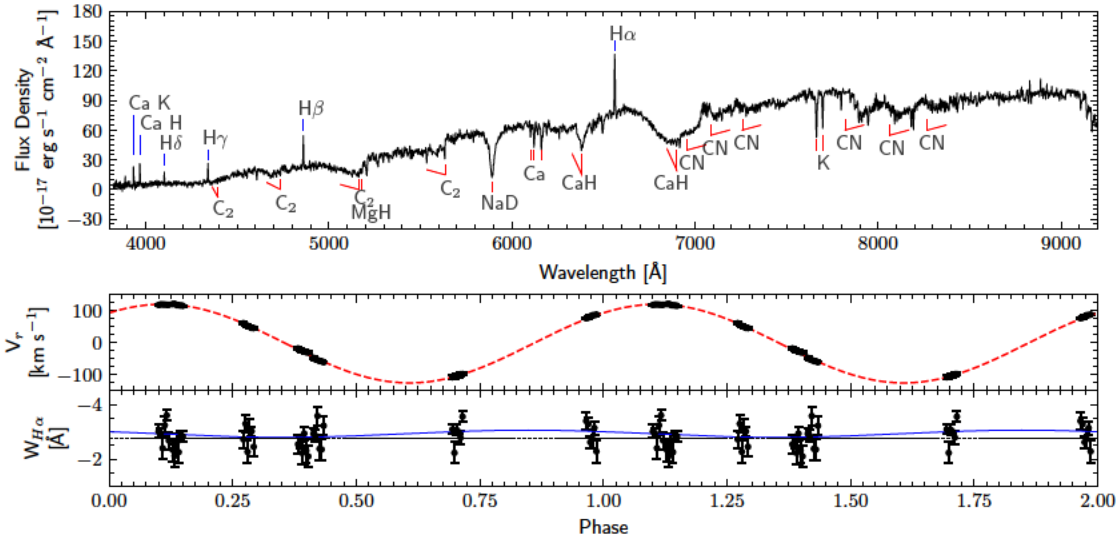

Figure 3.3: TOP: SDSS spectrum for the dC SDSS J123045.53+410943.8. The typical carbon bands of C_2 and CN for late-type dCs are labeled. Additionally, clear and strong emissions of Hα, Hβ, Hγ, Hδ, and Ca H and K are visible. Middle: RV as measured from the Hα and *K I* lines for SDSS J123045.53+410943.8, folded at the photometric period of 0.882519 d. The red dashed line represents the best fitting model. Bottom: Equivalent widths measured from the Hα line, phased on the photometric period. The blue curve is the best fit single sinusoid model to the data, while the grey dotted line is the average equivalent width value. The y-axis has been inverted so that smaller equivalent width values (more emission) are up. I do not detect any significant variation in phase for the equivalent width, to a limit of $<$1.50 Å.

3.5.3 SDSS J123045.53+410943.8

Another interesting dC is SDSS J123045.53+410943.8 (J1230), whose SDSS spectrum is shown in Figure 3.3. J1230 shows the C_2 and CN lines typical of late-type dC stars, but also shows strong absorption lines of K and a strong CaH band near 6800 Å. Additionally, this dC shows strong emission lines of Hα, Hβ, Hγ, Hδ, and Ca H and K. Unlike J1519, there is no visible WD component in the spectrum of J1230.

I observed J1230 (r = 16.6 mag) with the Binospec spectrograph on the 6.5m MMT using the setup described in Section 3.5.1. I took 6×266 s spectra on the

nights of 2021 February 3, 5, 7, 8, 9, 11 and 15. This resulted in a total of 42 spectra, with an average S/N of 13 in the continuum region near Hα. I measured the line center and equivalent widths of the Hα line, as well as for the two K lines visible in the MMT spectra of J1230. The emission and absorption lines have the same velocities, indicating they are coming from the same region. I average these velocities to measure the RV for each of the 42 epochs.

In the same method as J1519, I used the `rvfit` program to fit the RV curve of J1230. For this dC, I left all parameters free for fitting, with the resulting best period fit matching that of the photometric light curve ($P = 0.882519 \pm 0.000020\,\mathrm{d}$). I, therefore, fix the period to the photometric period and the eccentricity to 0.0, and refit the RVs. The resulting best fit can be found in Table 3.5.5 and the phased RV curve in Figure 3.3. As with J1519, I find the parameter errors using an MCMC method centered around the best-fit parameters.

The best fit gives a circular orbit with a semi-amplitude of $K_2 = 123.0 \pm 0.7\,\mathrm{km\,s^{-1}}$. If I use the estimated dC mass from Section 3.6.2 ($0.25\,\mathrm{M_\odot}$) and an assumed WD mass of $0.6\,\mathrm{M_\odot}$ the implied inclination of this system is around $i = 56°$.

The presence of multiple emission lines of H and Ca suggest that the photometric variability of J1230 is coming from the re-processing of the WD flux on the surface of the dC. Even though the WD companion to J1230 is not hot enough to be seen in the optical spectrum, it may be warm enough to still heat the surface of the dC. If this is true, it could be expected that the dC is at maximum brightness when the WD-facing side is pointed toward us maximally, i.e. when the dC is moving transversely on the sky, between the ascending and descending nodes. Comparing the light curve of J1230 to the RVs however shows this is not the case, as if it were, it would be expected that the RV to be moving to the descending node after the

photometric maximum, which the RV curve for J1230 is 0.33 out of phase with. This suggests that the photometric variability is not coming from re-processing, but rather from spot rotation on an active dC (with the emission lines indicating chromospheric activity). I do note that the uncertainties on the epoch of maximum brightness and period may cause an incorrect prediction of the phase when the spectroscopy was collected in 2021 February by up to 0.03 cycles.

3.5.4 SBSS 1310+561

I observed SBSS 1310+561 ($r = 14.1$ mag) using the FAST spectrograph on the 1.5m telescope at FLWO using the setup described in Section 3.5.1. I took 3×300 s spectra during the nights of 2021 February 10 and 11, and 6×300 s spectra during the night of 2021 February 12 for a total of 12 spectra with an average S/N of 32 in the continuum region near Hα.

Unlike with the MMT and Magellan observations, because of observing time constraints on the awarded FAST time, I chose to obtain these spectra close to the quadrature phases based on the ZTF photometry ($P = 5.1878 \pm 0.0012$ d). I assumed that the photometric period corresponds to the orbital period, and used t_0 from the light curve to calculate the expected times that SBSS 1310+561 should be at the quadrature phases ($\phi = 0.25$ and $\phi = 0.75$). The actual observations were taken at phases $\phi = 0.27 \pm 0.02$ and $\phi = 0.47 \pm 0.01$.

From these spectra, I measured the RV at $\phi = 0.27$ to be $V_r = -79.7 \pm 9.5$ km s^{-1} and the RV at $\phi = 0.47$ to be $V_r = -19.3 \pm 5.5$ km s^{-1}. Taking the difference in these two velocities for this system ($\Delta RV = 60 \pm 11$ km s^{-1}) can place a lower limit on the semi-amplitude of $K_2 > 30 \pm 6$ km s^{-1}. Using the estimated mass from Section 3.6.2 ($0.46 M_\odot$) and an assumed WD mass of $0.6\,M_\odot$, this constrains the inclination to

$i \geq 25°$ (if $i = 60°$, then it would be expected that $K_2 = 109$ km s^{-1}). Since the phase difference between the two epochs is quite small, this ΔRV suggests that SBSS 1310+561 is in a tight orbit and is very likely a PCEB.

3.5.5 LAMOST J062558.33+023019.4

The dC LAMOST J062558.33+023019.4 (hereafter J0625, $r = 13.9$ mag) was observed on the nights of 2021 January 11 and 12 using the Magellan MagE instrument setup described in Section 3.5.1. Each night, I observed 15×300 s exposures. The final reduced spectra consist of 30 epochs with an average S/N of 22 each in the continuum region near Hα.

Using the Hα emission line, I measured the RV of J0625 for each epoch. I found no evidence for RV variability, nor any variability in Hα equivalent width. I found the RV to vary with only a standard deviation of 3.9 km s^{-1}, and with a maximum $\Delta RV = 12.1 \pm 3.2$ km s^{-1}. In addition, cross-correlation of the spectra across epochs resulted in no significant measured RV variations. Using the estimated mass from Section 3.6.2 (0.84 M$_\odot$) and an assumed WD mass of 0.6 M$_\odot$, this places a constraint on the inclination of $i \leq 7°$ (if $i = 60°$, then it would be expected that $K_2 = 44$ km s^{-1}). This may suggest that the photometric variability is not related to the orbital period in this system since such a low inclination (and low semi-amplitude) is unlikely if the photometric period of 7.6080 ± 0.0014 d represents the orbital period. Hence, this system adds weight to the evidence that the photometric variability in dCs may often be due to spot rotation.

Table 3.4: Fit parameters from the radial velocity follow-up. The value for each parameter is given as the median of the marginalized distribution of the MCMC samples. The errors for each parameter are the 1σ values from the marginalized distribution of the MCMC samples. Additionally, derived values for the orbital separation ($a \sin i$) and mass function ($f(m_1, m_2)$) are given.

Parameter	J1519	J1230
P [d]	0.327526 ± 0.000012	0.882519^a
T_p [MJD]	59080.2085 ± 0.0053	59265.07955 ± 0.00059
e	0.0^a	0.0^a
ω [deg]	90.0^a	90.0^a
γ [km s^{-1}]	-1.7 ± 2.3	-2.9 ± 0.5
K_2 [km s^{-1}]	33.3 ± 1.4	123.0 ± 0.7
$a_2 \sin i$ [$R_\odot$]	0.2153 ± 0.0090	2.15 ± 0.01
$f(m_1, m_2)$ [$M_\odot$]	0.00125 ± 0.00016	0.170 ± 0.003
χ^2_ν	2.6	0.97
N_{obs}	39	42
Time span [d]	247.2	12.15
rms_2 [km s^{-1}]	11.6	2.5

[a] — Parameter fixed during fitting.

3.6 Common Envelope Connection

For the progenitor of the dC companion to become a C giant, it must enter the third-dredge-up phase (Iben, 1974). AGB stars have a degenerate CO core with a double-shell (moving outward from the core) of helium and hydrogen. As the hydrogen shell (which produces most of the energy) continues to fuse H into He, the helium shell surrounding the core continues to grow. Eventually, the helium shell experiences runaway fusion, driving the expansion of the envelope material above. This He-shell "flash" and expansion means the star is now in the TP-AGB phase. Helium shell fusion causes the inter-shell region to become strongly convective, dredging helium fusion products to the surface, i.e., the third dredge-up. As the expansion continues, the pressure in the helium shell will drop, eventually stopping its energy production. The layers contract again with hydrogen shell fusion resuming, and the cycle repeats.

Each successive thermal pulse becomes stronger, reaching deeper into the intershell zone, and the stellar radius increases (Iben & Renzini, 1983). As helium shell fusion products are brought to the surface, it is possible that the envelope carbon abundance increases until C/O > 1. Since C preferentially binds with O, C_2 and CN bands only appear when C/O> 1, forming a C giant star.

AGB stars going through the TP-AGB phase can reach radii of $800\,R_\odot$ (3.7 au) as they experience successively stronger thermal pulses (Marigo et al., 2017). Assuming an AGB mass of $2.5\,M_\odot$, AGB radius of $800\,R_\odot$, and a dC mass of $0.4\,M_\odot$, this system would experience the beginning of a CE phase with an initial period of ≈ 4.2 yr (if the dC mass is $1.0\,M_\odot$ instead, then P≈ 3.8 yr). Therefore, dCs with initial periods ≈ 4 yr (1500 d) or less will very likely have experienced a CE phase, corresponding to the shorter-period peak modeled by de Kool & Green (1995). The dCs in this chapter with P< 1 d are most certainly the result of a CE spiral-in. Of the six dC periods in the current literature, two of them have P< 3 d, so have likely experienced a CE. It seems then that many dCs may have experienced a CE phase.

Dell'Agli et al. (2021) recently studied the extreme AGB stars (those AGB stars which have extremely red mid-IR colors, e.g. Gruendl et al. 2008) and showed that the excess dust and outflow densities of these stars may be explained by envelope stripping in a CE event. Their models suggest that these extreme AGB stars are actually PCEBs with orbital periods of order 1 d, matching the periods for dCs in this sample. Dell'Agli et al. (2021) also found that the CE in their models starts after the rapid growth of the AGB radius, once the C/O ratio increases past unity, which corresponds well with the requirements for producing the short-period dCs found here. This makes these extreme AGB stars potential progenitors systems of the dCs that are in the CE phase currently.

However, is mass accretion during a CE phase the most likely mass transfer mechanism to form dCs? I address this question by looking at the periodic dC sample in the context of models that simulate expected binary populations.

3.6.1 Binary Population Synthesis Models

I used the binary population synthesis (BPS) models of Toonen & Nelemans (2013) to see if the observed population of dCs can be reproduced by theory. The full details of the BPS models can be found in Toonen & Nelemans (2013) and are briefly described here.

These BPS models were created using the SeBa (Portegies Zwart & Verbunt, 1996; Nelemans et al., 2001; Toonen et al., 2012; Toonen & Nelemans, 2013) population synthesis code. This code generates an initial population of binaries and simulates their evolution, taking into account processes such as stellar winds, magnetic braking, mass transfer, common-envelope, and angular momentum loss. The initial stellar population is generated from the classical BPS distributions found in Toonen & Nelemans (2013) via a Monte Carlo method. The resulting binaries are then convolved with a Galactic model including a star formation history that depends on time and location in the Milky Way based on Boissier & Prantzos (1999) so that the simulated binaries can be compared to the observed dC sample.

For the synthetic populations used here, the CE phase is modeled on the basis of the energy budget i.e. the classical α-formalism of Tutukov & Yungelson (1979). I discuss the results of two different models here that account for two different CE efficiencies: model $\alpha\alpha$ and $\alpha\alpha 2$ which have $\alpha\lambda$ of 2 and 0.25, respectively. The parameter λ is the structure parameter of the envelope to calculate the envelope binding energy (Paczynski, 1976; Webbink, 1984; de Kool et al., 1987; Livio & Soker,

1988; de Kool, 1990; Xu & Li, 2010). The α parameter describes the efficiency with which orbital energy is consumed to unbind the CE. A smaller value of α implies less efficient usage of orbital energy, and therefore a stronger shrinkage of the orbital period during the CE-phase. I do not consider the orbital angular momentum method of Nelemans et al. (2000), as this model does not reproduce the observed characteristics of the general PCEB (WD/main sequence) population (Toonen & Nelemans, 2013).

Furthermore, the BPS models here allow for accretion during the CE phase. The accretion rate is limited by the thermal timescale of the accretor times a factor that is dependent on the stellar radius and the corresponding Roche lobe (Portegies Zwart & Verbunt, 1996; Toonen et al., 2012) following Kippenhahn & Meyer-Hofmeister (1977); Neo et al. (1977); Packet & De Greve (1979); Pols & Marinus (1994). The total accreted mass is then given by the integral of the accretion rate times the timescale of the CE event, which here is taken to be 100 yr. This timescale is consistent with hydrodynamical simulations (Ricker & Taam, 2008; Ivanova et al., 2013) and observations of hot subdwarf binaries (Igoshev et al., 2020), although cataclysmic variables may suggest a longer CE timescale, up to 10^4 yr (Michaely & Perets, 2019; Igoshev et al., 2020).

3.6.2 BPS Comparison to Observed dC Sample

I use the resulting model population for a direct comparison to the observed sample of short-period dCs, assuming the photometric period is the current orbital period. To do this, I estimated dC masses based on their infrared absolute magnitude M_K in the K band. Comparisons of M dwarf spectra (Ivanov et al., 2004) to C star spectra (Tanaka et al., 2007) reveal them to be much more similar in the infrared than in the optical region. I used K_s band (2.159 μm) magnitudes from the Two Micron All-Sky

Survey (2MASS; Skrutskie et al., 2006). Six of the periodic dCs do not have K_s band magnitudes. For these, I first fit *Gaia* absolute G band (M_G) to the dCs that do have K_s band magnitudes. This fit was then used to convert the *Gaia* M_G into M_{K_s} for the dCs lacking K_s band magnitudes. I then fit M_{K_s} for the dCs to stellar masses using data from Kraus & Hillenbrand (2007). This fitting also provides bolometric luminosities for the dCs in the sample. Comparing these bolometric luminosities to those provided in Green et al. (2019b) (who used a spectral energy distribution method fitting $0.35 - 12.5\,\mu$m) for the four dCs that overlap, I find my luminosities agree within 3%, indicating the dC mass estimates should be reliable.

The mass estimates can be found in Table 3.6.2. I find that none of the dCs are fit with masses $> 1\,M_\odot$ or $< 0.2\,M_\odot$, in agreement with the range for which detectable C_2, CN, and CH bands are expected. I note that some of the lowest mass dCs may have been brown dwarfs or even planets before they accreted significant C-enriched material from their former AGB companion.

Using the mass-radius relationship for main-sequence stars of Eker et al. (2018), I estimate the radius for these periodic dCs as well, which are included in Table 3.6.2. Using these estimated radii I calculated the Roche-lobe filling factor (RLFF), using the equation of Eggleton (1983) to find the Roche radii. Six out of 34 of the periodic dCs may be experiencing RLOF back onto the WD (all have an RLFF > 1 in Table 3.6.2). However, I caution that these physical parameters are derived from O-rich main-sequence models, which may not accurately represent all dCs. For example, (1) the mass of the unseen WD companion is unknown and assumed to be $0.6\,M_\odot$ (2) I assume these mass-radius and M_K-mass relations hold for dCs, as they do for normal O-rich stars (3) dCs are thought to be of a lower metallicity population and studies have found that low metallicity M dwarfs may have smaller radii (Kesseli et al., 2019)

and (4) since dCs may have increased activity and magnetic fields due to their mass accretion, their radii may be inflated (Kesseli et al., 2018). I see no obvious evidence of flickering or accretion outbursts in any of the ZTF light curves that might indicate current RLOF back onto the WD.

Table 3.5: Distances and magnitudes for the periodic dCs. I use the *Gaia* distances, colors, and magnitudes, as well as the 2MASS absolute K magnitudes to estimate masses and bolometric luminosities for our dCs. For the solar bolometric luminosity, I adopt the value $\log_{10} L_{\odot} = 33.58$. I also calculate the Roche-lobe filling factor (RLFF) under the assumption of a $0.6\,M_{\odot}$ WD companion. I calculate the mass errors to be of order $0.05\,M_{\odot}$, the $\log_{10}(L_{\rm bol}/L_{\odot})$ errors to be of order 0.1, and the radius errors to be of order $0.05\,R_{\odot}$. However, I caution that physical parameters are derived from O-rich main-sequence models, which may not accurately represent all dCs.

R.A. (J2016.0)	Decl. (J2016.0)	ϖ^a	σ^a_{ϖ}	d^b	$\sigma^b_{\rm d}$	BP - RP^a	M^a_G	M_K	M_{dC}	$\log_{10}(L_{\rm bol}/L_{\odot})$	R_{dC}	RLFF
		[mas]	[mas]	[pc]	[pc]	[mag]	[mag]	[mag]	[$M_{\odot}$]	[erg s^{-1}]	[$R_{\odot}$]	
00h47m06.76s	+00d07m48.80s	0.68	0.18	1340	196	1.78	7.85	4.79	0.67	-0.88	0.59	0.06
01h31m19.05s	+37d20m25.30s	1.12	0.12	944	88	1.59	7.63	4.79	0.67	-0.88	0.59	0.27
02h35m30.65s	+02d25m18.58s	1.678	0.085	590	30	1.61	7.93	5.08	0.60	-1.05	0.52	0.22
02h54m14.24s	+26d21m54.19s	3.294	0.082	301	8	1.46	7.25	4.52	0.74	-0.72	0.67	1.10
04h16m05.11s	+50d28m28.52s	2.946	0.015	335	2	1.19	6.04	4.00	0.87	-0.40	0.83	0.12
05h02m40.82s	+40d23m23.59s	1.237	0.086	840	62	1.61	7.58	4.65	0.71	-0.79	0.63	0.13
06h25m58.34s	+02d30m19.43s	2.410	0.024	409	4	1.09	5.93	3.90	0.90	-0.34	0.86	0.11
07h44m47.66s	+51d38m31.76s	2.178	0.050	457	11	1.64	7.92	5.09	0.60	-1.05	0.52	0.23
08h11m57.14s	+14d35m33.00s	1.596	0.039	612	14	0.69	6.72	4.39	0.77	-0.64	0.70	0.45
09h14m58.08s	+21d56m39.65s	3.594	0.050	275	4	1.82	8.43	5.23	0.56	-1.14	0.49	0.25
09h33m24.58s	-00d31m44.07s	5.726	0.036	173	1	1.63	7.91	5.14	0.59	-1.08	0.51	0.27
09h40m26.28s	+36d25m48.81s	1.55	0.21	765	92	1.77	8.93	5.61	0.48	-1.35	0.41	0.17
12h02m46.01s	+54d19m29.24s	1.08	0.19	1103	170	1.98	8.87	5.32	0.55	-1.18	0.47	0.26
12h08m53.35s	-00d08m47.99s	0.78	0.37	2403	372	1.35	6.95	4.65^c	0.71	-0.80	0.63	0.70
12h10m06.99s	+58d43m18.34s	1.134	0.064	873	44	1.41	7.46	4.79	0.67	-0.88	0.59	1.04
12h23m57.62s	+55d01m51.43s	1.911	0.079	521	21	1.79	9.03	5.86	0.43	-1.48	0.36	0.50
12h30m45.52s	+41d09m43.45s	5.736	0.056	173	1	2.14	10.38	6.82	0.25	-1.96	0.22	0.20
13h03m59.18s	+05d09m38.62s	1.44	0.10	722	58	1.53	7.96	5.16	0.58	-1.10	0.50	0.20
13h12m42.27s	+55d55m54.84s	9.54	0.023	106	0	1.91	9.10	5.71	0.46	-1.40	0.39	0.08
13h31m23.61s	+48d26m24.37s	1.10	0.15	959	136	1.92	8.92	5.62	0.48	-1.35	0.40	0.75

Table continued on next page

(continued)

R.A. (J2016.0)	Decl. (J2016.0)	ϖ^a [mas]	σ^a_ϖ [mas]	d^b [pc]	σ^b_d [pc]	BP - RP^a [mag]	M^a_G [mag]	M_K [mag]	M_{dC} [$M_\odot$]	$\log_{10}(L_{bol}/L_\odot)$ [erg s^{-1}]	R_{dC} [$R_\odot$]	RLFF
14h09m53.08s	-06d11m41.71s	2.502	0.079	393	11	1.32	6.45	4.11	0.84	-0.47	0.79	0.87
14h15m15.24s	+51d41m28.01s	0.77	0.36	4420	799	1.19	6.62	4.47[c]	0.75	-0.69	0.68	0.87
15h11m44.58s	+38d59m10.46s	2.05	0.11	487	29	1.84	8.90	5.88	0.42	-1.49	0.35	0.50
15h15m42.72s	+52d01m45.47s	1.291	0.065	775	37	1.61	8.00	5.30	0.55	-1.18	0.47	0.60
15h19m05.93s	+50d07m03.14s	2.274	0.064	437	14	0.77	9.08	5.95	0.41	-1.53	0.34	0.52
15h24m34.12s	+44d49m55.84s	0.96	0.19	1236	211	2.00	8.89	5.80[c]	0.44	-1.45	0.37	0.62
15h25m04.49s	+32d25m10.90s	0.10	0.40	3280	598	1.55	7.42	4.91[c]	0.64	-0.95	0.56	1.22
15h30m59.26s	+45d12m00.33s	2.215	0.044	444	8	1.81	8.45	5.39	0.53	-1.22	0.45	0.05
15h35m32.92s	+01d10m16.22s	1.18	0.39	1179	234	2.15	9.09	4.80	0.67	-0.88	0.59	1.07
16h37m18.63s	+27d40m26.63s	2.497	0.077	397	12	2.12	9.54	5.92	0.41	-1.51	0.35	0.21
16h59m02.30s	+25d05m49.00s	0.88	0.24	1293	220	2.07	8.87	5.79[c]	0.44	-1.44	0.37	0.57
19h23m55.93s	+44d58m32.20s	1.238	0.048	802	28	1.36	6.90	4.79	0.67	-0.88	0.59	1.21
22h08m10.01s	+25d17m30.17s	4.121	0.053	241	3	1.56	7.75	4.79	0.67	-0.88	0.59	0.60
23h41m30.74s	+15d19m43.20s	0.27	0.12	2685	482	1.04	5.67	3.99	0.87	-0.40	0.83	1.60

[a] — From Gaia Collaboration et al. (2021), b - From Bailer-Jones et al. (2021), c- M_K interpolated from M_G

[b] — From Bailer-Jones et al. (2021)

[c] — M_K interpolated from M_G

To compare the BPS models directly to the observed dC sample, I applied a series of cuts and selection effects to the models, as follows: (1) P $<$ 100 d (2) r mag $<$ 19.5 (3) $M_{dC} \leq 1\,M_{\odot}$ (4) 1.0 $<M_{ZAMS} < 4\,M_{\odot}$ (5) the initial primary must be a TP-AGB star at the onset of the CE phase. Here, M_{dC} is the current mass of the main sequence companion in the BPS models, and M_{ZAMS} is the initial mass of the primary at the beginning of the models (which will become the AGB donor).

I show the resulting BPS models in Figure 3.4 and Figure 3.5 — models $\alpha\alpha 2$ and $\alpha\alpha$, respectively. In both figures, the BPS models are shown as the colored 2D histogram in mass and period (note that the histogram color scale is logarithmic and its range is different for each plot), and the periodic dC stars from this chapter are represented as the red scatter points (with KDE contours). The dashed black line represents the RLOF boundary, with systems occupying the region to the left (shaded in grey) filling their Roche lobes, under the assumption of a $0.6\,M_{\odot}$ WD companion. Both figures also show a histogram of the estimated mass accreted during the CE phase (assumed to last 100 yr).

Figure 3.4 shows model $\alpha\alpha 2$ ($\alpha\lambda = 0.25$) and includes three different magnetic braking prescriptions. Panel (a) uses the magnetic braking of Rappaport et al. (1983), panel (b) that of Ivanova & Taam (2003) and panel (c) that of Knigge et al. (2011). Again, the color scale is logarithmic and its range is different for each sub-figure.

Model $\alpha\alpha 2$, however, does not reproduce the mass distribution of the dCs very well, generating lower mass systems than observed (still under the assumption that the physical parameters derived from O-rich main-sequence models apply to dCs). While it may be that model $\alpha\alpha 2$ does not produce low mass dCs, I have not considered the sample selection effects in this comparison. THe observed sample is likely biased toward lower mass dCs as (1) they have stronger C_2 and CN bands, and (2) their

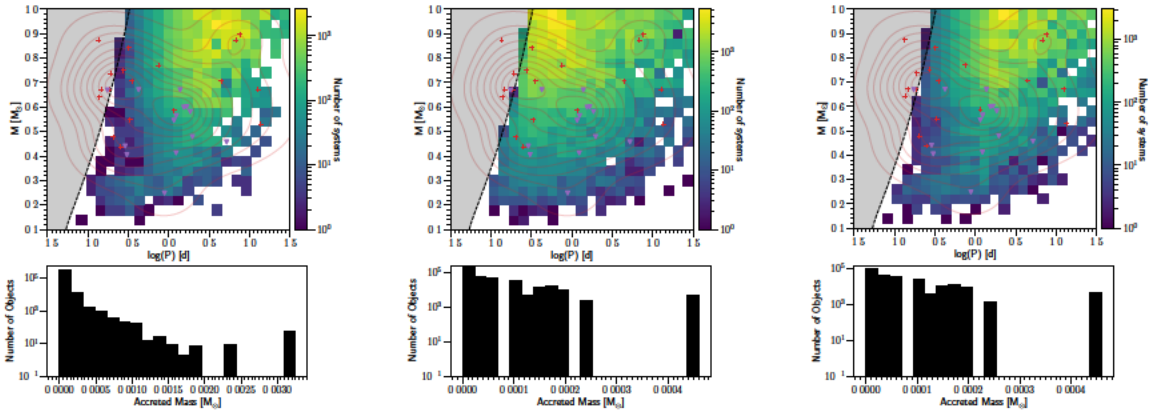

(a) **(b)** **(c)**

Figure 3.4: Binary population syntheses results for model $\alpha\alpha 2$, which is the model with lower common-envelope efficiency ($\alpha\lambda = 0.25$) in which less orbital energy goes to unbinding the CE. The background heat map shows the number of systems (colored on a log scale) in model $\alpha\alpha 2$ going through a CE phase while the primary is in the TP-AGB phase. The plotted masses are for the secondary (i.e. the dC) and periods are for the currently observed system. Each panel uses a different magnetic braking formalism: (a) magnetic braking from Rappaport et al. (1983) (b) magnetic braking from Ivanova & Taam (2003) (c) magnetic braking from Knigge et al. (2011). The red plus scatter markers are the observed short period dC sample without Hα emission, while the purple triangles are dCs which show Hα emission. The red contours are a KDE contour for the entire periodic dC sample. The dashed black curve represents the boundary for current dC systems to be experiencing RLOF, where systems to the left in the grey shaded region may be experiencing RLOF. The bottom panel shows a histogram of the estimated mass accreted by the secondary during the CE phase. While this model ($\alpha\alpha 2$) reproduces the period distribution better than model $\alpha\alpha$ (see Figure 3.5), the estimated accreted mass is even lower than that of $\alpha\alpha$ because of the lower CE efficiency. Since $>0.03\,M_\odot$ of mass transfer is likely required to create a dC, a CE is not likely to be the primary mechanism for accretion to form a dC.

variability is fractionally larger and so easier to detect.

Model $\alpha\alpha$ (Figure 3.5) uses a higher CE efficiency ($\alpha\lambda = 2$) similar to classical BPS studies and includes the standard magnetic braking of Rappaport et al. (1983). From Figure 3.5, it is seen that this model is unable to reproduce the short periods of this observed dC sample. This is in agreement with the conclusions based on the SDSS PCEBs (WD+MS systems; Zorotovic et al. 2010; Toonen & Nelemans 2013; Camacho et al. 2014), where Toonen & Nelemans (2013) found that standard efficiency ($\alpha\lambda = 2$) CE was also unable to reproduce the observed periods, as it generated too many long-period PCEBs.

A crucial shortfall is that the estimated mass accreted for all models is too small to convert a main-sequence star into a dC (see Section 3.7 for a discussion). Miszalski et al. (2013) suggest that to shift the secondary envelope from approximately solar $(\mathrm{C/O})_i \sim 1/3$ to the observed $(\mathrm{C/O})_f > 1$ requires $\Delta M_2 = 0.03$–$0.35\,M_\odot$ for $M_2 = 1.0$–$0.4\,M_\odot$. The predicted mass accretion in the BPS models is lower than this by 2−3 orders of magnitude. Together with the strong mismatch between the modeled and observed dC period-mass distributions, it seems clear that there must be further mass accretion outside the brief CE phase.

A solution to the under-prediction of accreted mass may be that more mass accretion may take place before the CE phase, but during the TP-AGB phase, by wind accretion during wind-RLOF (Mohamed & Podsiadlowski, 2007). Wind-RLOF is a mass transfer state that lies between standard wind mass transfer and standard RLOF, where the wind of the primary star is focused toward the secondary star. This results in increased mass transfer efficiency as compared to the standard BHL accretion case (Hoyle & Lyttleton, 1939; Bondi & Hoyle, 1944).

In the wind-RLOF regime, the primary is technically not filling its Roche lobe.

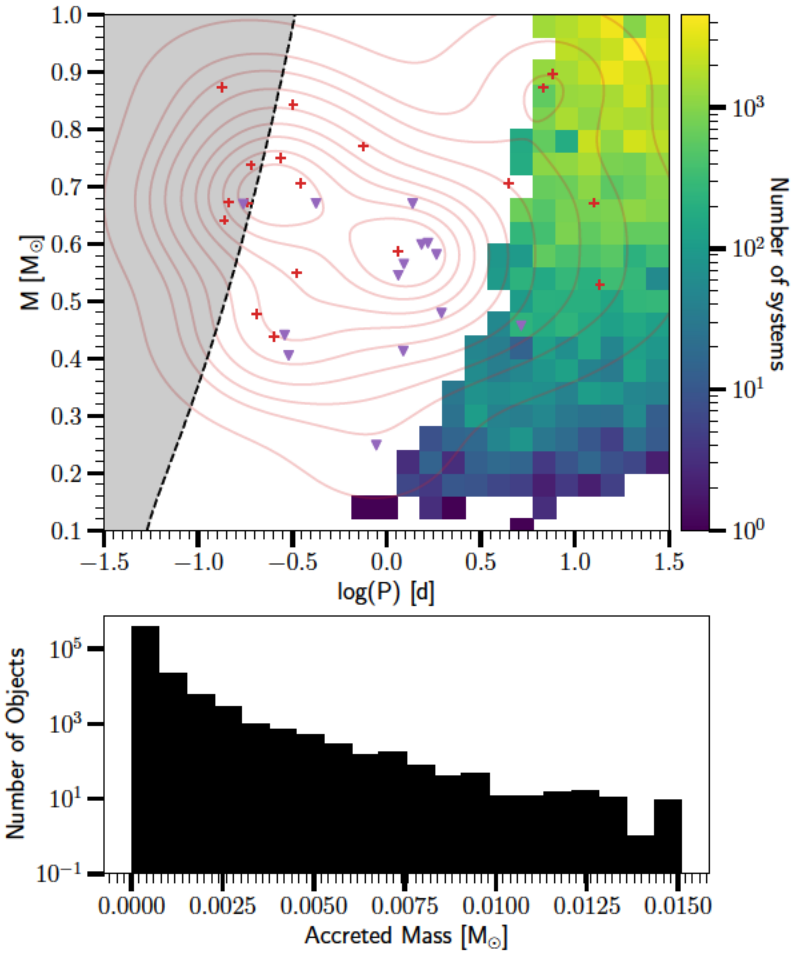

Figure 3.5: Binary population synthesis results for model $\alpha\alpha$, which is the model with higher CE efficiency ($\alpha\lambda = 2$). The background heat map shows the number of systems (colored on a log scale) in model $\alpha\alpha$ going through a common-envelope phase while the primary is on the TP-AGB phase. The plotted masses are for the secondary (i.e. the dC) and periods are for the currently observed system, including standard magnetic braking from Rappaport et al. (1983). The red plus markers are the observed short period dC sample without Hα emission, while the purple triangles are dCs that show Hα emission. The red contours are a KDE contour for the entire observed dC sample. The dashed black curve represents the boundary for current dC systems to be experiencing RLOF, where systems to the left in the grey shaded region may be experiencing RLOF. The bottom panel shows a histogram of the estimated mass accreted onto the secondary during the CE phase. This model ($\alpha\alpha$) does not reproduce the observed dC period distribution, as it does not produce periods below 1d, as well as not being able to accrete enough expected mass ($>0.03\,M_\odot$ necessary to form dCs.

However, low-velocity wind matter is funneled through the Roche lobe to the companion, allowing for mass transfer to take place in binaries with wider orbits than the classical RLOF case. Wind-RLOF would boost dC formation since, if the initial orbital separation is too small, the expanding AGB atmosphere can cause a CE before the third dredge-up can turn the AGB into a C star.

A variety of simulations (Abate et al., 2013; Saladino et al., 2018, 2019; Saladino & Pols, 2019) have shown that wind-RLOF in binaries with AGB primaries can have mass-transfer efficiencies of 40-50%. For an average AGB wind mass-loss rate of 10^{-7}–10^{-4} $M_{\odot}yr^{-1}$ (Höfner, 2015), a main sequence companion could accrete enough material ($\sim 0.35M_{\odot}$) in only 10^{3}–10^{6} yr, within the time an AGB star is expected to stay a C star (10^{6}yr; Marigo et al., 2017). Wind-RLOF has also been shown to efficiently tighten the orbit (Saladino et al., 2018; Chen et al., 2018) so that more systems could be driven towards orbits with the short periods found for these dCs.

Indeed, it appears that wind-RLOF may be the dominant mass transfer mechanism for many chemically peculiar stars. Abate et al. (2013) showed that simulations of AGB binaries with wind-RLOF were better able to reproduce the observed formation rates of the CEMP-s stars. Saladino et al. (2019) and Saladino & Pols (2019) also performed simulations finding AGB binaries with wind-RLOF were consistent with the observed properties of the CEMP-s, CH, and Ba stars. This further strengthens the connection between dCs, wind-RLOF, and the other chemically peculiar stars.

However, detailed modeling of the wind-RLOF in the specific case of the TP-AGB phase with a C star is needed to understand how the larger stellar radii of AGB-C stars and the increased dust formation often found in their winds affect the wind-RLOF mass transfer efficiencies. The periodic dCs in this chapter represent a prime sample that is ready for spectroscopic follow-up and for comparison to future models

of wind-RLOF mass transfer.

3.7 Summary

I searched ZTF light curves of a sample of 944 dCs for periodic signals. I have found 34 dCs with signs of significant photometric variability, with 82% having P$<$ 2 d. The most likely origins of this periodicity is either from spot rotation or surface heating of the dC from the close WD companion. Even if the detected ZTF periods arise from ellipsoidal variations and represent half the orbital period, such short periods are surprising for dC stars, which require significant accretion from a TP-AGB C giant to turn them into the C-enriched dwarfs seen today.

Spectroscopic follow-up is needed to determine the source of the variability in each of these periodic dCs. This is especially important to confirm, for the case of spot rotation, that the system is circularized and tidally locked so that the rotation period can be assumed to equal the orbital period (i.e. that the reported photometric periods correspond to both rotational and orbital periods). The periodic dCs in this chapter provide a rich new sample to target for spectroscopic follow-up, as well as to study dC formation and properties. I have confirmed the photometric period as the orbital period for one dC for which I have obtained spectroscopic follow-up. In two other dCs I have confirmed that they must have short orbital periods from their RVs (not confirming the photometric period as the orbital period, however). In all three cases, these short (P$<$ 1 d) orbits indicate these dCs have indeed experienced a CE phase.

These short periods indicate that at least some dCs will experience a CE at some point in their formation, with P$<$ 1 d dCs having experienced experiencing substantial plunge-in. I used binary population synthesis models to show that the observed

sample of dCs is not well-reconstructed by mass transfer during the common-envelope phase alone, since the dCs in this sample require at least $0.03\,M_\odot$ of mass accretion but the models predict 2–3 orders of magnitude less transfer during the CE phase, suggesting mass accretion before the CE phase. However, some systems such as cataclysmic variables indicate CE timescales an order or two longer (Michaely & Perets, 2019; Igoshev et al., 2020) than the assumed 100 yr (based on Ricker & Taam, 2008; Igoshev et al., 2020), which may substantially increase the amount of accreted material to the point that the CE alone could provide enough mass to form a dC.

Hydrodynamical simulations of CE evolution typically find that accretion onto a non-degenerate companion is not common, because of the entropy barrier between the companion and the surrounding material (e.g. Ivanova et al., 2013, for a review). In fact, even in the case of neutron star companions, which can accrete more efficiently due to neutrino cooling, accretion is limited to $\lesssim 0.1 M_\odot$ (MacLeod & Ramirez-Ruiz, 2015). Further modeling of the CE phase involving C-AGBs may provide further insight.

dC systems that begin as very wide binaries would experience stable mass transfer and a widening of the orbit. Systems that initially are close would begin a CE phase either during the red giant branch or during the AGB before the TP-AGB and, without experiencing the third dredge-up during the TP-AGB, would not produce dCs. Therefore, it seems that the most likely mass transfer mechanism to form dCs is wind-RLOF.

Further modeling of wind-RLOF in binaries with a TP-AGB star is needed to fully test this formation pathway of dCs. Additionally, further work is needed to understand the relationship between initial dC metallicity and mass to constrain the amount (and composition) of material that needs to be accreted to form a dC. This

would be an important step in constraining the mass-transfer efficiency in the wind-RLOF case.

3.8 Summary

In this chapter, I searched the ZTF survey to find a sample of 34 new periodic dCs. Remarkably, 82% of these have periods $< 2\,\mathrm{d}$, implicating them as PCEBs. I conducted follow-up spectroscopic observations for four dCs, finding all with RV variations consistent with short-period orbits, and two with the same photometric period as their orbital periods. I used binary population synthesis models to compare the dCs to the more normal ($\mathrm{C/O} < 1$) PCEB sample. From the analyses in this chapter, I was able to determine the following:

1. I found 34 new dC periods, with 28 of those having $\mathrm{P} < 2\,\mathrm{d}$, marking them as PCEBs.

2. Finding two dCs with the same period via spectroscopic follow-up suggests that the photometric signal is coming from spot rotation on the dC, with the dC-WD system being tidally locked due to the close orbit, and not from ellipsoidal variations.

3. Comparing these new short period dCs to binary population synthesis models suggests dCs follow the same low common-envelope efficiency as found in the normal ($\mathrm{C/O} < 1$) PCEBs.

4. The amount of mass accreted during the common-envelope phase in too small by more than two orders of magnitude to account for the carbon enrichment of dCs, suggesting that dCs form *prior* to the common-envelope via either wind-Roche lobe overflow or standard Roche lobe overflow.

Chapter 4

X-ray Properties of the Nearest Dwarf Carbon Stars

In this chapter, I examine the X-ray emission of an unbiased sample of dCs using *Chandra*. As products of (likely significant) mass transfer, dCs should show signs of spin-up, for which I tested with *Chandra* observations. For the dCs with detected X-ray emission, I model that emission, finding results consistent with other rapidly rotating stars. I also discuss one dC with an unusual X-ray spectrum and model fits, pointing to more evidence of dCs being post-common-envelope binaries. The contents of this chapter have been published in Roulston et al. (2022).

4.1 Motivation

Main-sequence stars are known to "spin down" as their rotation rates, dynamo strengths, and associated activity decrease with age (e.g., Kraft 1967; Skumanich 1972). As dCs are thought to be from older thick disk and halo populations (Green, 2013; Farihi et al., 2018), they may be expected to exhibit slower rotation rates and corresponding weaker activity. To demonstrate dCs' likely population and hence age, I show a Toomre diagram (Carney et al., 1988) for a sample of dCs in Figure 4.1. I used the Green (2013) SDSS sample of C stars, matching to *Gaia* EDR3 (Gaia Collaboration et al., 2021). I selected only those stars with: (1) parallax $\varpi/\varpi_{\rm err} > 5$ (2) proper

motion signal-to-noise > 5 in both right ascension and declination and (3) absolute $M_G > 5$. I measured the dC RVs from the Hα line and then used the *Gaia* EDR3 distance and proper motions to calculate the space velocities U, V, W. I mark the transitions between thin and thick disks, and thick disk and halo kinematics. As seen in the figure, the majority of dCs show kinematics consistent with either thick disk or halo populations.

However, dCs' activity may not correlate simply with age because they are not single stars and therefore do not evolve independently. Indeed, dCs constitute a population of binary systems in which interaction and mass transfer can be confirmed by simple inspection of their signature optical spectra.

Jeffries & Stevens (1996) showed that a slow (10–20 $\mathrm{km\,s^{-1}}$) AGB wind can spin up a low-mass companion to short ($\lesssim 10$ hr) rotation periods. If dC stars gain most of their carbon-rich mass through wind-RLOF (Mohamed & Podsiadlowski, 2007), which focuses the wind into the orbital plane, it is possible that this may cause dCs to spin up to even shorter periods. Rapid rotation in stars with convective envelopes drives a magnetic dynamo, so this spin-up rejuvenation may result in enhanced chromospheric and coronal activity (e.g., Kosovichev 2013), which normally yields observable Hα and/or X-ray emission. Since M dwarfs show activity lifetimes of $\sim$ 1–5 Gyr (West et al., 2008), dCs may remain active after mass transfer for similar timescales. Additionally, Matrozis et al. (2017) modeled the maximum amount of mass the progenitors of the better studied Ba, and CEMP-s stars can accrete before reaching critical rotation. They found that in order for these stars, and by similarity dCs, to accrete enough material to change their surface abundances there must be angular momentum loss from the freshly spun-up accretor. They suggest one possible method of angular momentum loss is through enhanced magnetic braking from the

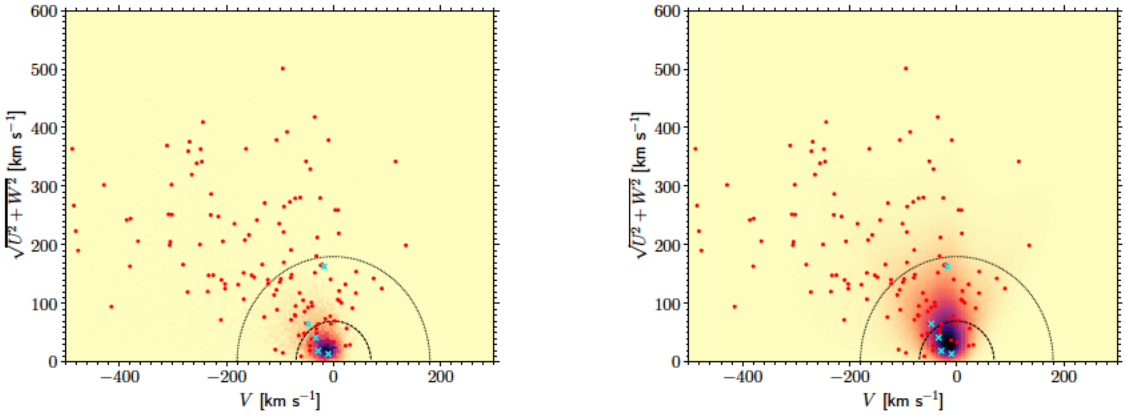

(a) **(b)**

Figure 4.1: Toomre diagram for dCs showing the UVW kinematics with the dCs shown as red scatter points (the cyan points are dCs with detected periodicity from Roulston et al. 2021). The RVs for each dC was measured from the Hα line from their publicly available spectra, either LAMOST or SDSS. Distances and proper motions were taken from *Gaia* EDR3. The marked dashed and dotted lines represent, respectively, the divisions between thin and thick disks, and thick disk and halo kinematics ($V_{tot.} = 70$, 180 km s^{-1}; Bensby et al., 2005; Reddy et al., 2006; Nissen & Schuster, 2009). A sample of SDSS K and M dwarfs is shown as the background heatmap, with darker colors showing regions with a higher density of K and M dwarfs. These normal (C/O < 1) stars are more representative of the thin and thick disk. As dCs must be in binaries, and some are known to be short-period binaries, their RVs may be inflated by their orbital motions. I, therefore also inflate the K and M dwarf UVW space velocities with similar velocities using the RV models of Roulston et al. (2019). The left panel (a) shows the uninflated UVW space velocities for the K and M dwarfs, while the right panel (b) shows the inflated UVW velocities. Even when the K and M dwarfs are inflated with larger velocities to match the dCs, they do not match the same UVW kinematics as the dCs, pointing to dCs truly originating from thick disk or halo populations.

increased differential rotation of the accretor envelope.

Green et al. (2019b) thus aimed to study the activity and rejuvenation of dCs using *Chandra*. Their sample was constructed to observe the dCs that were most likely to be detected based on optical spectroscopy, i.e., those with either Hα emission or showing a composite dC+WD spectrum. They detected all six members of their observed sample; however, their sources lacked enough counts to robustly fit a model to the source spectrum. Nonetheless, they fit two models appropriate for coronally active stars, with differing plasma temperatures of 2 MK and 10 MK. Green et al. (2019b) found that when assuming the lower 2 MK plasma temperature, dCs populate the saturated regime where $\log(L_x/L_{\rm bol}) \sim -3.3$ (e.g., Wright et al., 2011), indicating short rotation periods. However, with the higher 10MK plasma temperatures, only half of the dCs remain in the saturated regime, with periods weakly constrained to < 20 d. While there were no rotation periods available in Green et al. (2019b), they argued that their saturated X-ray activity indicated rapid rotation rates that were indicative of dC spin up from mass transfer.

Green et al. (2019b) end their discussion with the caveat that their sample is not representative of dCs in general since they explicitly observed those dCs with optical signs of activity. They argue that observations of a sample of the closest dCs, without requiring signs of activity, is critical to understanding the dC rotation-activity relationship. In this chapter, I detail my analysis of just such a sample of dCs. This sample consists of the five closest known dCs.

4.2 Sample Selection

I compiled the parent sample of dCs from the current literature. The largest contributor (747 dCs, 79%) is the Green (2013) sample of carbon stars from the SDSS

(York et al., 2000). I also selected a smaller number of dCs from Si et al. (2014), who found 96 new dCs using a label propagation algorithm from SDSS DR8, and Li et al. (2018) who selected carbon stars from the LAMOST survey (Cui et al., 2012) using a machine learning approach. The resulting final parent sample consists of 944 dCs, where I ensured that each is indeed a dC by verifying that each C star had $M_G > 5\,\mathrm{mag}$ from *Gaia* Early Data Release 3 (*Gaia* EDR3; Gaia Collaboration et al., 2021) while having a significant parallax of $\varpi/\varpi_{\mathrm{err}} > 3$. I expect to publish this large parent sample, along with detailed SED fit parameters in an upcoming paper.

I then selected the nearest five dCs to make the final *Chandra*sample. The selected sample can be found in Table 4.2 with their corresponding *Gaia* EDR3 properties. In addition, I have estimated the bolometric luminosities for each selected dC in the same way as in Green et al. (2019b) by using a spectral energy distribution (SED) for each dC and the `sedkit` Python package (Filippazzo et al., 2015). Figure 4.2 shows a color-magnitude diagram for a sample of chemically-enhanced stars, including dCs. From this, it is seen that the five dCs in this sample are all clearly dwarfs having $M_G > 8$. Additionally, I examined the available spectra for the five dCs selected here, all of which show strong C_2 and CN bands.

The reddest stars in this CMD correspond to the lowest mass dCs. These dCs will likely have accreted a substantial fraction (see Miszalski et al. (2013) and the discussion at the end of this chapter) of their current mass and may have even been brown dwarfs before the onset of the accretion that turned them into dCs (see Majidi et al. (2021) for a discussion on a similar topic).

Table 4.1: Selected dCs in this sample. For each, the coordinate positions and parallaxes from *Gaia* EDR3 (Gaia Collaboration et al., 2021) are listed. The distance for each dC is from Bailer-Jones et al. (2021), which were used to calculate the absolute Gaia G band magnitude. Additionally, for each dC, the bolometric luminosity as calculated from the SED fits are included. Here, I have adopted the solar bolometric luminosity of $\log(L_\odot/\mathrm{erg\ s^{-1}}) = 33.583$.

Object		R.A. (J2016.0)	Decl. (J2016.0)	ϖ [mas]	Distance [pc]	M_G [mag]	$\log(L_{\rm bol}/L_\odot)$
LSPM J0435+3401	(J0435)	04h35m26.31s	+34d01m35.54s	7.819 ± 0.019	127.19 ± 0.21	8.18	-1.27 ± 0.01
LAMOST J054640.48+351014.0	(J0546)	05h46m40.51s	+35d10m13.23s	6.126 ± 0.035	162.05 ± 0.62	9.03	-1.54 ± 0.01
HE 1205-0417	(HE1205)	12h07m51.75s	-04d34m41.55s	6.52 ± 0.12	153 ± 2	8.90	-1.43 ± 0.01
LAMOST J124055.15+485114.2	(J1240)	12h40m55.17s	+48d51m14.14s	5.57 ± 0.15	179 ± 3	8.93	-1.55 ± 0.02
SBSS 1310+561	(SBSS1310)	13h12m42.27s	+55d55m54.84s	9.538 ± 0.023	104.48 ± 0.17	9.10	-1.51 ± 0.01

4.3 X-Ray Observations and Analysis

All of the *Chandra* observations were taken with ACIS-S using the S3 chip (backside-illuminated CCD) between 2019 September and 2021 December (*Chandra* proposals 21200072 and 22200008; PI: P. Green). Exposure times, proposed based on optical magnitudes, ranged from 9.83 ks to 36.78 ks, with one dC (LSPM J0435+3401) having multiple exposures (ObsIDs). None of the observations use a grating and all were taken in VFAINT ACIS mode; observation details can be found in Table 4.3.

I reprocessed the *Chandra* event lists for all ObsIDs with the CIAO (ver 4.13.0) `chandra_repro` script and CALDB (4.9.5). This reprocessing ensures I have used the most recent calibrations for the data, including corrections for afterglows, bad pixels, charge transfer inefficiency, and time-dependent gain corrections. I searched each ObsID for each target near the expected *Gaia* EDR3 position, detecting sources for two of the five targets, J0435 and SDSS1310. J0435 was detected in all seven ObsIDs, with all detections being within 1.1″ of the expected *Gaia* EDR3 position. SDSS1310 was detected within 0.3″ of the *Gaia* EDR3 position. A detection was counted if there were multiple neighboring pixels, within 5″of the expected source, that had at least one X-ray count.

I estimated source properties in the 0.3–8.0 keV energy range using the CIAO `srcflux` tool for the two dCs with detections. For both detections, I used a circular aperture of 5″ for the source region and an annular aperture with an inner radius of 5″ and outer radius of 15″ for the background region. Both of these regions were centered on the detected position of the dC. I accounted for Milky Way dust extinction by using the 3-dimensional Bayestar17 (Green et al., 2018) dust maps from the `dustmaps` Python package (Green, 2018); resulting line of sight column density (N_H) values are listed in Table 4.3.

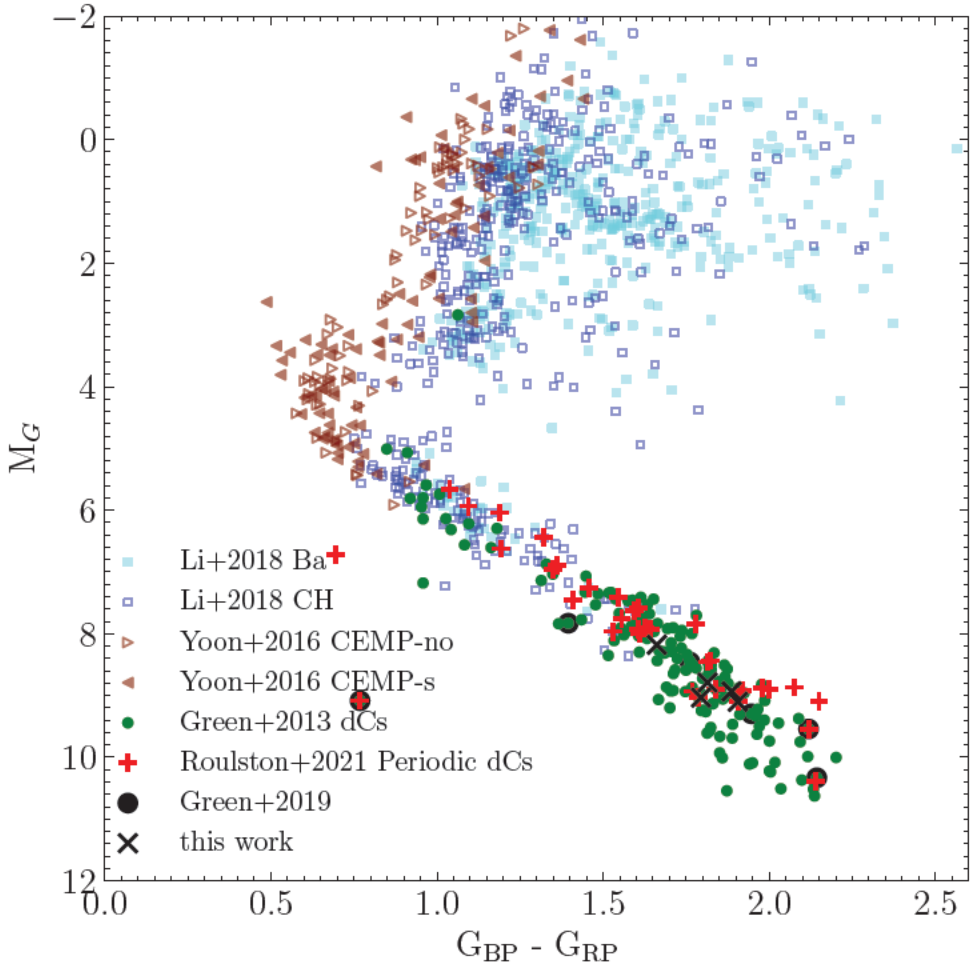

Figure 4.2: Updated color-magnitude diagram from Green et al. (2019b). While I only analyze main sequence stars in this chapter, I include the C-rich subgiants and giants in this plot merely to illustrate that they may be the evolved descendants of dC stars, which all together present a C-rich HR diagram. Further studies comparing e.g., the binary orbital properties, kinematics, and abundances of these samples can confirm this hypothesis. I show only those carbon-enhanced stars with $\varpi/\sigma_{\varpi} > 10$ from *Gaia* EDR3 (Gaia Collaboration et al., 2021). The majority of dCs come from the SDSS samples of Green (2013), Si et al. (2014), and the LAMOST sample from Li et al. (2018). I show the more evolved carbon-enhanced stars (i.e. Ba, CH, and CEMP-s/no stars) from the Yoon et al. (2016) and Li et al. (2018) samples. Additionally, I show important samples of dCs: the sample of periodic dCs from Roulston et al. (2021), the *Chandra* sample from Green et al. (2019b) and the sample from this work, with the latter two populating the low-luminosity red tail of this sequence.

Table 4.2: The ObsID, date, and exposure time are listed for each individual observation. For the dCs with detections (J0435, SBSS1310), the net count rate is shown. For each detected exposure, the column density (N_H) from Green et al. (2019a) is used with two different assumed plasma temperatures of 2 MK and 10 MK. For each assumed plasma temperature, the observed source flux, unabsorbed source flux, and source luminosity are calculated in the 0.3–8.0 keV range. The 1σ errors for each property are shown. For dCs without a detection, the 3σ upper limits are shown assuming the same set of plasma temperatures.

Object	ObsID	Obs-Date	Exposure	Net Count Rate	N_H	T_X	$F_{X,obs}$	F_X	L_X
			[ks]	[cnt ks^{-1}]	[10^{19} cm^{-2}]	[MK]	[10^{-15} erg cm^{-2} s^{-1}]		[10^{28} erg s^{-1}]
J0435	22298	2019-09-15	10.12	$2.61^{+0.33}_{-0.27}$	$6.3^{+0.7}_{-1.1}$	2	230^{+57}_{-38}	246^{+61}_{-41}	$48^{+12}_{-8.0}$
...	...	...	...	...	...	10	$31.6^{+7.8}_{-5.2}$	$32.3^{+8.0}_{-5.3}$	$6.3^{+1.6}_{-1.0}$
...	23376	2020-12-15	19.81	$2.39^{+0.22}_{-0.19}$	...	2	319^{+56}_{-42}	341^{+60}_{-45}	$66^{+12}_{-9.0}$
...	...	...	...	...	...	10	$36.0^{+6.4}_{-4.7}$	$36.8^{+6.5}_{-4.8}$	$7.1^{+1.3}_{-1.0}$
...	24305	2020-12-20	9.83	$2.23^{+0.91}_{-0.25}$	...	2	299^{+83}_{-53}	319^{+89}_{-57}	62^{+17}_{-11}
...	...	...	...	...	...	10	$33.7^{+9.3}_{-6.0}$	$34.5^{+9.6}_{-6.2}$	$6.7^{+1.9}_{-1.2}$
...	24306	2021-12-20	11.42	$2.50^{+0.55}_{-0.45}$	...	2	428^{+185}_{-125}	458^{+199}_{-134}	88^{+38}_{-26}
...	...	...	...	...	...	10	$42.3^{+18.0}_{-12.0}$	$43.3^{+19.0}_{-13.0}$	$8.4^{+3.6}_{-2.5}$
...	24893	2020-12-21	17.83	$2.77^{+0.25}_{-0.21}$	...	2	371^{+64}_{-48}	397^{+68}_{-51}	77^{+13}_{-10}
...	...	...	...	...	...	10	$41.8^{+7.2}_{-5.4}$	$42.7^{+7.4}_{-5.5}$	$8.3^{+1.4}_{-1.1}$
...	24896	2020-12-20	19.81	$3.17^{+0.23}_{-0.23}$	...	2	424^{+56}_{-56}	454^{+60}_{-60}	88^{+12}_{-12}
...	...	...	...	...	...	10	$47.8^{+6.3}_{-6.3}$	$48.9^{+6.5}_{-6.5}$	$9.5^{+1.3}_{-1.3}$
...	26242	2021-12-20	17.23	$2.76^{+0.46}_{-0.40}$	...	2	472^{+83}_{-61}	505^{+89}_{-65}	98^{+17}_{-13}
...	...	...	...	...	...	10	$46.6^{+8.2}_{-6.0}$	$47.7^{+8.4}_{-6.2}$	$9.2^{+1.6}_{-1.2}$
J0546	22299	2020-01-09	34.80	< 0.20	$7.5^{+1.5}_{-0.6}$	2	< 18	< 24	< 7.2
...	...	...	...	...	...	10	< 2.5	< 2.8	< 0.9
HE1205	22300	2020-04-04	24.23	< 0.44	$8.4^{+1.3}_{-1.2}$	2	< 47	< 51	< 14
...	...	...	...	...	...	10	< 5.9	< 6.1	< 1.7
J1240	22301	2019-09-19	36.78	< 0.34	$6.3^{+0.8}_{-1.2}$	2	< 31	< 32	< 10
...	...	...	...	...	...	10	< 4.2	< 4.3	< 1.3
SBSS1310	22302	2020-01-25	14.90	$1.98^{+0.24}_{-0.19}$	$3.0^{+1.8}_{-1.7}$	2	203^{+47}_{-32}	210^{+49}_{-33}	$40.7^{+9.5}_{-6.4}$
...	...	...	...	...	...	10	$25.9^{+6.0}_{-4.1}$	$26.2^{+9.2}_{-4.1}$	$5.1^{+1.2}_{-0.8}$

Table 4.3 lists the ObsIDs for each dC, the observation properties, and the X-ray source properties for each dC. The calculated net count rate for each ObsID is given, with the 1σ upper and lower error limits. For the three dCs with no detections, the 3σ upper limits are given. Following Green et al. (2019b), I derived two X-ray flux estimates, using both a 2 MK and a 10 MK optically thin plasma (APEC; Smith et al., 2001) with absorption modeled using WABS (Morrison & McCammon, 1983). I list the 1σ upper and lower limits for the two dCs with detections for the net count rate, observed flux, unabsorbed flux, and X-ray luminosity. For the three dCs without detections, I list the 3σ upper limits.

4.3.1 Individual Spectral Fits

For the dCs SBSS1310 and J0435, I have also fit individual spectral models for each observation. These individual fits use the same APEC and WABS models as before, but now fit the plasma temperature, column density, and normalization as free parameters.

SBSS1310

The best fitting model for SBSS1310 consists of a 12.1 MK plasma temperature with a low column density (3σ upper limit of $N_H = 9.6 \times 10^{21}\,cm^{-2}$). This column density is consistent with the negligible Bayestar17 expected line of sight column density of $N_H = 3 \times 10^{19}\,cm^{-2}$.

Figure 4.3 shows the best fit spectral model for SBSS1310. The left panel shows the observed source spectrum with the associated errors and the best fitting model. The right panel shows the error contours for the fit parameters, with the best-fit parameters shown as the blue marker. The Bayestar17 expected line of sight column

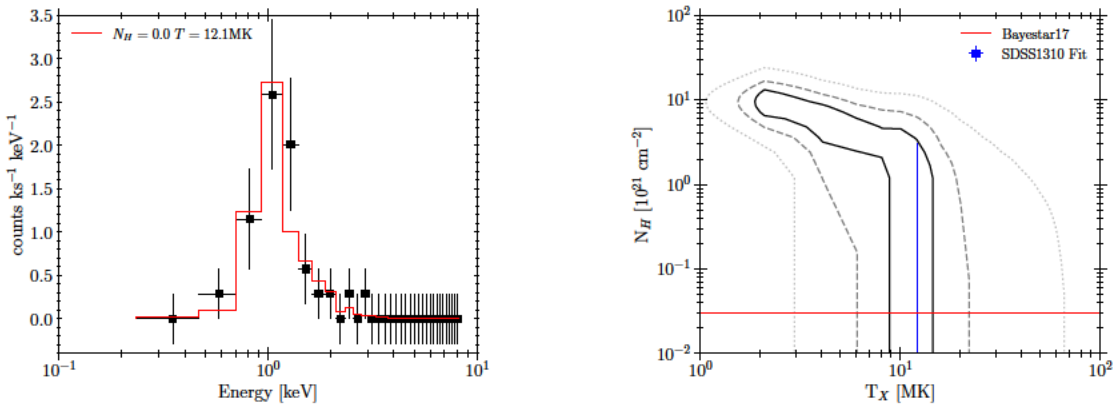

(a) **(b)**

Figure 4.3: Best fitting spectral model for SBSS13010. The left panel, (a), shows the observed source spectrum in black with the associated errors. The best fitting model is shown as the solid red line. The right panel, (b), shows the contours for the plasma temperature and column density, with the 1σ, 2σ, 3σ contours shown as the solid, dashed and dotted lines respectively. These contours were calculated by varying the plasma temperature and column density over a grid and calculating the confidence with a χ^2 statistic using the Sherpa package (Freeman et al., 2001). The best fit parameters are shown as the blue marker, with the 1σ errors. The Bayestar17 expected line of sight column density is shown as the red dashed line for reference.

density is shown as the red dashed line for reference. The resulting model is consistent with the expected negligible column density, and with the assumed 10 MK plasma temperature from (Green et al., 2019b). Green et al. (2019b) assumed this 10 MK plasma temperature based on X-ray-selected stellar samples observed with *Chandra* from, e.g., the COSMOS survey (Wright et al., 2010).

J0435

The requested 100 ksec was split by *Chandra* mission planners into seven separate observations of J0435. As with SBSS1310, I fit each observation with a spectral model with plasma temperature and column density as free parameters. For each ObsID, the resulting plasma temperature and column density are listed in Table 4.3.1 with their 1σ errors. All of the fits result in a column density three orders of magnitude higher than the expected line of sight column density from Bayestar17 dust map ($N_H = 6.3 \times 10^{19}\,cm^{-2}$), which suggests the presence of material around J0435 (see Section 4.4). The fit plasma temperatures are consistent with the higher assumed values of the 10 MK models. Figure 4.5 shows the resulting best fit parameters for J0435. The colored scatter points show the best fitting parameters for the individual fits, with their errors.

In addition to the individual fits, I simultaneously fit all seven observations with one model. For this fit, I used the same APEC and WABS models as before, but all seven observations are fit with the same plasma temperature and column density, allowing only the normalization to vary between each observation.

The simultaneous fit results in a column density of $N_H = 1.77 \pm 0.30 \times 10^{22}\,cm^{-2}$ and a plasma temperature of $T_X = 14.2 \pm 2.9$ MK. Figure 4.4 shows both the individual and simultaneous fits for J0435. For each observation, the observed source spectrum

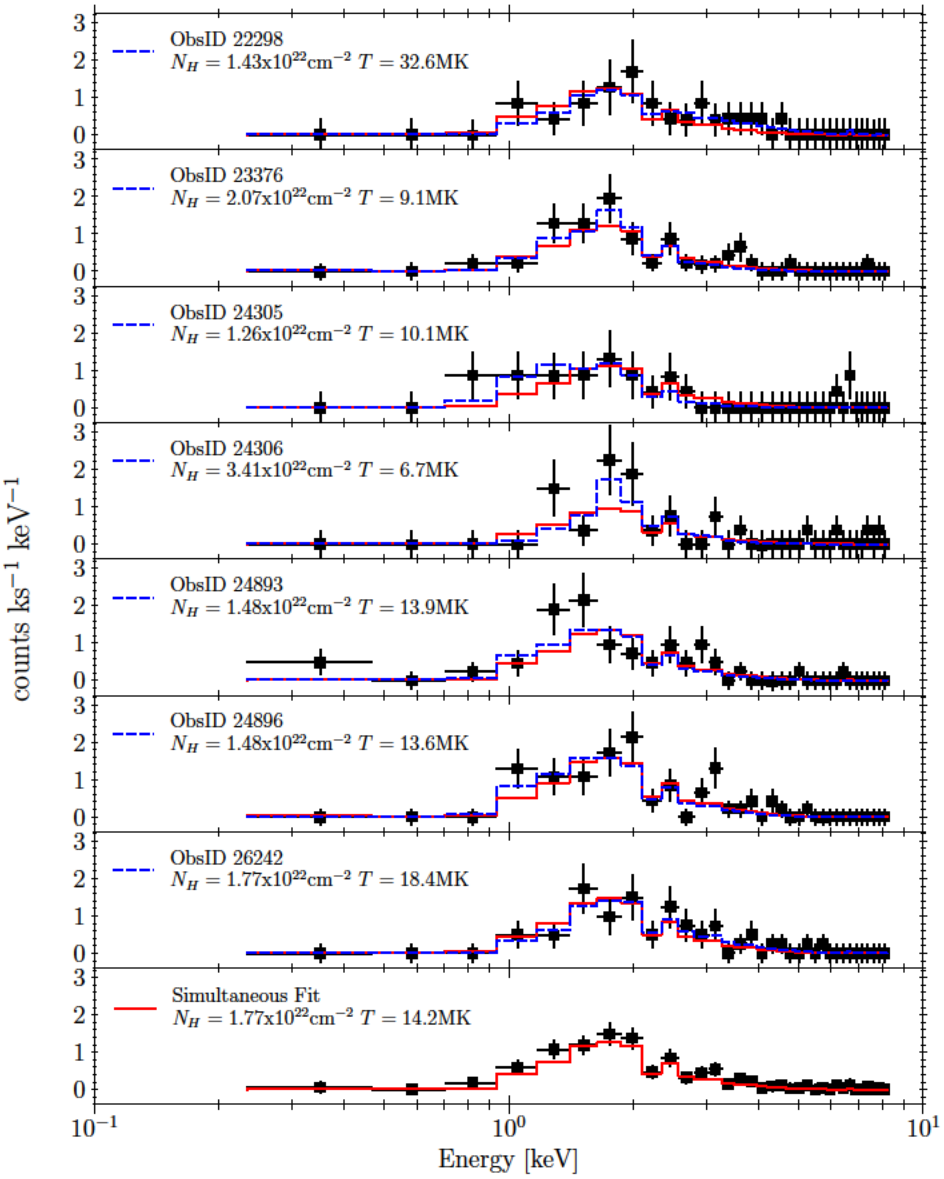

Figure 4.4: *Chandra* count rate spectrum in the range 0.3–8.0 keV for J0435. Each of the seven individual ObsIDs is shown, respectively, in the upper seven panels. Each of the individual observations is fit separately with the same model. The resulting fit for each is shown as the blue dashed line in each panel, with the fit parameters shown in the panel. The combined spectrum of all seven observations is shown in the bottom (last) panel. I fit all seven observations simultaneously, forcing the same column density and plasma temperature, but leaving the model normalization free to be fit for each observation. The resulting simultaneous fit is shown as the solid red line in each panel.

Table 4.3: Individual model fits for each ObsID of J0435. Each model uses the same model, but is fit independently. The 1σ errors for each fit parameter are shown.

ObsID	$N_{\rm H,fit}$ $[10^{22}$ cm$^{-2}]$	$T_{\rm X,fit}$ [MK]
22298	$1.43^{+0.33}_{-0.32}$	$33^{+11}_{-5.0}$
23376	$2.07^{+0.25}_{-0.13}$	$9.1^{+1.3}_{-1.3}$
24305	$1.26^{+0.30}_{-0.18}$	$10.1^{+1.8}_{-1.3}$
24306	$3.41^{+1.44}_{-0.44}$	$6.7^{+1.5}_{-1.4}$
24893	$1.48^{+0.14}_{-0.32}$	$13.9^{+1.8}_{-1.2}$
24896	$1.48^{+0.22}_{-0.28}$	$13.6^{+1.4}_{-1.4}$
26242	$1.77^{+0.87}_{-0.63}$	$18.4^{+2.6}_{-1.5}$

Table 4.4: Combined model fits for each ObsID of J0435. For each observation, the observed source flux, unabsorbed flux, and luminosity are listed. For each value the 1σ errors are shown.

ObsID	$F_{\rm X,obs}$ $[10^{-15}$ erg cm^{-2} s$^{-1}]$	$F_{\rm X}$ $[10^{-15}$ erg cm^{-2} s$^{-1}]$	$L_{\rm X}$ $[10^{28}$ erg s$^{-1}]$
22298	$23.8^{+5.5}_{-4.4}$	170^{+39}_{-32}	$32.9^{+7.5}_{-6.1}$
23376	$23.1^{+3.9}_{-3.3}$	165^{+28}_{-23}	$31.9^{+5.4}_{-4.5}$
24305	$21.5^{+5.5}_{-4.3}$	154^{+40}_{-31}	$29.8^{+7.6}_{-6.0}$
24306	$24.9^{+5.5}_{-4.5}$	178^{+40}_{-32}	$34.5^{+7.6}_{-6.2}$
24893	$26.7^{+4.4}_{-3.7}$	191^{+32}_{-27}	$37.0^{+6.1}_{-5.2}$
24896	$30.6^{+4.1}_{-4.1}$	219^{+29}_{-29}	$42.4^{+5.6}_{-5.6}$
26242	$27.4^{+4.6}_{-3.9}$	196^{+33}_{-28}	$37.9^{+6.4}_{-5.4}$

is shown, with the best fitting individual model shown as a dashed blue line. The best fit simultaneous model is shown as the red solid line. The bottom panel shows the combined source spectrum, with the total simultaneous fit model.

4.3.2 X-ray Variability

Since coronal activity is by nature variable, I searched for signs of X-ray variability in the dCs observed to date. I used the CIAO implementation of the Gregory-Loredo variability algorithm (Gregory & Loredo, 1992) `glvary`. I tested all available ObsIDs for dCs in both the Green et al. (2019b) sample and this work. I found that none

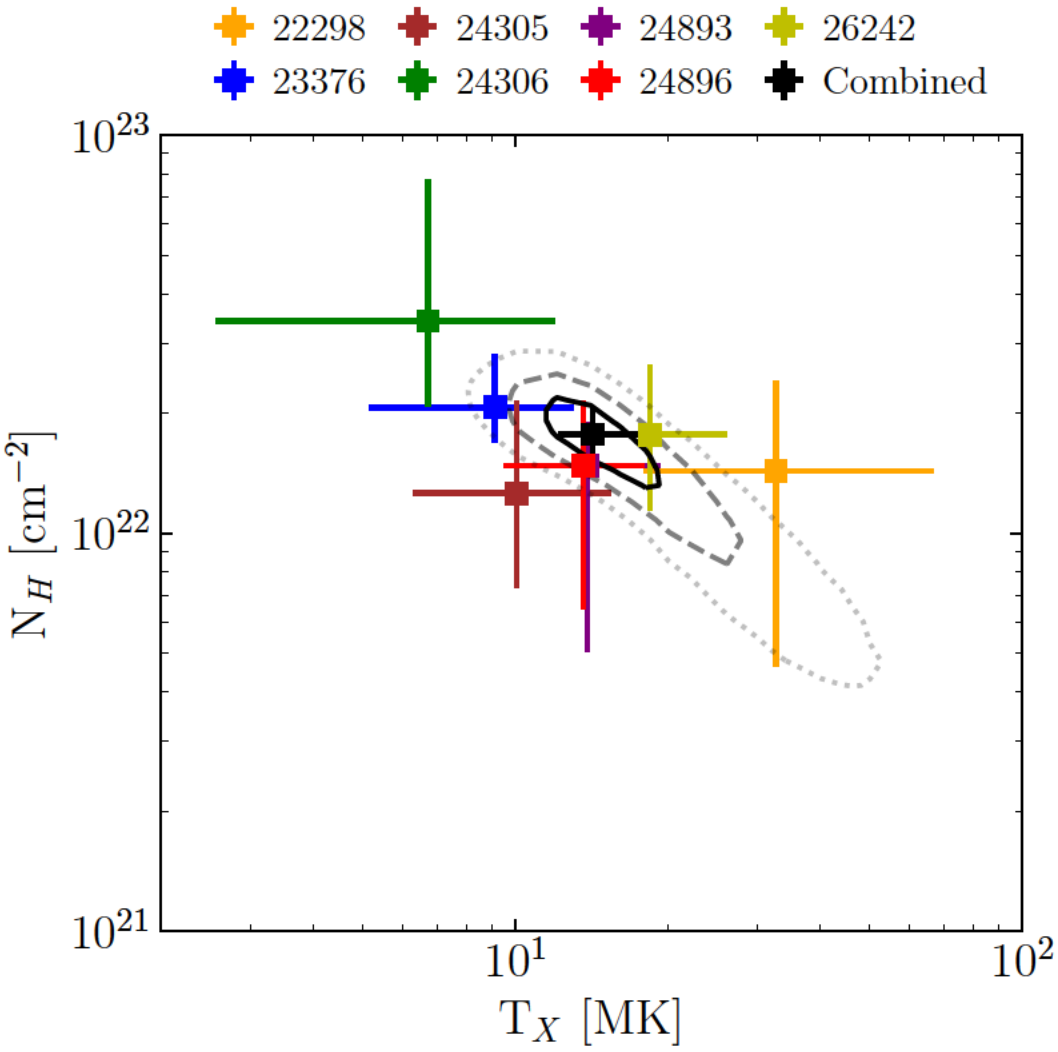

Figure 4.5: Fit values of the model column density (N_H) and plasma temperature (T_X) for the dC J0435. The individual observations are shown as the color scatter points with their respective 1σ errors. The red scatter point is the best fit for the combined set of all seven observations. The black contours represent the 1, 2, and 3σ regions for the combined fit. The expected column density at the distance of J0435 from the 3D optical/IR dust maps of Green et al. (2019a) ($N_H = 6.3 \times 10^{19}$ cm^{-2}) is more than two orders of magnitude lower than the values shown here from X-ray fitting.

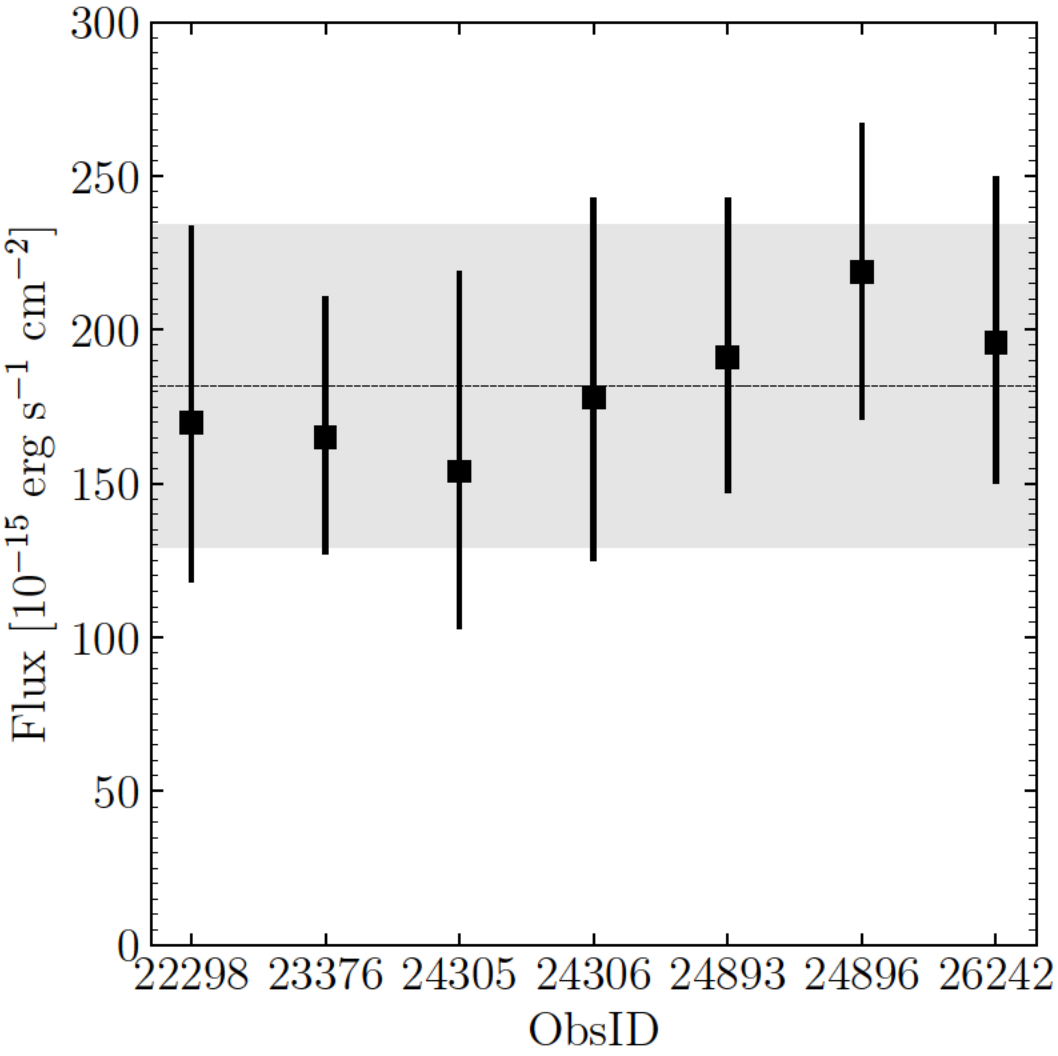

Figure 4.6: Unabsorbed model flux for each ObsID of the dC J0435. For each ObsID, the flux is calculated using the combined fit model parameters (see Figures 4.4 and 4.5). The dashed black line is the mean of the seven observations, with the grey shaded region showing the mean error of the observations. I find no signs of variability in the source flux of J0435. Note that all the ObsIDs for J0435 span some 28 months, but several are clustered within a few days so I plot by ObsID here, which does not map to MJDs (listed in Table 4.3).

of the dCs in Green et al. (2019b) show significantly variable count rates, with all having a variability index[1] of 0 or 1.

From this work, I found that SBSS1310 has a variability index of 2 and is considered not variable. For J0435, the variability indices are 6, 2, 0, 0, 0, 6, 0 for the ObsIDs 22298, 23376, 24305, 24306, 24893, 24896, and 26242 respectively. The ObsIDs with variability index equal to 6 are considered definitely variable; variability index equal to 2 is considered probably not variable, and variability indexes of 0 are considered definitely not variable.

One possible explanation for this changing variability index may lie with the source of the X-ray emission in dCs, which is believed to be from coronal emission associated with rotation and magnetic activity. Stellar flares are associated with magnetic activity and magnetic reconnection (Pettersen, 1989), where most of the flare coronal emission is in X-rays. As dCs show X-ray emission and are thought to have rejuvenated activity, dCs are expected to flare at similar rates as active M dwarfs. As flares are transient, stochastic events, the resulting X-ray emission will also be transient and stochastic. If J0435 has an active corona, some continuous level of X-ray emission should be observed. During a flare however, the X-ray emission should increase with a lifetime of the flare. These flares could be the source of the differing levels of variability between the J0435 observations. To check for flares from J0435, I searched the *TESS* (Ricker et al., 2015) light-curve but found no detected flare events in the full frame images. However, given that for cool stars the flare duration is of order one hour (Howard et al., 2019), the 30 min cadence of this light curve may not resolve any flares outside of single point outliers.

Additionally, for J0435, I used the best simultaneous fit model parameters to

[1] https://cxc.cfa.harvard.edu/ciao/ahelp/glvary.html

calculate the observed flux, unabsorbed flux, and source luminosity in the 0.3–8.0 keV range for each ObsID. These values are listed in Table 4.3.1 with their 1σ upper and lower limits. Figure 4.6 shows the unabsorbed model flux for each ObsID. The 1σ error bars are shown for each, with the shaded region showing the average 1σ error across all seven observations. Within these errors, I find no detectable variability in the source flux of J0435.

4.3.3 Rotation-Activity Relationship

In main-sequence stars, X-ray emission, and often chromospheric Hα emission, is associated with coronal activity due to magnetic activity. This activity is thought to be produced by an $\alpha\Omega$ dynamo (Parker, 1955) which requires a differentially rotating convective envelope and a solidly rotating radiative core. However, it has been found that even late-type, fully convective stars show magnetic activity associated with rotation (Wright et al., 2018). The Rossby number $Ro = P_{rot}/\tau$ (Noyes et al., 1984), which relates the rotation period to the convective turnover time (τ), has been shown to correlate with activity and saturates for rapid rotators at the level of $\log(L_x/L_{\rm bol}) \approx -3.3$ for $Ro \lesssim 0.13$ (Micela et al., 1985; Wright et al., 2011).

In Green et al. (2019b), all six of the observed dCs were detected with *Chandra*, with $\log(L_x/L_{\rm bol})$ ranging from -4.5 to -3.2, depending on the assumed model plasma temperature. These values place the dCs in the saturated regime for stellar rotation; however, at the time, no rotation periods were known for these stars. The recent studies by Roulston et al. (2021) and Whitehouse et al. (2021) have found many new periods for dC stars, including five of the six in the Green et al. (2019b) sample. One of the detections in this work, SBSS1310, is in both Roulston et al. (2021) and Whitehouse et al. (2021). However, J0435 does not have a known rotation

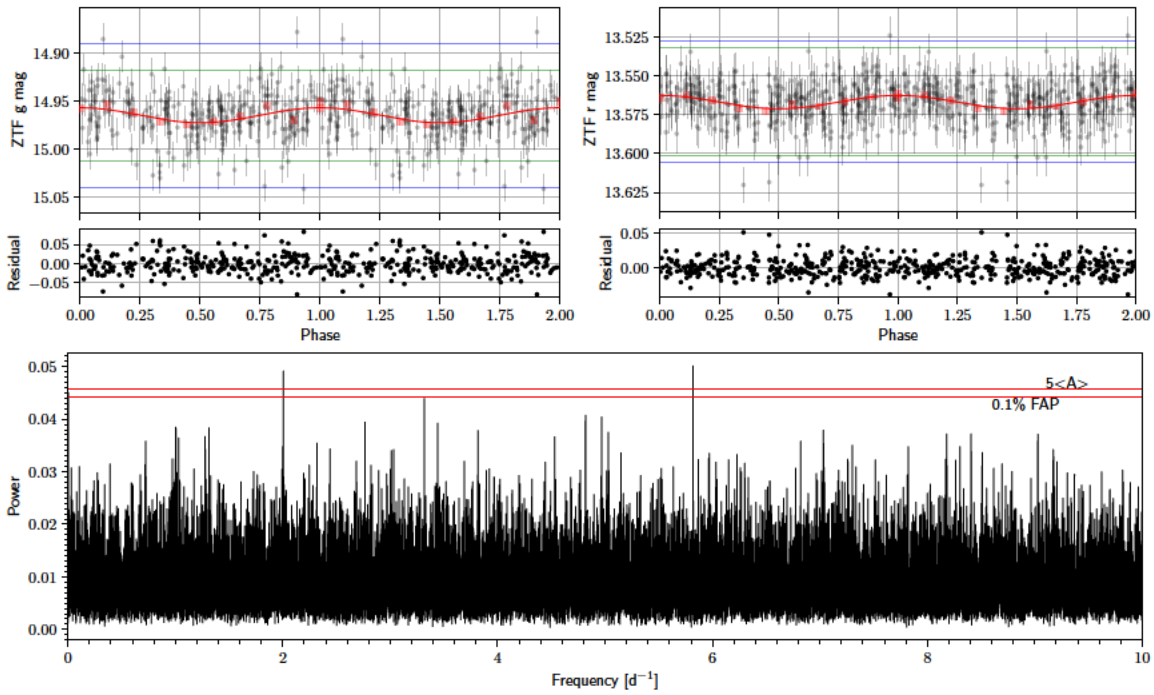

Figure 4.7: Zwicky Transient Facility light curves for J0435. The top panels show the light-curves in both the g and r bands, folded on the best found significant period of 0.1719 ± 0.0016 d. The red line shows the best fitting model to the each phased light-curve, with residuals shown below the light-curve. The red square markers are the binned data in 10 phase bins. The multiband LS power spectrum is shown in the bottom panel, the $5\langle A \rangle$ or 0.1% FAP limits are marked by the dashed and dotted red horizontal lines respectively.

period in the literature.

I searched the light-curve of J0435 in the Zwicky Transient Facility DR5 (ZTF; Bellm et al., 2019; Masci et al., 2019; Graham et al., 2019). for periodic signals. I used similar methods as detailed in Roulston et al. (2021), explained briefly here. I used an outlier removal procedure to clean the raw light-curve, before searching for periodic signals using a Lomb-Scargle periodogram (LS; Lomb, 1976; Scargle, 1982). While there were no significant peaks in the individual ZTF light curves, I used the multiband periodogram from VanderPlas & Ivezić (2015) to search for shared variability in both the g and r bands. To consider a peak in the power spectrum as

significant, I used the $5\langle A \rangle$ (five times the mean power) limit as well as the 0.1% false-alarm probability (FAP) limit (see Greiss et al. 2014 and Hermes et al. 2015 for more details). Additionally, I required that the peak frequency must be separated by at least $0.005\,\mathrm{d}^{-1}$ from an observational alias, such as $0.5\,\mathrm{d}^{-1}$ or $0.333\,\mathrm{d}^{-1}$.

The highest peak in the combined ZTF power spectrum for J0435 meets both of these requirements, so I take the period to be $0.1719 \pm 0.0016\,\mathrm{d}$. I do note the caveat that this period is assumed to be both the rotation period and orbital period under the assumption that in a close binary system, it would be expected to be in a synchronized (Hurley et al., 2002), low eccentricity orbit. Figure 4.7 shows the ZTF light-curve for J0435 folded on the highest found significant peak. The best fitting single sinusoidal model to the data is shown for each band as the solid red line, with the residuals below. The bottom panel shows the power spectrum, and the power needed to reach the $5\langle A \rangle$ or 0.1% FAP limits. J0435 also has a light curve in the Catalina Real-Time Transient Survey (Drake et al., 2009), but including this light curve in the multiband periodogram results in the same period and significance as the ZTF only analysis. Since the Catalina data have much larger errors, I do not include them in the multiband analysis.

With the newly found periods for the dCs in Green et al. (2019b) and this work, I can now place dCs on an activity-rotation diagram. Figure 4.8 shows the updated Figure 3 of Green et al. (2019b), but I now show the true position of the five dCs in that sample with their rotation periods (the one dC from that sample without a rotation period is still shown with horizontal lines). I additionally place the two new X-ray detected dCs from this work, SBSS1310 and J0435, on this diagram. For SBSS1310 I include both the 2 MK and 10 MK model values, both placing SBSS1310 in the saturated regime. For J0435, I use the simultaneous fit model, making it the

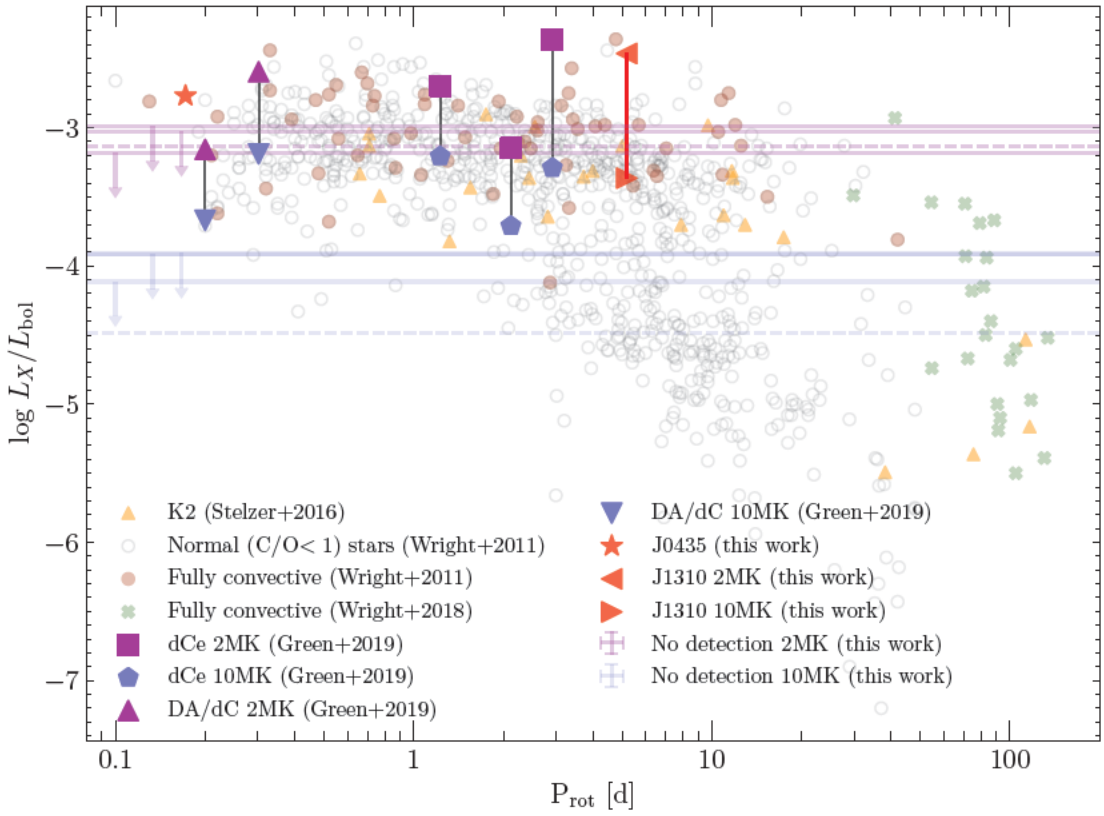

Figure 4.8: Updated activity-rotation figure from Green et al. (2019b). For context, the activity and rotation for normal (C/O < 1) main-sequence stars are shown in the background. The logarithm of X-ray to bolometric luminosity is plotted against rotation period for the normal dwarf stars from the samples of: Wright et al. (2011), Stelzer et al. (2016), and Wright et al. (2018). I show the dCs from the Green et al. (2019b) *Chandra* sample and use the recently found rotation periods from Roulston et al. (2021) and Whitehouse et al. (2021) to place those dCs at their true location on the diagram, assuming both 2MK and 10MK APEC plasma models for X-ray emission. The X-ray detected dC J1548 from the Green et al. (2019b) sample does not have a rotation period and so is marked by horizontal dashed lines. Finally, I show the two dCs with new X-ray detections reported in this chapter, J0435 and SBSS1310, as well as the 3σ upper limits for the three non-detections. The rotation period for SBS1310 comes from Roulston et al. (2021), and the rotation period for J0435 is from this chapter. For J0435, I use the simultaneous best-fit X-ray model of 13.4MK (section 4.3.1). It is clear that for either 2 MK and 10 MK models, most dCs are found in the saturated regime of active stars.

best-constrained dC of both samples. J0435 is clearly in the saturated regime with a short rotation period ($P = 0.1719\,\mathrm{d}$) and $\log(L_x/L_{\mathrm{bol}}) = -2.77$.

The dC sample of Green et al. (2019b) was chosen because its stars were *expected* to show X-ray activity due to being either composite spectroscopic binaries of the dC+DA type, or showing signs of chromospheric activity with Hα emission. This suggested that dCs have experienced spin-up from the angular momentum of the accreted material during mass transfer. As dCs are believed to be from older thick disk and halo populations (Green, 2013; Farihi et al., 2018), they are expected to have spun-down from magnetic braking and angular momentum loss through magnetized winds (Kraft, 1967; Matt et al., 2015; Garraffo et al., 2018); therefore, any signs of short rotation periods would be indicators of mass transfer spin-up. Indeed, the location of the dCs from Green et al. (2019b) in the rotation-activity diagram indicated short rotation periods, which have now been confirmed by Roulston et al. (2021) and Whitehouse et al. (2021).

The dCs in the current study were selected to investigate if dCs, regardless of Hα emission or a spectroscopically detectable WD, show signs of spin-up and chromospheric rejuvenation. Indeed, I find that the two dCs with X-ray detections in this work are both in the saturated activity regime with short rotation periods.

However, the recent works of Roulston et al. (2021) and Whitehouse et al. (2021), where a large number of new dC periods were found, complicate the interpretation of activity as resulting only from accretion-induced spin-up (Green et al., 2019b). Remarkably, 95% of the new dC periods are under 10 d, with nine having been confirmed to have the same photometric (likely rotational) period and orbital period. Since dCs form via mass transfer from evolved TP-AGB stars and TP-AGB stars can reach radii of $800\,\mathrm{R}_\odot$ (3.7 au) as they experience successively stronger thermal

pulses (Marigo et al., 2017), these short period dC stars must have experienced a common-envelope phase (Paczynski, 1976; Ivanova et al., 2013). Therefore, the dCs in this chapter, and in Green et al. (2019b), must have experienced a CE phase and the associated spiral-in to these short periods. This spiral-in results in the circularization and subsequent synchronization of the binary (Hurley et al., 2002), and therefore the resulting final dC should have a rotation period commensurate with PCEBs, i.e. P$\approx$ 1 d. Thus, the X-ray detections in Green et al. (2019b) and in this work do indeed trace short period rotation of dCs; however, the cause of this dC spin-up is more likely associated with common-envelope spiral-in, and subsequent spin-orbit locking in the binary system with the remnant WD, and not necessarily angular momentum gain from accreting carbon-rich material. A more appropriate *Chandra* sample to probe accretion-induced spin-up would be to target dCs in which the orbital period is on the order of years. For example, the 3 dCs from Harris et al. (2018) (with astrometric periods of 1.23 yr, 3.21 yr, and 11.35 yr) should have avoided a common-envelope phase, and therefore, the rotation period should only have been affected by accretion.

4.4 J0435 Spectral Energy Distribution

The significant column density ($N_H = 1.77 \times 10^{22}\,cm^{-2}$) from the spectral fit of J0435 indicates the presence of substantial material along the line of sight. However, the expected intervening column density from the Bayestar17 dust maps ($N_H = 6.3 \times 10^{19}\,cm^{-2}$) suggest negligible amounts of dust in the direction and distance of J0435. This suggests that there may be either substantial circumbinary or circumstellar material around J0435.

The mass transfer process to form dCs requires the accretion of carbon-rich material from a former TP-AGB companion (which now as a WD, has cooled beyond

detection). The carbon-rich dust expelled by these TP-AGB stars has large opacity to optical and infrared photons, driving high radiation pressure and therefore large mass loss rates of $\sim 10^{-7}$–$10^{-5}\,\mathrm{M}_{\odot}\,\mathrm{yr}^{-1}$ (Höfner & Olofsson, 2018). This should result in extended shells of dust around nascent dC systems. In addition, those dCs that experience a common-envelope phase will eject the envelope of the TP-AGB star resulting in a planetary nebula. This seems to be observed in the Necklace Nebula where the central source was found to be a binary with a dC, having a photometric period of 1.16 d (Corradi et al., 2011; Miszalski et al., 2013). As the WD companion to the newly minted dC cools, the planetary nebula should similarly fade (on typical timescales of $\sim 10^4$ years), but may leave detectable signs of circumbinary dust and gas around the dC. Given that dC main sequence lifetimes can exceed planetary nebula lifetimes by a factor of $\sim 10^5$, it is perhaps a surprise that even one dC is known within a cataloged PN.

I compiled the spectral energy distribution (SED) of J0435 using a variety of catalog observations. In the optical, I cross-matched to *Gaia* EDR3 (Gaia Collaboration et al., 2021) and the Pan-STARRS1 survey (Chambers et al., 2016; Magnier et al., 2020a; Waters et al., 2020; Magnier et al., 2020b,c; Flewelling et al., 2020). In the near-infrared and mid-infrared, I cross-matched to the Two Micron All-Sky Survey (2MASS; Skrutskie et al., 2006) and *WISE* surveys respectively. I also cross-matched to the GALEX GR6/7 (Martin et al., 2005) finding only a near-ultraviolet (NUV, 130–180 nm) detection for J0435.

I obtained deeper NUV and far-ultraviolet (FUV) observations of J0435 using the Wide Field Camera 3 (WFC) and Advanced Camera for Surveys (ACS) detectors on the *Hubble Space Telescope* (HST). I obtained NUV images with WFC3 using the F225W filter, across one full orbit with a total exposure time of 2384.0s. The

exposure was split into four equal exposures of 596.0s and dithered using the WFC3-UVIS-DITHER-BOX pattern, with point spacing of 0.173″ and line spacing of 0.112″. I obtained FUV images with the Solar Blind Channel (SBC) on the ACS using both the F140LP and F165P filters[2]. Observations with both filters were obtained within one orbit, with a total exposure of 1084.0s and 1091.0s in the F140LP and F165LP filters respectively. Exposures in both filters were split into four equal exposures (271.0s, 272.75s) and dithered using the ACS-SBC-DITHER-BOX pattern, with point spacing of 0.179″ and line spacing of 0.116″.

I measured the NUV and FUV magnitudes in a similar way. I used the *Gaia* EDR3 positions and proper motions to update the coordinates of J0435 to the time of the *HST* observations. I performed simple aperture photometry using a circular aperture (with radius 0.8″ and 0.2″ for the NUV/FUV images respectfully) for the source and an annulus (with inner and outer radii of 2″ and 4″ for the NUV and 0.5″ and 4.5″ for the FUV) for the background region. For both the NUV and FUV images, I correct the aperture counts using the provided encircled energy fractions[3][4]. The measured NUV (F225W) magnitude is 22.224 ± 0.003, and the measured FUV (1400Å–1650Å) magnitude is extremely faint, at 29.04 ± 0.95.

Figure 4.9 shows the SED of J0435 with the catalog and new *HST* fluxes. I fit a blackbody model to the SED of J0435, excluding the *HST* and GALEX FUV/NUV fluxes. I corrected for the expected extinction by using the Bayestar17 dust maps (Green et al., 2018). I used the extinction law from Cardelli et al. (1989), assuming $R_V = 3.1$, to calculate the extinction in the observed bands. The fit results in a dC temperature of $4026\,\mathrm{K} \pm 78\,\mathrm{K}$ and dC radius of $0.48\,\mathrm{R}_\odot \pm 0.15\,\mathrm{R}_\odot$. This best-fit model

[2]I obtained FUV images in both filters to account for the SBC red leak.

[3]https://www.stsci.edu/hst/instrumentation/wfc3/data-analysis/photometric-calibration/uvis-encircled-energy

[4]https://www.stsci.edu/hst/instrumentation/acs/data-analysis/aperture-corrections

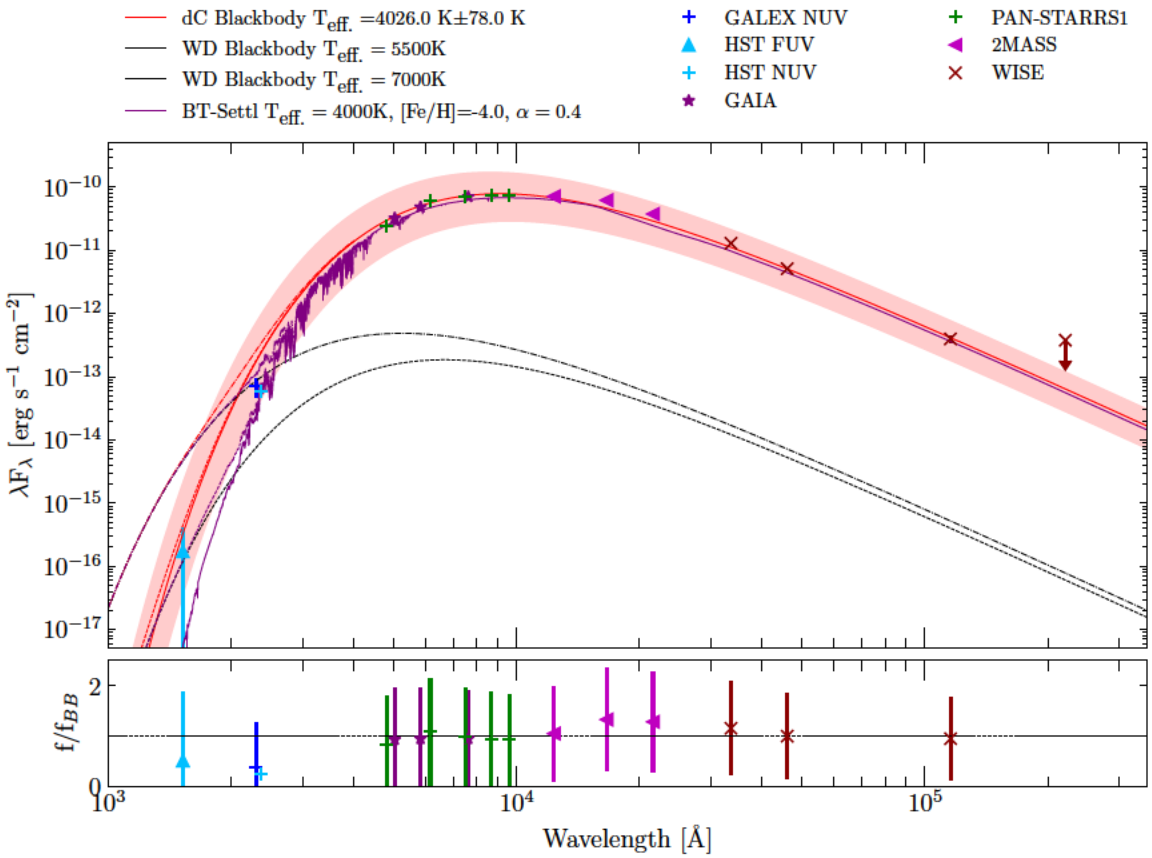

Figure 4.9: Spectral energy distribution for the dC J0435. The SED was compiled from *Gaia* EDR3 and Pan-STARRS1 in the optical, GALEX in the NUV, 2MASS in the near-infrared, *WISE* in the mid-infrared, and new *HST* observations in the NUV/FUV regions. The best fitting blackbody model is shown as the solid red line and consists of a 4026 K±78 K dC with a radius of 0.48 $R_\odot \pm 0.15$ $R_\odot$. The red shaded region shows the 1σ uncertainty of this best-fit model. The bottom panel shows the observed flux divided by the expected flux from the best-fit blackbody for each observation; error bars represent the blackbody fit errors added in quadrature to the photometric flux uncertainties. Also shown is a BT-Settl model atmosphere (Allard et al., 2011) with [Fe/H]= -4.0 and $\alpha = 0.4$, normalized to the *Gaia* EDR3 distance and fit radius (again with the shaded purple region showing the 1σ uncertainty). The black dashed and dotted-dashed lines show two blackbodies of a 7000 K and 5500 K respectively meant to describe the WD. For each WD model, the combined dC blackbody and combined BT-Settl models are shown. The new *HST* fluxes are consistent with a 4000 K main-sequence star combined with a cool WD. The FUV flux places a weak constraint of approximately 5500 K on the WD companion. In addition, there appears to be a slight increase in the near-infrared flux as compared to the best-fit blackbody, but within the 1σ uncertainty region.

is shown as the solid red line in Figure 4.9, with the shaded red region representing the 1σ uncertainty region from this fit. Also shown (as the solid purple line) is a 4000 K BT-Settl model atmosphere (Allard et al., 2011) with [Fe/H]$= -4.0$ and $\alpha = 0.4$, normalized to the *Gaia* EDR3 distance and fit radius. Figure 4.9 also shows two blackbodies for a WD of 7000 K and 5500 K. For both WD blackbodies, I show the combined dC blackbody and dC BT-Settl model atmosphere as dashed lines.

The dC blackbody model fit reproduces the observed dC SED moderately well, with the BT-Settl model atmosphere matching more closely in the UV region. The measured *HST* NUV flux is consistent with that of the GALEX NUV flux, and the flux from a 4000 K main-sequence BT-Settl model. Although the *HST* flux has a fairly large uncertainty, it is consistent with the fit dC temperature and a cool WD companion. From Figure 4.9, it is clear the WD must be cooler than 7000 K or a slightly higher NUV flux would have been observed, and the FUV detection should have been much stronger. If I use the FUV flux as an upper limit of the WD flux contribution, I find the WD is likely around 5500 K implying a cooling age (therefore the time since mass transfer to the dC) of approximately 3.5 Gyr (using a standard WD mass of 0.6 $M_\odot$), assuming that there have been no accretion episodes since.

Circumbinary and circumstellar dust around J0435 should re-emit absorbed radiation in the mid-infrared. This should be visible as a bump in the infrared region of the SED. While there does appear to be a slight bump in the SED of J0435 in the 2MASS fluxes, it is within the 1σ uncertainties of the blackbody fit, supporting the non-detection of a dusty disk in the SED of J0435. Additionally, the SED is well fit using the negligible extinction from the Bayestar17 dustmaps, pointing again to a lack of dust along the line of sight to J0435.

4.5 Discussion

Green et al. (2019b) sought to determine if dCs, while expected to be of older thick disk and halo populations (Green, 2013; Farihi et al., 2018), may still show signs of coronal activity due to rapid rotation induced by an increase in angular momentum from mass transfer. While they did indeed find that all of their observed dCs were detected with *Chandra* and consistent with saturated X-ray activity, their pilot sample was biased to enhance detection probability, targeting dCs showing $H\alpha$ emission, a known tracer of coronal activity.

Following up on the successful detection of those dCs, the sample in this chapter aimed to study a more representative sample, targeting the five nearest known dCs regardless of Hα emission. Of the five dCs targeted, I detect X-ray emission in two. I use the same assumed 2 MK and 10 MK plasma temperature models to calculate $\log(L_x/L_{\rm bol})$, finding that both of those dCs fall in the saturated regime. For the three non-detections, I place 3σ upper-level constraints on the X-ray flux.

For the dC J0435, I have seven individual *Chandra* observations, with a total of 289 counts. This allowed us to fit the X-ray spectrum, placing constraints on the plasma temperature ($\rm T_X = 14.2\,MK$) and column density ($\rm N_H = 1.77 \times 10^{22}\,cm^{-2}$). The column density suggests a large amount of material surrounding J0435, but the lack of a mid-infrared excess in the SED, and the good SED fit without the need for a larger extinction correction, suggests that the material around J0435 may be gas with very little dust. The material may indeed be the remnants of the TP-AGB wind or common-envelope ejecta. This explanation is problematic, however, as the CE material would be expected to should have been cleared from the system, especially given the time since the CE was inferred from the estimated cooling age. There could be the remains of the AGB wind, the CE, or an accretion disk that was in the

form of dust but has been heated above the sublimation temperature by the strong X-ray activity found in J0435. The origin of this anomalous column density and low reddening motivates further multi-wavelength studies of J0435.

While the results here are consistent with Green et al. (2019b), recent works have shown that the previous interpretation of dC X-ray activity, as primarily due to accretion spin-up, may not be complete. Roulston et al. (2021) and Whitehouse et al. (2021) recently found 40 dCs with photometric periods, with 95% having P$<$ 10 d. These dCs must have been engulfed in a common-envelope during their former giant companion's TP-AGB phase. This would have caused a spiral-in of the dC, after which tidal spin-orbit synchronization would lead to the observed short dC rotation periods. It appears that, compared to accretion-induced spin up as originally postulated by Green et al. (2019b), these spin-orbit-induced short rotation periods are more likely the source of the increased coronal activity as traced by the X-ray emission.

An interesting comparison to make is to the symbiotic stars (Davidsen et al., 1976; Allen, 1984; Luna et al., 2013). Symbiotic stars consist of a compact object in a bound orbit around a red giant and accreting from its wind. They are known to have orbital periods ranging from hundreds of days to thousands of days (Mikołajewska, 2012). The accretion in symbiotics is believed to take place via wind accretion or a form of wind-RLOF (Luna et al., 2018), both of which likely form an accretion disk around the compact object. In symbiotics with a WD, which are analogous to dCs, this accretion disk results in X-ray emission, with thermal bremsstrahlung models of $\sim$ 100 MK (Chernyakova et al., 2005; Tueller et al., 2005; Mukai et al., 2007; Smith et al., 2008; Kennea et al., 2009; Luna et al., 2013, 2018; Danehkar et al., 2021), compared to the approximate $\sim$ 10 MK found for the dCs with X-ray detections.

This supports the conclusion that the observed X-ray emission in dCs is indeed from coronal activity and not from accretion onto the WD companion.

The question remains, though, of how the initial properties of both the binary and the individual stars affect the formation of dCs. The evolution of the TP-AGB star, and the subsequent third dredge-up events, are affected by both the initial mass and metallicity of the star (Kalirai et al., 2014); this includes the final C/O of the TP-AGB envelope, controlling the C budget available to enhance the proto-dC. If the initial orbital period is too short, the system risks entering a CE phase either during the red giant branch or during the AGB phase before the third dredge-up can enhance the AGB to C/O$>$ 1. If the initial orbital period is too long, then the mass transfer may only take place via BHL accretion, or wind-RLOF may not effectively shrink the orbit to begin a CE, which would then cause the binary to spiral into the observed short periods. Therefore, the initial orbital and stellar properties that can result in a dC, and more strictly short period dCs, must inhabit a parameter space more stringent than traditional (C/O $<$ 1) WD+MS PCEBs, although they remain unknown.

Roulston et al. (2021) examined whether main-sequence companions to TP-AGB stars can accrete enough mass during the CE phase to form dCs. They found that the CE efficiency must be low to account for the known short-period orbits of dCs, which is consistent with the more well-known normal (C/O $<$ 1) WD+MS PCEBs (Zorotovic et al., 2010; Toonen & Nelemans, 2013; Camacho et al., 2014). Furthermore, they also found that dCs cannot accrete enough carbon-rich material during the CE phase, at least on the approximately 100 yr CE timescale assumed. They suggest that the dCs must accrete enough carbon-rich material before the CE phase, but after the third dredge-up has polluted the AGB companion, via wind-RLOF(Mohamed &

Podsiadlowski, 2007). In wind-RLOF, the primary (in the case of dCs, this would be a TP-AGB star) does not completely fill its Roche-Lobe, and the primary wind is focused in the orbital plane towards the secondary star (the proto-dC). This results in accretion rates that can be significantly higher than those in the BHL prescription, in some cases as high as 50% (Abate et al., 2013; Saladino et al., 2018, 2019; Saladino & Pols, 2019). It has also been shown that wind-RLOF can efficiently tighten the orbit (Saladino et al., 2018; Chen et al., 2018), driving these systems toward the short periods that have been found for dCs.

The wind-RLOF formalism for forming dCs requires a balance of initial orbital period, progenitor TP-AGB mass and metallicity, and progenitor dC mass and metallicity (and likely other parameters as well). It has been suggested that dCs may be predominantly found in low metallicity populations, as the amount of carbon excess needed to be accreted to make C/O$>$ 1 is less in a low metallicity star. The prototype dC G77-61 is extremely metal deficient with [Fe/H]~ -4 (Plez & Cohen, 2005). The mass of the dC progenitor (and C/O of the accreted mass) will also change how much material must be accreted. Miszalski et al. (2013) estimated that to shift a secondary from $(\mathrm{C/O})_i \sim 1/3$ to $(\mathrm{C/O})_f > 1$ would require the accretion of $\Delta M_2 = 0.03 - 0.35\,\mathrm{M}_\odot$ for a secondary with a mass $M_2 = 1.0 - 0.4\,\mathrm{M}_\odot$. The TP-AGB phase can last from 1 Myr up to 3.5 Myr (Kalirai et al., 2014), while the C-AGB phase itself only lasts up to ~ 0.42 Myr for an initial mass of $2.60\,\mathrm{M}_\odot$. Mass transfer to the dC must happen during this short time, which supports the wind-RLOF scenario, as a dC may accrete $0.35\,\mathrm{M}_\odot$ in only 10^3–10^6 yrs (for the above AGB mass-loss rates of 10^{-7}–$10^{-5}\,\mathrm{M}_\odot\,\mathrm{yr}^{-1}$, Höfner & Olofsson 2018) via wind-RLOF with accretion efficiencies as high as $\sim$ 50% (Abate et al., 2013).

Systems in which the dC has not experienced a CE phase (such as the dCs with

orbital periods of a year or more (Harris et al., 2018), may be the best candidates yet for testing if the accretion of carbon-rich material can cause the rejuvenation of dCs via spin-up to short rotation periods. Additionally, future simulations of wind-RLOF and CEE in progenitor dC systems, coupled with the observed dC space density and fraction of dCs with short orbital periods, may allow the first insight into the initial conditions needed for dC formation.

4.6 Summary

In this chapter, I analyzed a sample of *Chandra* observations of the five nearest dCs. From these, I detected X-ray emissions in two dCs. These two dCs also are the only ones with detected photometric variability and periods, linking the X-ray emission to dC rotation. I fit models to the X-ray spectra and found one dC with a peculiar model fit. The X-ray emission from dCs is consistent with rapid rotation. From the analysis in this chapter, I was able to determine the following:

1. X-ray emission is detected in two out of the five nearest dCs. For these two, the model plasma temperatures are consistent with that expected from other fast-rotating stars.

2. The dC X-ray emission is in the saturated regime suggesting (and confirmed with photometric light curves) that the X-ray emission in dCs is indeed connected to the dC's rotation period.

3. The dC J0435 has a peculiar X-ray spectrum, which is fit with a higher temperature of 14.2 MK, shows an intervening column density of $\mathrm{N}_H = 1.77 \times 10^{22}\,\mathrm{cm}^{-2}$. This is three orders of magnitude higher than expected at its Galactic position. As the SED shows no signs of a near-IR dust excess, this material is expected to

be in gaseous form and may be the remains of the AGB envelope ejection of the common envelope. Future observations and modeling are needed to constrain this system further.

4. The discovery of many short orbital period dCs in chapter 3 (Roulston et al., 2021) complicates the confirmation of dC spin-up. As these short-period dCs are likely tidally locked, it cannot be determined in those systems if the dC was spun-up before the tidal locking. However, this leads to the suggestion of observing a sample of known *wide* orbit dCs to check for spin-up in systems that are likely *not* tidally locked.

Chapter 5

Empirical Spectral Templates for Dwarf Carbon Stars and DA White Dwarfs

In this chapter, I describe the creation of optical spectral templates for dCs and DA WDs. These templates are built from the co-addition of SDSS spectra and are used to extend the PyHammer (Kesseli et al., 2017) classification program. I break the dCs into three classes based on optical colors and spectral shape, corresponding to classes that overlap with the normal (C/O $<$ 1) GKM stars. The contents of this chapter have been published in Roulston et al. (2020).

5.1 Motivation

Spectroscopy is a cornerstone of modern astronomy. Our understanding of the composition of stars, molecular clouds, nebulae, and exoplanetary atmospheres is determined via spectroscopy. Spectroscopy is used to search for and characterize binary companions and exoplanets, study the environments around stars and galaxies, and map the distances to galaxies and quasars.

Stellar spectroscopy allows for the measurement of stellar RVs, key for the study of galactic archaeology and evolution, as well as for the study of binary stellar systems and their evolution. Modern spectroscopic instruments and telescopes can determine RVs from the tug of exoplanets orbiting other stars. In the case of double-lined (spa-

tially unresolved) spectroscopic binaries (SB2), spectroscopy can reveal not only the presence of a binary system but information on its individual components. Accurate and rapid stellar classification is crucial to extract physics from stellar spectroscopy, especially in the era of large surveys.

The current spectral classification system, the Harvard system, classifies stars into letter classes that follow a temperature scale. The current classes of O, B, A, F, G, K, M, L, T, and Y represent stars and brown dwarfs across the stellar temperature range. O stars have the highest temperatures found in stars, and the M, L, T, and Y-dwarfs are the coolest (and most abundant, see Bochanski et al. 2010) spectral types that span the change from stars to brown dwarfs. While the majority of stars fall into these types, there are a few other spectral types commonly found in larger surveys, including the carbon (C) and white dwarf (WD) stars. The expanded Morgan-Keenan system (Morgan et al., 1943) adds additional luminosity (i.e. giant, dwarf, sub-dwarf) classes to the spectral typing scheme.

In recent years, there have been numerous implementations of automated spectral typing algorithms and software. These have included principal component analysis of large spectroscopic surveys like the SDSS (Blanton et al., 2017; McGurk et al., 2010), neural networks (Singh et al., 1998; Sharma et al., 2020), fitting of synthetic spectra from model atmospheres, and comparisons to spectral lines in stellar templates like PyHammer (Kesseli et al., 2017).

These automatic spectral typing methods have come about as a direct need of current and future large spectroscopic survey campaigns like SDSS and LAMOST (Cui et al., 2012). These surveys have already produced spectra for millions of stars, and with the beginning of the SDSS-V (Kollmeier et al., 2017), millions more will be observed with repeat, time-domain spectroscopy. These surveys represent an enormous,

only partly-exploited, resource for astronomy. With the coming of age of time-domain astronomy and large scale, all-sky photometric surveys, like ZTF (Bellm et al., 2019; Masci et al., 2019; Graham et al., 2019) and the Rubin Observatory Legacy Survey of Space and Time (LSST; Ivezić et al. 2019), the need for efficient and accurate stellar spectral typing is only going to become more pressing.

In addition to large spectroscopic surveys, further advances are needed to spectrally type binary stars, particularly close interacting binary stars. Recent surveys have shown that almost half of solar-type stars are in multiple systems (Raghavan et al., 2010; Moe & Di Stefano, 2017). Higher multiplicity can be found for earlier-type stars, while later-type stars are found to have a lower multiplicity - near 27% for M-dwarfs (Winters et al., 2019). Many of these systems are spatially unresolved and therefore undetected. However, the spectrum contains the light from both components and can tell us information about each one. In some cases, these components are of a sufficiently different spectral type that the spectrum is visually striking as an SB2 (e.g. M+WD binaries). However, the majority of SB2 components are in spectral types that are closer together in the MK system (e.g. G+K). While there have been advances in 'disentangling' SB2 spectra (Sablowski & Weber, 2017; Sablowski et al., 2019), these methods have generally relied on high resolution, high S/N, and multi-epoch spectra. These high-quality spectra require significant dedicated telescope time.

Motivation for this work came from the combination of a large-scale spectroscopic survey with a large fraction of stars being possible binary systems. The SDSS-IV's Time Domain Spectroscopic Survey (TDSS; Morganson et al., 2015; Ruan et al., 2016; MacLeod et al., 2018a, Anderson et al. 2022 in prep.) is a large spectral survey designed to collect optical spectra for a large sample of variable objects. The TDSS

observed optical spectra for approximately 81,000 variable sources (quasars and stars) selected based on being spatially unresolved in SDSS imaging and photometrically variable, without further regard, e.g., for color or type of variability (Anderson et al. 2020, in prep.). One of the TDSS's main goals is the study of variable stars with a combination of spectroscopy and photometry. Approximately half of the periodic stellar systems in this sample are likely to be binaries but do not show clear eclipses. The potential for spectroscopic detection of these binaries and characterization of their properties motivates the work detailed here.

Here I present an upgraded version of PyHammer, a Python spectral typing suite. PyHammer has the advantage of needing only a single epoch of spectroscopy to perform spectral typing, including the new SB2 typing abilities detailed here. I also present a new library of empirically-derived, luminosity-normalized spectral templates. These luminosity spectra are used to create SB2 templates, which have also been added to PyHammer. This version has also been extended to include single carbon and DA white dwarf stars.

5.2 PyHammer

5.2.1 PyHammer v1.0

PyHammer (Kesseli et al., 2017, https://github.com/BU-hammerTeam/PyHammer) is a Python based spectral typing suite that is based on the IDL program the Hammer (Covey et al., 2007, http://myweb.facstaff.wwu.edu/~coveyk/thehammer.html).

In v1.0 of PyHammer, spectral types were assigned by measuring spectral indices (similar to equivalent widths) for 34 atomic and molecular lines and comparing the measured indices to those of the templates. The best matching spectral type was selected as the one that minimized the χ^2 difference between spectral indices. Because

proper flux calibration across the full wavelength range of optical spectra can often be a significant challenge to achieve observationally, the use of spectral indices offers a distinct advantage for the accurate classification of typical spectra.

The templates used by PyHammer are for single stars spanning types: O, B, A, F, G, K, M, L. Each of these classes contains a variety of sub-types and metallicities that are simultaneously compared. All of these templates were created from the co-addition of SDSS optical spectra, as detailed in Kesseli et al. (2017).

The v1.0 PyHammer release extended the Hammer by including new templates to allow for spectral typing across different metallicities. It also provided a Python package that is easy to install and begin spectral typing without requiring IDL[1].

5.2.2 PyHammer v2.0: SB2

In this new release of PyHammer, available on GitHub[2], I add two new single star spectral types for main-sequence carbon stars (i.e. dwarf carbon, dC) and DA white dwarfs (WD), defining spectral indices for the C_2 and CH bandheads. The new dC stars span a range of broadband colors (and likely effective temperatures) from classic "G" to "M" type stars, while the WDs span a range of temperatures from 7000K to 100000K.

While the Balmer line spectral indices were included in PyHammer v1.0, I include a second set that spans wider Balmer line wavelength regions to help aid in the classification of the WDs.

PyHammer v2.0 now also has the ability to detect some combinations of spectroscopic binaries. The details of the SB2 templates are discussed in Section 5.5

[1] https://www.harrisgeospatial.com/Software-Technology/IDL
[2] https://github.com/BU-hammerTeam/PyHammer

Table 5.1: Properties of the new dC star templates. Colors are the unweighted average of SDSS and Gaia colors of the component spectra and were used to help separate stars into the three dC star template classes (along with visual inspection). The templates for dCG, dCK, dCM correspond to 'G', 'K', and 'M'-type dC stars respectively.

Template	$g-r$	$r-i$	$BP-RP$	N^{a}_{spec}	S/N
dCG	0.68	0.47	1.35	3	59
dCK	1.30	0.56	1.64	5	54
dCM	1.77	0.61	1.92	9	64

[a] Number of individual stellar spectra combined to create template.

5.3 Carbon Star and White Dwarf Templates

5.3.1 Carbon Star Templates

This release of PyHammer includes three new single star dC star templates. These new dC star templates are made using dC stars and were created in a similar method as the stellar library of Kesseli et al. (2017), involving the co-addition of individual spectra to make each sub-type.

The individual spectra used to make the dC star templates are from the SDSS sample of Green (2013). Green (2013) identified carbon stars by visual inspection of single-epoch SDSS spectra compiled from the union of (1) SDSS DR7 spectra (Abazajian et al., 2009) having strong cross-correlation coefficients with the SDSS carbon star templates, and with (2) SDSS spectra with a DR8 pipeline class of STAR and subclass including the word carbon (Aihara et al., 2011). The subsample with main-sequence luminosities (the dCs) was identified by their high proper motions.

The spectra used to make the new dC star templates were all selected from the SDSS DR16 (Ahumada et al., 2020), which includes a combination of SDSS-I/SDSS-II and SDSS-III/SDSS-IV spectroscopic data. SDSS-I/SDSS-II spectra were taken with

the legacy SDSS spectrograph, spanning a wavelength range of 3900 – 9100Å with a resolution of $R \sim 2000$. The newer eBOSS spectrograph (Smee et al., 2013) used in SDSS-III/SDSS-IV covers the 3600 – 10400Å range at a resolution of $R \sim 2500$.

From the Green (2013) dC star sample, I made a series of quality cuts as follows: (1) SDSS $15.0 < r < 17.0$ mag to ensure the SDSS sources are neither saturated nor have large uncertainties (Fukugita et al., 1996) (2) average S/N > 5 for the SDSS spectrum (3) Gaia DR2 (Gaia Collaboration et al., 2018) match within $2''$ (4) Gaia DR2 distance (Bailer-Jones et al., 2018) S/N > 5[3] (5) removed any dCs known to be in binaries with a WD (i.e. those with evident DA/dC composite spectra Heber et al. 1993; Liebert et al. 1994; Green 2013; Si et al. 2014) (6) removed any stars marked as giant in Green (2013).

After these cuts, I visually inspected each individual spectrum and removed those with bad flux regions and artifacts, which can happen due to background contamination, errors during the pipeline reduction, or fiber not being correctly placed. During this visual inspection, the "type" of dC star was noted (i.e., going progressively redder from 'G' to 'K' to 'M'-types) based on the continuum shape and strength of the CN bands.

I then placed the remaining dC stars into three groups based on the 'type' given during the visual inspection. Then using the average SDSS colors of $g - r$, $r - i$ and Gaia $BP - RP$ I removed any sources that fell outside of the color locus for a given template. The breakdown of these colors can be found in Table 5.3.1. The resulting templates (dubbed dCG, dCK, dCM) correspond approximately by color to 'G', 'K', 'M'-types, and were made from the co-addition of 3, 5, and 9 C star spectra

[3]The original cut of on parallax ($\varpi/\varpi_{\rm error} > 5$) did not translate to a distance S/N > 5 for all objects. The cut on the distance S/N ensures however that parallax and distance both have a S/N > 5.

respectively.

This co-addition follows the same method as used in Kesseli et al. (2017) for the original PyHammer; creating a wavelength grid that is logarithmically spaced (with 5 km s^{-1} spacing), interpolating each component spectrum onto this grid, and then add all the components together. The resulting template is then normalized so that the flux at 8000Å is unity.

The new dC star templates are listed as [Fe/H] = 0.0, although their metallicity information is unknown. Both higher resolution spectra and well-tested model atmospheres would be needed, but are not yet available for dC stars.

The most striking features of dC stars are their prominent C_2 and CN bandheads. These can be seen in Figure 5.1 which shows the three new dC star PyHammer templates. This figure also shows the variety of the dC class. The C_2 and CN molecular bandheads are marked, as well as the Hα atomic line wavelength. These bandheads allow for accurate spectral typing, given that additional spectral indices are added to PyHammer. Details of these can be found in Section 5.3.3.

5.3.2 WD Templates

I have created new DA WD templates and added them to v2.0 of PyHammer. These WD templates were created using the same method as for the original single star PyHammer templates and new dC star templates. I used spectra from the Gentile Fusillo et al. (2019) WD sample, which used spectroscopically confirmed WDs from the SDSS to create selection criteria and color cuts to select WDs from Gaia DR2.

From this sample of 260000 high-confidence white dwarf candidates, I selected stars using the following quality cuts: (1) DA classification by Gentile Fusillo et al. (2019) (2) SDSS $15.0 < r < 17.0$ mag (3) an existing SDSS spectrum with (4) mean

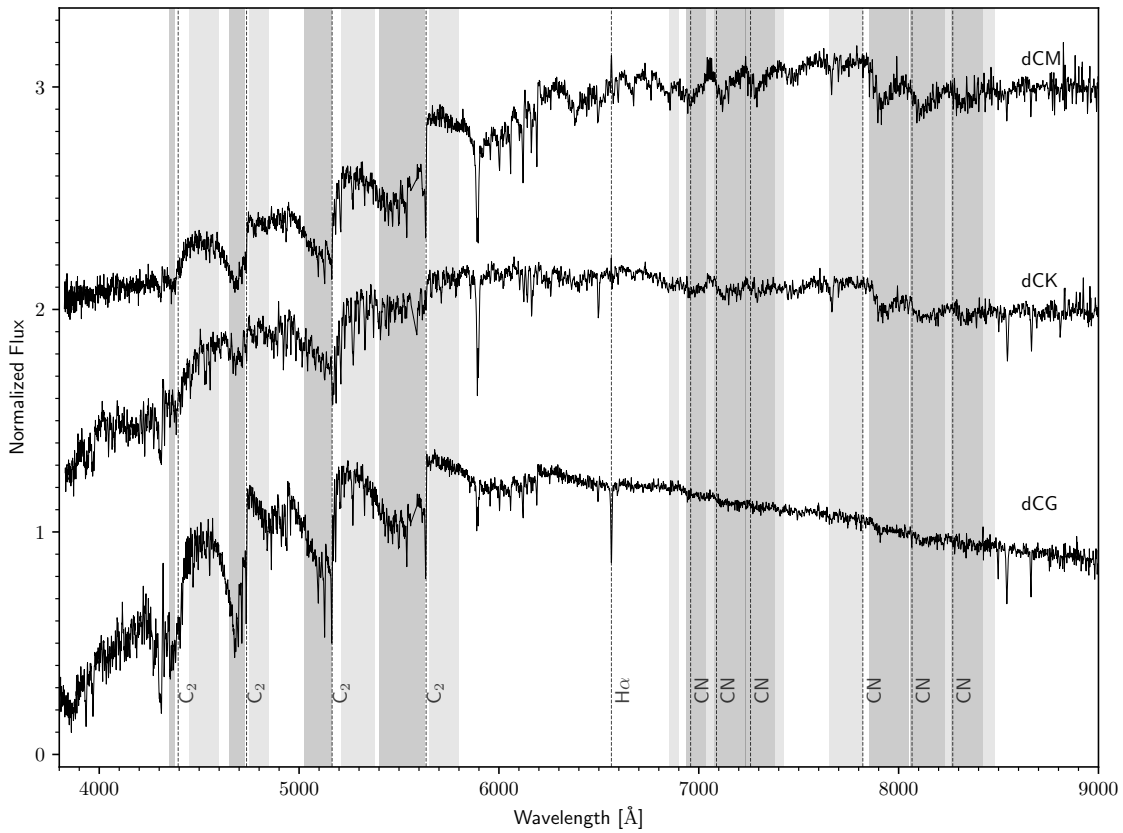

Figure 5.1: New PyHammer single star dC star templates. Each of these sub-type templates is averaged from a sample of luminosity-normalized single epoch SDSS spectra. The striking and prominent C_2 and CN bandheads are visible across the dC stars. These bandheads, as well as Hα, are marked and labeled with dashed lines. I also show the new spectral index regions used by PyHammer for automatic typing. There are 10 new dC star lines (4 C_2 and 6 CN), each consisting of a wavelength region within an absorption line or band, and a comparison 'continuum' region near the line region. The line regions and continuum regions are shown with dark and light gray shading, respectively. Each sub-type has been offset in flux for better visualization.

Table 5.2: Properties of the 10 new DA WD templates. These templates span temperatures from 7000K to 100000K and all have a S/N above 100. The reported colors are from SDSS and Gaia DR2 where the value is the unweighted average of all the spectra used to make each template.

Template	$T_{\rm eff.}$	$g-r$	$r-i$	$BP-RP$	N^{a}_{spec}	S/N
DA0.5	100 000	-0.53	-0.38	-0.55	6	102
DA1	50 000	-0.53	-0.37	-0.55	12	120
DA1.5	40 000	-0.51	-0.36	-0.51	18	175
DA2	30 000	-0.47	-0.34	-0.45	61	301
DA2.5	20 000	-0.39	-0.30	-0.30	100	421
DA3.5	15 000	-0.30	-0.25	-0.15	99	325
DA5	10 000	-0.14	-0.17	0.06	44	230
DA5.5	9 000	-0.02	-0.07	0.24	28	184
DA6.5	8 000	0.05	-0.02	0.35	20	154
DA7	7 000	0.19	0.05	0.52	16	164

[a] Number of individual stellar spectra combined to create template.

S/N > 5 (5) a Gaia DR2 distance (Bailer-Jones et al., 2018) S/N > 5. Similar to the dC star templates, after these selection cuts were made each individual spectrum was visually inspected to check for bad flux regions and artifacts, removing stars with bad regions. The remaining stars were grouped by temperature, taken from model fits by Gentile Fusillo et al. (2019), and co-added to create the 10 final DA templates, which were chosen to represent a reasonably-spaced temperature grid from 7000 to 100000 K. Each individual spectrum was assigned to the template nearest in temperature (e.g. the $T_{\rm eff.} = 10000K$ template is made of WDs with $9500K < T_{\rm eff.} \leq 12500$K).

The naming of the DA templates follows the system and effective-temperature indicator introduced by Sion et al. (1983), where I also follow the half-integer steps of Wesemael et al. (1993).

Table 5.3.2 shows the resulting set of DA templates, their temperatures, and the number of individual spectra averaged to make them. As with the new dC star templates, these new DA templates are listed as [Fe/H] = 0.0. Although this is not

valid for WDs, a metallicity value is required by the PyHammer software.

Figure 5.2 shows these new DA single star PyHammer templates, illustrating the variety of the DA temperatures included.

PyHammer v1.0 used Balmer line indices for spectral typing; however, the featureless spectra of the new DA WDs were almost always confused with A and F star templates in v1.0. To distinguish WDs, additional Balmer line indices of varying widths were added as well as additional fitting methods. Details of these can be found in Section 5.3.3.

5.3.3 PyHammer Spectral Indices

In addition to the new dC and DA WD templates, corresponding dC and DA line indices have been added to the list that PyHammer measures. The entire list, including new lines, is shown in Table 5.3.3. This table shows the line and the comparison wavelength regions for the spectral index numerator and denominator.

For the dC stars, I include the C_2 molecular bands in the blue and CN bands in the red. This allows for C bands to be calculated for either the bluer "G-type" carbon stars or the redder "M-types".

I have added a second set of Balmer line indices specifically for the DA WDs. These new "WD Balmer" line indices add a wider wavelength region to the previously included narrow Balmer line indices. Since the DA WD Balmer lines are broadened due to strong pressure broadening, this helps both with line detection, and to distinguish the DA WD indices from those of main-sequence stars with Balmer absorption. However, these wider Balmer line indices alone were not enough to consistently differentiate between DA WDs and hot stars of A and F types. Therefore, an additional line width measurement for the Hα line was added to the typing routine. This in-

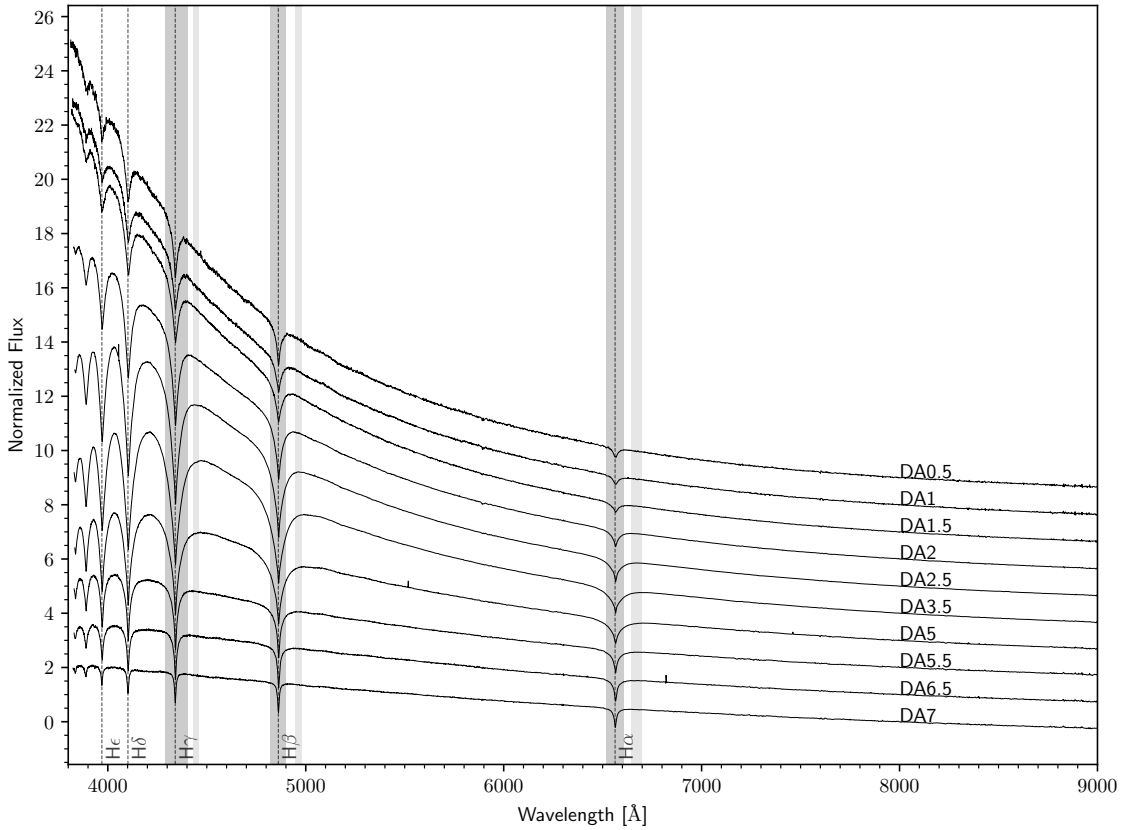

Figure 5.2: New PyHammer DA WD star templates. Each of these sub-type templates is averaged from a sample of luminosity-normalized single epoch SDSS spectra. Each sub-type has been offset in flux for better visualization. The Balmer lines are marked and labeled with dashed lines. I also show the new spectral index regions used by PyHammer for automated typing. Each spectral index consists of a line region and a continuum region near the line region. The line regions and continuum regions are shown with dark and light gray shading respectively.

volved fitting the Hα line with a Gaussian profile if the type is initially either A, F or DA WD. It then compares the fit width (σ) with that measured for most DA WDs; if the fit width is sufficiently large ($\sigma > 15$Å), PyHammer classifies the spectrum as a DA.

5.4 Luminosity Stellar Templates

To create single star templates that can then be combined to create realistic spectroscopic binary templates, I built a library of luminosity-normalized spectra[4], in units of erg s^{-1} Å^{-1}. To do this, I sought optical spectral libraries with precise flux calibrations that allow transformation into luminosity units using well-measured distances.

I created this by selecting O, B, A, and F main sequence stars from Pickles (1998), G, K, and M stars from the SDSS-IV MaStar program (Yan et al., 2019) program, dC stars from Green (2013), and DA WDs from Gentile Fusillo et al. (2019).

The MaStar survey uses fiber bundles, which can achieve much more accurate flux calibration than the normal SDSS survey. However, the MaStar sample (DR 16) lacks O, B, A, and F stars that meet the quality cuts. For those spectral types, I used the Pickles (1998) library. This library also is well flux-calibrated and has a similar resolution to SDSS and MaStar (R $\sim$ 2000).

There are no public digital libraries of precisely flux-calibrated C and WD star spectra. For these spectral types, I used the same libraries that I made their single star templates. The Gaia distance quality cuts ensure accurate distances to perform the flux to luminosity transformation.

The O, B, A, and F stars from Pickles (1998) have excellent relative flux calibra-

[4]Here luminosity-normalized refers to spectra in luminosity units, not to be confused with luminosity classes from the MK system.

Table 5.3: Spectral indices for v2.0 of PyHammer. For the indices that have two numerator regions the weight for each numerator is shown. Atomic and molecular lines are in order of increasing wavelength. Some Color region indices, separated from the atomic and molecular line indices at the bottom of the right set of indices, are also in increasing wavelength order.

Spectral Index	Numerator [Å]	Denominator [Å]	Spectral Index	Numerator [Å]	Denominator [Å]
Ca II K	3924.8 – 3944.8	3944.8 – 3954.8	CN λ7872	7850.0 – 8050.0	7650.0 – 7820.0
Caδ	4087.9 – 4117.9	4137.9 – 4177.2	VOλ7912	7902.2 – 7982.2	8102.2 – 8152.2
Ca I λ4217	4217.9 – 4237.9	4237.9 – 4257.2	CN λ8067	8059.0 – 8234.0	8234.0 – 8263.0
G band	4286.2 – 4316.2	4261.2 – 4286.2	Na I	8179.2 – 8203.2	8153.2 – 8177.2
WD Hγ	4290.0 – 4405.0	4430.0 – 4460.0	CN λ8270	8263.0 – 8423.0	8423.0 – 8481.0
Hγ	4333.7 – 4348.7	4356.2 – 4371.2	TiO8	8402.3 – 8417.3	8457.3 – 8472.3
C_2 λ4382	4350.0 – 4380.0	4450.0 – 4600.0	TiO λ8440	8442.3 – 8472.3	8402.3 – 8422.3
Fe I λ4383	4379.8 – 4389.8	4356.2 – 4371.2	Ca II λ8498	8485.3 – 8515.3	8515.3 – 8545.3
Fe Iλ4404	4401.0 – 4411.0	4416.0 – 4426.0	CrH-A	8582.4 – 8602.4	8623.4 – 8643.4
C_2 λ4737	4650.0 – 4730.0	4750.0 – 4850.0	Ca II λ8662	8652.4 – 8677.4	8627.4 – 8652.4
WD Hβ	4823.0 – 4900.0	4945.0 – 4980.0	Fe I λ8689	8686.4 – 8696.4	8666.4 – 8676.4
Hβ	4848.4 – 4878.3	4818.3 – 4848.4	FeH	9880.0 – 10000.0	9820.0 – 9860.0
C_2 λ5165	5028.0 – 5165.0	5210.0 – 5380.0	VOλ7445	7352.0 – 7402.0, 0.5625	7422.0 – 7472.1
Mg I	5154.1 – 5194.1	5101.4 – 5151.4		7512.1 – 7562.0, 0.4375	7422.0 – 7472.1
C_2 λ5636	5400.0 – 5630.0	5650.0 – 5800.0	VO-B	7862.2 – 7882.2, 0.5	7962.2 – 8002.2
NaD	5881.6 – 5906.6	5911.6 – 5936.6		8082.2 – 8102.2, 0.5	7962.2 – 8002.2
Ca I λ6162	6151.7 – 6176.7	6121.7 – 6146.7	Rb-B	7924.8 – 7934.8, 0.5	7944.8 – 7954.8
WD Hα	6519.0 – 6609.0	6645.0 – 6700.0		7964.8 – 7974.8, 0.5	7944.8 – 7954.8
Hα	6549.8 – 6579.8	6584.8 – 6614.8	Cs-A	8498.4 – 8508.4, 0.5	8518.4 – 8528.4
CaH2	6815.9 – 6847.9	7043.9 – 7047.9		8538.4 – 8548.4, 0.5	8518.4 – 8528.4
CN λ6926	6935.0 – 7035.0	6850.0 – 6900.0	Color region1	4160.0 – 4210.0	7480.0 – 7580.0
CaH3	6961.9 – 6991.9	7043.9 – 7047.9	Color region2	4550.0 – 4650.0	7480.0 – 7580.0
CN λ7088	7075.0 – 7233.0	7039.0 – 7075.0	Color region3	5700.0 – 5800.0	7480.0 – 7580.0
TiO5	7127.9 – 7136.9	7043.9 – 7047.9	Color region4	9100.0 – 9200.0	7480.0 – 7580.0
CN λ7259	7233.0 – 7382.0	7382.0 – 7425.0	Color region5	10100.0 – 10200.0	7480.0 – 7580.0
VOλ7434	7432.0 – 7472.0	7552.0 – 7572.0			

tions but are presented in normalized units where each spectrum is normalized to 1.0 at 5556Å. Since absolute magnitudes M_V are reported for each, I used the V band filter response function from Bessell (1990) to perform synthetic photometry, thereby finding the appropriate scale factor to convert these templates into luminosity units of erg s^{-1} $Å^{-1}$.

For the G, K, and M spectral types I matched each MaStar star to Gaia DR2 and selected the best spectrum for each spectral type and sub-type. This best spectrum was chosen as having the best combination of Gaia DR2 parallax S/N and Gaia G magnitude S/N. After selecting those with Gaia DR2 $\varpi/\varpi_{\rm err} > 10$, I then chose the best S/N spectrum in each sub-type bin. Then, using the Gaia DR2 distance, I converted these flux spectra into luminosity spectra in units of erg s^{-1} $Å^{-1}$.

For the dC and DA WD stars, I used a similar method to the GKM stars. However, since these objects are from the main SDSS-IV survey, some may have poorer absolute flux calibrations due e.g., to sub-optimal individual fiber placement or transmissivity. I mitigate this by averaging. I converted each of the individual spectra for each template into luminosity units using the Gaia DR2 distances. Then, I co-added and averaged to get an average luminosity spectrum for each spectral type.

Although PyHammer contains single L templates, I do not make L star spectral luminosity templates, because the L templates are constructed from very faint spectra ($r > 21$), outside the range of quality criteria. These L spectra likely have poor flux calibrations that are not suitable for transforming into luminosity units.

This luminosity-normalized digital spectral library allows for a variety of useful applications. The templates can be combined to create templates for spectroscopic binaries as described in the next section. Another important application is using these templates for flux calibration. Once an observed spectrum has been typed

using PyHammer, one can divide the appropriate template by the observed spectrum, fit with a low-order polynomial, and then multiply the polynomial by the observed spectrum to get a luminosity-normalized observed spectrum.

Figure 5.3 shows all of the luminosity spectra from the library that I then used to create spectroscopic binary templates. All of the luminosity spectra are in units of erg s^{-1} $Å^{-1}$ and have been smoothed by a boxcar of 10 pixels to aid in visualization.

This luminosity normalized spectral library can be found on Zenodo[5] in FITS format.

5.5 Spectroscopic Binary Templates

Using the luminosity library from Section 5.4, I was able to combine these spectra to create a library of main-sequence spectroscopic binary templates. This can be done by adding the component spectra together on a common wavelength axis to form a combined SB2 spectrum (the common wavelength axis I use is the PyHammer template wavelength grid which is logarithmically spaced between 3550Å and 10500Å with a spacing of 5 km s^{-1}).

Not all combinations of the main sequence luminosity templates make useful SB2 templates, as the more luminous stars easily overpower the faintest ones (e.g., an A5+M2 binary would be useless as the A star would be almost 10^3 times more luminous than the M star and no M star features would be visible).

To limit the combinations to those with some realistic hope of detection, I require that at least 20% of the pixels of the two constituent spectra be within 20% of the luminosity of each other.

For practical reasons of classification accuracy detailed in Section 5.6, I only build

[5] https://doi.org/10.5281/zenodo.3900328

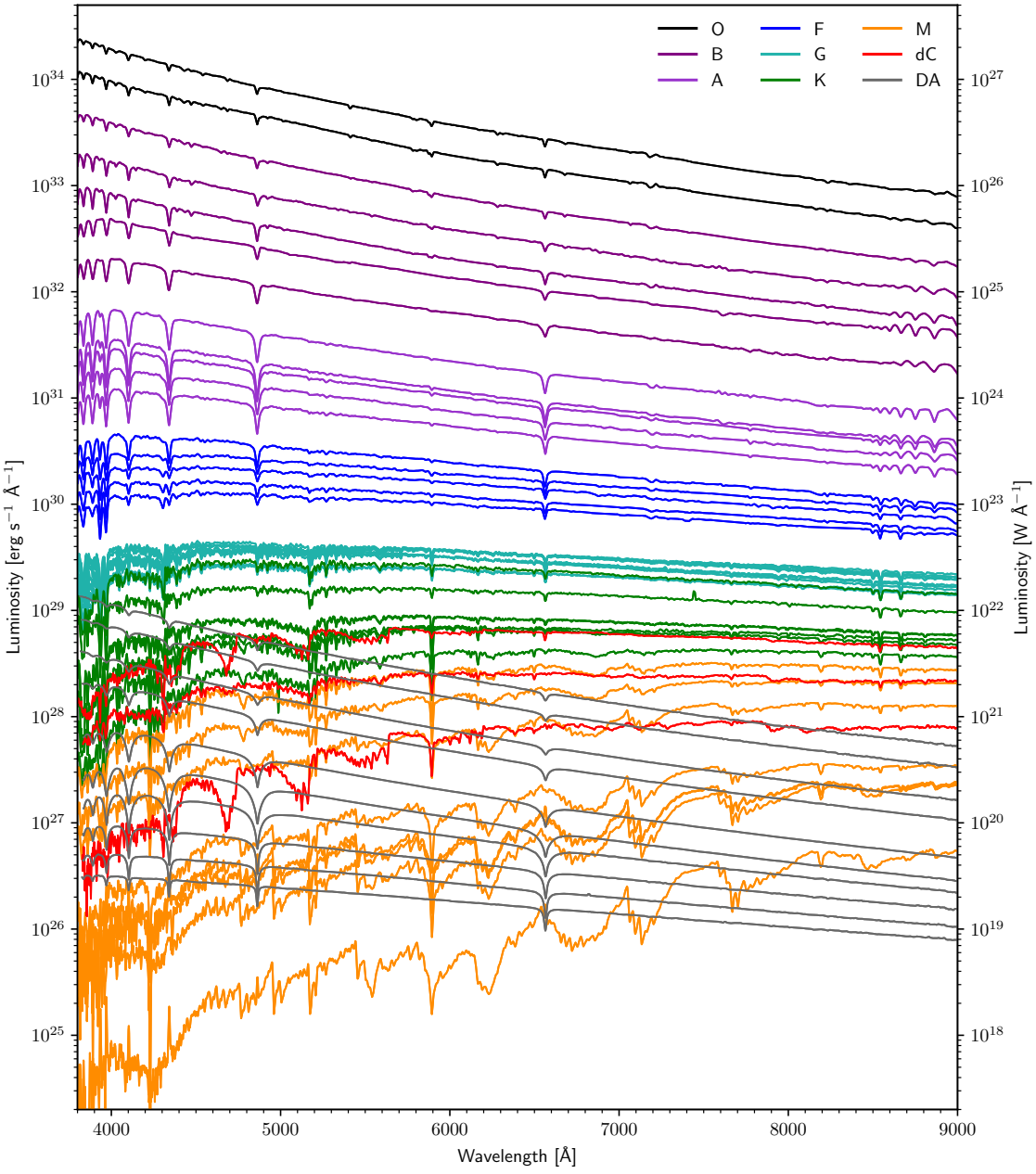

Figure 5.3: Luminosity-normalized stellar templates. These templates are made using digital stellar spectra from Pickles (1998) library, the MaStar library, Green (2013), and Gentile Fusillo et al. (2019). The MaStar, dC, and WD libraries all use flux-calibrated spectra and are converted to luminosity units using Gaia DR2 distances. The Pickles (1998) library is converted to luminosity units using reported M_V and synthetic photometry. Note that the luminosity axis is spaced logarithmically to clearly show the variation of stellar luminosty with spectral type.

SB2 combinations from constituents of different main spectral types (i.e. no A+A, F+F etc.). This results in the following combinations of main SB2 spectral types: A+F, F+G, F+K, G+K, G+dC, G+DA, K+M, K+dC, K+DA, M+dC, M+DA, dC+DA.

I have created and included these new SB2 templates to allow PyHammer the ability to spectral type SB2s based on a single epoch of optical spectroscopy. The SB2s generated and studied in the current work do not include any giant stars.

5.5.1 SB2 Radial Velocities

In addition to spectral typing, PyHammer has the ability to measure the RV of an input spectrum. As detailed in Kesseli et al. (2017), PyHammer uses a cross-correlation method across three wavelength regions. Kesseli et al. (2017) report that the original PyHammer has an RV accuracy of 7–10 km s^{-1} for mid-temperature and low-temperature stars and 10–15 km s^{-1} for high-temperature stars.

In the process of this work, I also considered adding the ability to PyHammer to fit the RV of each of the SB2 component spectra. This would involve using the luminosity spectral library to create SB2 composite templates on the fly, fitting the SB2 to the input spectrum with the RVs for both components as free parameters. This would be useful to find SB2s with components of similar spectral type (e.g. M2+M3 or F5+F6 etc.) where PyHammer v2.0 likely will classify the system as a single star. However, in such cases, there may often be widening or even separation of spectral lines due to the radial components of the orbital motion of the components, potentially allowing RV fitting to detect the RVs of both stars.

In practice, however, this proved difficult for a variety of reasons. Mainly, the SNR of most SDSS spectra is not high enough to allow for this robust of a fitting routine,

and the attempts at recovering simulated RV shifts were unsuccessful. After implementing and testing a few methods, the retrieved RV measurements for simulated SB2s have, so far, been unreliable and so I do not include this tool in PyHammer v2.0. Stars determined to be best fit by an SB2 template will have an RV reported by the software as NaN. The ability to calculate RVs for single stars however remains the same as with the original PyHammer (including for the new C and WD templates).

5.6 Accuracy

The initial SB2 templates included all templates that met the requirement that 20% of the pixels of the two constituent spectra be within 20% of the luminosity of each other, including SB2s wherein both the primary and secondary were of the same main spectral type (e.g. A2+A3, M2+M4).

However, after initial accuracy tests, I found that the classification accuracy rates for single stars dropped significantly when SB2s with the same main spectral type were included in PyHammer. For example, a single F5 star is unlikely to be misclassified as an F2+G2 SB2, but is quite likely to be misclassified as e.g., an F2+F5 SB2.

Figure 5.4 shows the classification accuracy for single stars being typed as single stars when including SB2s with the same main spectral type. The bottom panel shows the accuracy when including the same main spectral type SB2s and the top panel shows the accuracy rate when excluding the same main spectral type SB2s. This figure shows how strongly the single star accuracy rates are affected by including the same main spectral type SB2s.

One possible reason that these same main spectral type SB2s negatively affect the single star accuracy rates is that there are two nearly equivalent templates in terms of spectral indices. For example, when typing an F5 spectrum it could be equally

well-matched to an F5 template or an F4+F5 template. This results in single stars that have lower S/N or a noisy spectrum to be best typed by an SB2 with the same main spectral types.

For this reason, I do not include these same main spectral type SB2s templates in PyHammer v2.0, limiting SB2s to have different main spectral types. Classification accuracies discussed further in this section refer to the accuracy of PyHammer using only the SB2s which have different main spectral types.

However, all possible SB2 combinations meeting the 20% criteria outlined in Section 5.5 are included in the Zenodo library for completeness, whether or not they combine the same main spectral types. This includes some types, like dC+dC, which would be expected to be extremely rare in the cosmos for reasons of stellar evolution. As well as DA+DA types, which could be extremely interesting but difficult to detect with PyHammer.

I have tested the new SB2 templates for their accuracy[6] and their dependence on the input spectral S/N. I tested accuracies for all templates across a range of S/N. I did this by degrading each template by varying levels of noise. I created a Gaussian distribution for each pixel centered at the pixel's flux with the standard deviation given by an integer multiple of the template error at that pixel. I then used these distributions to draw new noisy spectra for integer multiples between 1σ and 50σ. Using PyHammer, I typed each noisy test spectrum at each degradation level. To better represent the accuracies for different use cases, I selected three "criteria" of classification accuracy to test.

The first criterion (criterion 0) is the least stringent, allowing any combination

[6]The accuracies detailed here are representative of SDSS spectra and may not reflect results for spectra of different resolution, wavelength coverage, relative flux calibration, or quality.

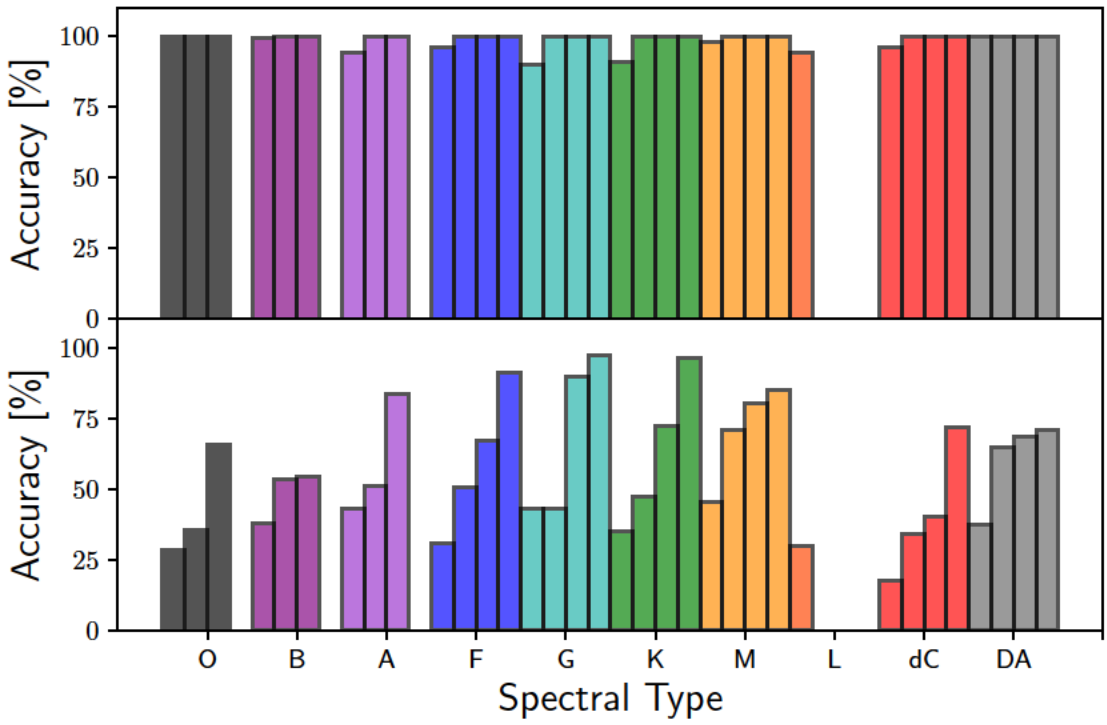

Figure 5.4: Classification accuracy for single stars for two different sets of SB2 combinations. The lower panel shows the accuracy rates for single stars typed as single stars when including same main spectral type SB2s (e.g. A+A, or G+G). The upper panel shows the accuracy rates for single stars typed as single stars when same main spectral type binaries are excluded from PyHammer. For each spectral type there are 4 bars for 4 S/N bins (left to right): S/N < 5, $5 \leq$ S/N < 10, $10 \leq$ S/N < 20, S/N ≥ 20. Note that not all spectral types have all S/N bins. Given the strong degradation in accuracy for single stars when allowing same main type SB2s, I exclude them from the software.

of sub-types as long as the two main spectral types are correct.[7] For example, an M2+DA3.5 would be correct even if labeled as an M1+DA7 because the main spectral types are correctly M and DA, but if it were labeled as K7+DA0.5, it would be counted as incorrect.

The second criterion (criterion 1) increases the requirements to count correct typing as only those SB2s classified by the code to be within one sub-type, in either or both of the components. In this case, an M2+DA3.5 would be counted correct if labeled as M2+DA2.5 (or M3+DA5, etc.), but would be incorrect if labeled as M2+DA6.

The third and most stringent criterion (criterion 2) counts the classification as correct if (and only if) the exact spectral types and sub-types for both components of the SB2 are correct. An example is an M2+DA3.5 would be classified correct only if labeled as M2+DA3.5; if labeled as M2+DA2.5, it would be incorrect.

Figure 5.5 shows the accuracy for each of the SB2 groups in PyHammer 2.0. Each of the panels shows the accuracy for one of the 6 possible primary spectral types (A, F, G, K, M, dC). Each panel then shows the accuracies for the possible combinations of secondary types (e.g. A+F, or dC+DA). Each primary+secondary combination has 4 bars for 4 S/N bins (left to right): S/N < 5, $5 \leq$ S/N < 10, $10 \leq$ S/N < 20, S/N > 20. Each bar then has 3 stacked components representing the previously described accuracy criteria (0, 1, or 2). Criterion 0 is represented by the most transparent (single diagonal hatching), criterion 1 by the partially transparent (double diagonal hatching), and criterion 2 by the solid color (no hatching) bars.

From Figure 5.5, I see that PyHammer's accuracy with SB2 stars is dependent

[7] Accuracy criterion 0 may be imprecise because it has discontinuous jumps at spectral type boundaries. For example, an F9+G9 classified as F9+K0 would be incorrect, even though a G9 is just one sub-type away from K0. However, this affects only a small percentage of the SB2 combinations.

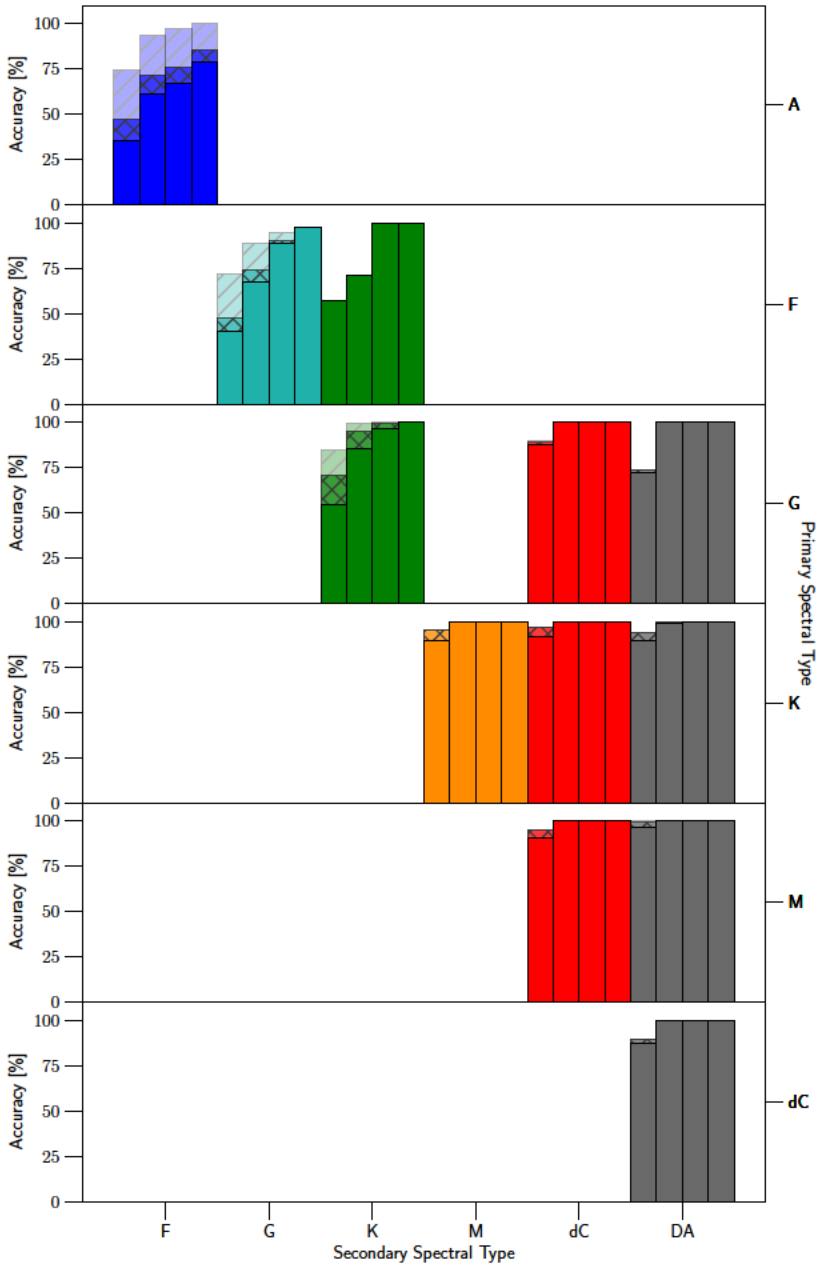

Figure 5.5: SB2 accuracy based on sub-type, S/N, and accuracy criteria. Each primary+secondary combination has 4 bars for 4 S/N bins (left to right): S/N < 5, $5 \leq$ S/N < 10, $10 \leq$ S/N < 20, S/N ≥ 20. Each bar then has 3 stacked components representing the previously described accuracy criteria (using criterion 0, 1, or 2). criterion 0 is represented by the most transparent bars (single diagonal hatching), criterion 1 by the middle transparent bars (double diagonal hatching), and criterion 2 by solid color bars (no hatching).

both on the input spectrum's S/N and on the spectral type combination. As expected, the lowest S/N has the lowest accuracy, which holds across all three "criteria" for counting accuracy. It can also be seen that early-type stellar combinations (i.e. A+F, F+G, F+K) tend to be less reliable. This is expected, as the early types of A and F are spectrally similar, with the main features being the Balmer lines. In contrast, late-type combinations (e.g. G+dC, K+M, M+dC, etc.) are much more - in some cases nearly 100% - accurate. This is likely due to the strong difference in visible atomic and molecular lines and bands within these spectral types (e.g. TiO bands in M dwarfs, and CN, CH, and C_2 bands in dC stars). PyHammer is particularly good at identifying binaries of late-type stars with a DA companion (i.e. G+DA, K+DA, M+DA, C+DA) due to the strong WD Balmer lines in the blue with strong late-type stellar features in the red. These types are all nearly 100% accurate across all S/N bins and accuracy criteria.

Figure 5.6 shows the accuracy for specific SB2 combinations. These accuracies are for criterion 0 (main types correct) and are an average of the degraded test spectra for that SB2 type that fall within the given S/N range. The figure shows two S/N ranges, with the $1.8 < S/N < 5$ bin given above the diagonal in the upper triangle, and the $5 < S/N < 15$ bin given below the diagonal in the lower triangle. This figure shows again that late-type combinations and those combinations with a DA WD component tend to be the most accurate at low S/N. However, at higher S/N (above $\sim$10) most combinations are above 90% accurate in all three criteria of accuracy.

I also report the accuracy of PyHammer v2.0 in identifying between the single star and SB2 star templates. Table 5.6 shows these accuracy rates between the single star and SB2 star classes. These rates are calculated from the total average across all S/N and across all spectral types and SB2 combinations. Here, accurate typing

is counted whenever a single star is typed as a single star or an SB2 is typed as an SB2. All other combinations are counted as incorrect (i.e., a single star classified as an SB2 or an SB2 classified as a single star).

These accuracies give the rates at which, on average, it is expected that PyHammer mistypes between single and SB2 star templates. There is a dependence on both spectral type and S/N, with these misclassifications all occurring for S/N < 5 and 32% being for A or F types. Misclassifications of A and F types are again not surprising, as those classes are very similar with predominant Balmer lines only. With low S/N, it is hard for PyHammer to distinguish between a low S/N A star and an A+F SB2. Overall, as shown in Table 5.6, PyHammer has about 95% accuracy in correctly identifying between the single and SB2 star classes.

5.7 Updated PyHammer GUI

The graphical user interface (GUI) for PyHammer v2.0 is functionally similar to the GUI in v1.0 of PyHammer. I have made a few minor updates and included the new functionality needed for classification using the SB2 templates.

PyHammer uses a χ^2 method to compare the spectral indices of the input spectrum to that of the templates. PyHammer now shows and reports this raw "distance" measure on the GUI screen as LineDist to aid users when visually checking the classifications. Along with this statistic, I also report the residual between the chosen template and the input spectrum as well as the residual weighted by the errors. These allow the user to easily see the statistical change in the fit of each template in addition to a visual check.

There are now two additional sliders and a toggle for SB2 templates. The toggle

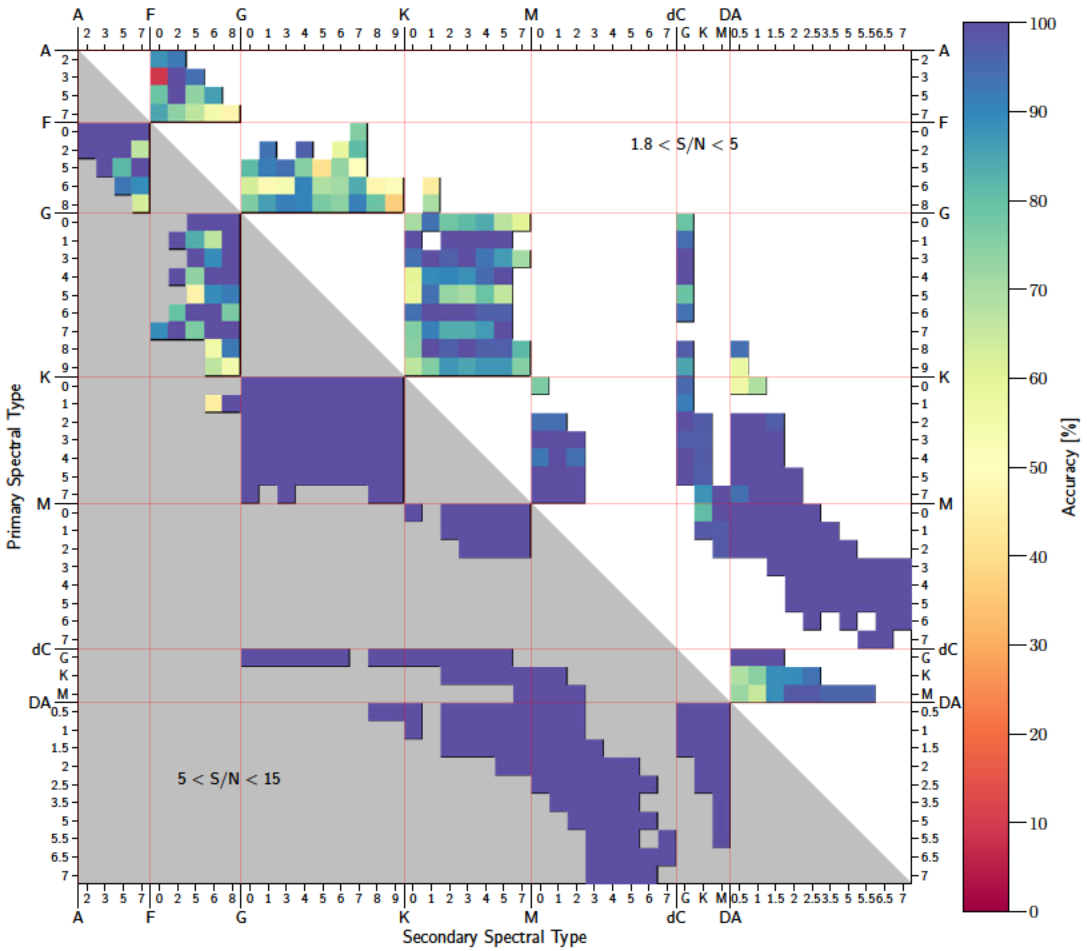

Figure 5.6: SB2 accuracy based on accuracy criterion 0 (i.e. only main-types need be correct). The upper triangle (white background) of the plot shows the accuracy rates for spectra with $1.8 < \mathrm{S/N} < 5$, and the lower triangle (gray background) plot shows accuracy rates for spectra with $5 < \mathrm{S/N} < 15$. All possible SB2 combinations are shown in this figure, with the primary type and sub-type labeled along the y-axis and the secondary type and sub-type along the x-axis. The percentage accuracy for a specific SB2 combination is derived from all the degraded test spectra for that SB2 type that fall within the given S/N bin.

Table 5.4: Accuracy and misclassification rates between the single and SB2 star classes. These rates are for S/N < 5 and only represent the accuracy and error rates between the single star and SB2 star template groups (i.e., this does not represent the total true accuracy rate because it only accounts for errors between the single and SB2 star classes). For each spectral type shown, the rate shown is the percentage of all test spectra in that primary-secondary type bin that were classified correctly as a SB2 for SB2 stars (and single for single stars).

SB2 Type	N_{spec}	Accuracy
A+F	424	90.3
F+G	769	90.8
F+K	55	94.6
G+K	1665	88.2
G+dC	253	94.5
G+DA	72	88.9
K+M	375	95.7
K+dC	433	98.4
K+DA	580	95.7
M+dC	203	95.1
M+DA	1686	100.0
dC+DA	708	90.4
SB2 Average	602	93.5
Single Type	.	.
O	187	100.0
B	421	99.5
A	1406	94.5
F	2140	96.4
G	2278	90.1
K	1653	91.0
M	1507	97.9
L	250	94.4
dC	137	96.4
DA	412	99.8
Single Average	1039	96.0

will turn on to include both single and SB2 templates, or off to include only single star templates. The additional sliders allow the user to select a secondary star's spectral type and sub-type based on the selected primary types. Only valid combinations from the list of SB2 templates are allowed, with unavailable options greyed out.

Figure 5.7 shows the new GUI in PyHammer v2.0 for the example of a dC+DA binary spectrum. The new secondary stellar-type sliders are visible, showing how the sliders limit the possible SB2 combinations.

5.8 Discussion

I have extended the PyHammer spectral typing software to include new carbon and DA white dwarf single star templates. These new templates were created in a similar method as the original PyHammer stellar templates via the co-addition of SDSS optical spectra. These new templates cover a range of effective temperatures across both dC and DA WD classes, providing spectral typing abilities for unique and important stellar types.

In addition, I have also created a new luminosity-normalized spectral library that consists of stars across the MK classification types. These luminosity templates are based on two libraries of accurately flux calibrated optical spectra and using the Gaia DR2 to convert to luminosity units of erg s^{-1} $Å^{-1}$. This luminosity library allowed us to create combinations of double-lined spectroscopic binary templates which I have also added to this v2.0 of PyHammer.

Fast and accurate automatic spectral typing is important for individual observers but also for large-scale all-sky surveys of today and the future. Surveys such as the SDSS-IV (Blanton et al., 2017) and the upcoming SDSS-V (Kollmeier et al., 2017) need accurate stellar spectral types in their reduction pipelines. These surveys

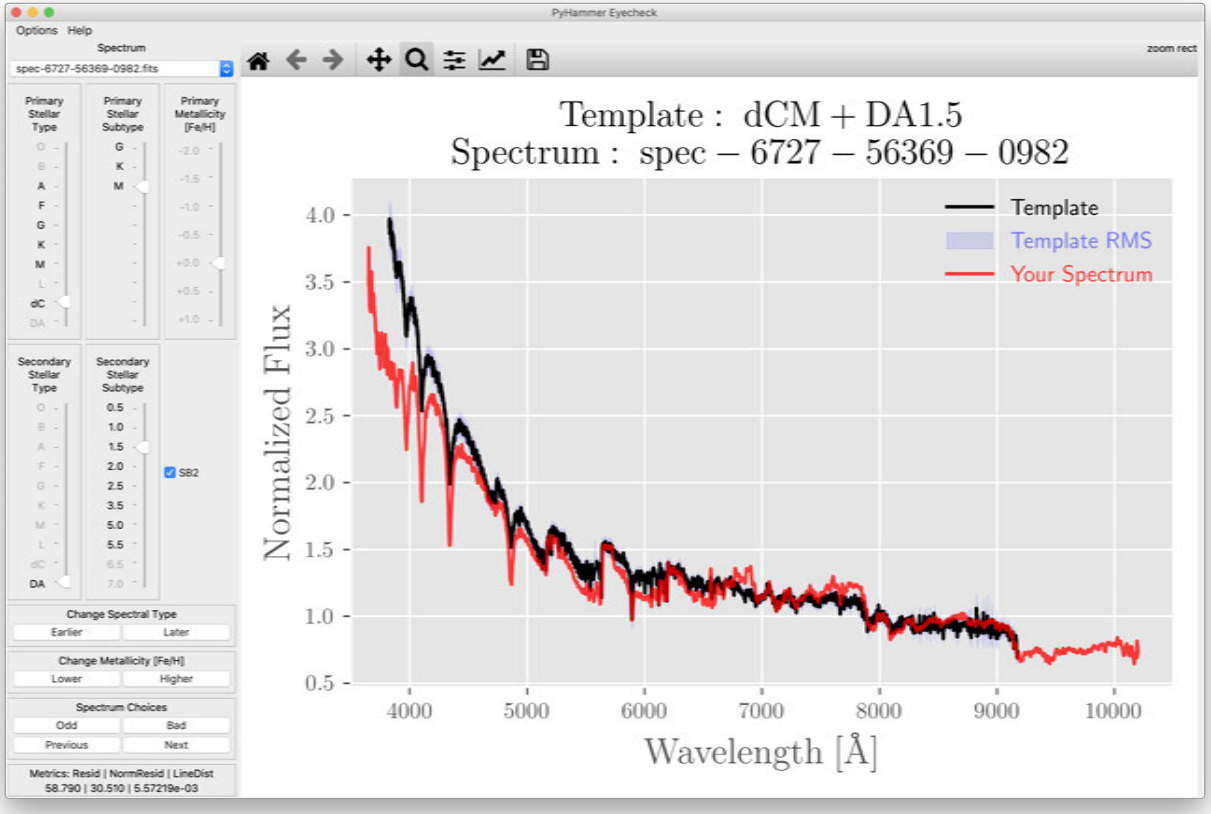

Figure 5.7: The GUI for PyHammer v2.0. This GUI is functionally the same as in the original PyHammer. The main new feature is that of the addition of SB2 options. Users now have the option to toggle on and off SB2 templates with a check button. This button enables and disables the SB2 sliders which allow the user to choose specific combinations of available SB2 binaries. This allows users to compare the fits of SB2 and single stars as well as to change the SB2 secondary types and sub-types to check for best fits.

often use stellar templates based on synthetic spectra and model atmospheres that require assumptions and simplifications. The stellar templates presented here allow for accurate spectral typing for situations in which accurate stellar models do not exist and would normally be left out of synthetic template libraries, such as dCs (Green, 2013).

PyHammer is also easily extendable to any spectral class in the future. The requirements are only that there exist enough correctly typed spectra to create a template and for which there are measurable spectral line features characteristic of that type. Examples of future PyHammer extensions could be CVs, T Tauri stars, or classes of galaxies. It is also possible that PyHammer could be extended to other wavelengths, for example, to encompass IR spectra. This type of extension would only require additional spectral indices in the desired wavelength ranges and would be useful for IR spectral surveys such as APOGEE (Majewski et al., 2017).

5.9 Summary

In this chapter, I have created a new set of empirical optical spectral templates for dCs and DA WDs. These templates are based on optical colors and spectral shape and detail the features unique to dCs: C_2, CN, and CH bands. In this chapter I did the following:

1. Created a set of new optical templates for dC spectra. These templates are split into three classes, based on optical colors, and correspond roughly to the same temperature range as the GKM stars.

2. Created a set of new optical templates for DA WD spectra. These templates are split into 10 classes, based on temperatures ranging from 7000K K to 100,000 K.

3. Created a set of spectroscopic binary (SB2) templates for a variety of spectral type combinations.

4. Extended the PyHammer program to include the new dC, DA WD, and SB2 templates. This new extension is capable of detecting double-lined binaries with a single epoch, given the spectral type are not of the same spectra type and the luminosity difference between the stars is reasonably small.

Chapter 6

Summary and Future Work

This dissertation provides the largest and most complete understanding of dC stars and their properties. Here, I summarize the answers to the questions posed at the beginning of this dissertation and place them in the context of future work.

6.1 Summary of Work

Questions 1, 2, and 3

1 What is the binary fraction of the dwarf carbon stars?

2 Are the orbital properties consistent with a single formation mechanism: carbon-enriched mass transfer?

3 What does the separation distribution imply for the mass transfer mechanisms that can form dwarf carbon stars, and in what systems can this occur?

These questions are addressed in Chapter 2 using spectroscopic data taken as part of the SDSS-IV's Time-Domain Spectroscopic Survey. Using multi-epoch spectroscopy, I measured the RV variations of an SDSS sample of dC stars. Through MCMC methods, the models were able to constrain the binary fraction to 95%, consistent with the expected binary formation pathway of dCs.

From these models, I was also able to construct the separation distribution of this dC population that best recreates the observed ΔRV distribution. I presented

the best parameters for two separation models: a single log-normal distribution and a bimodal mixture model of log-normal distributions. Both models result in close binary separation distributions with means less than 1 AU, corresponding to mean periods on the order of 1 year (varying depending on dC mass).

The sample contains a handful of objects with large ($\geq$ 100 km s^{-1}) ΔRV measurements that are indicative of close binary systems like those discussed in Chapter 3. These objects are prime targets for future spectroscopy to constrain orbital parameters, thereby better characterizing the separation distribution.

Question 4

4 What is the formation pathway for the extremely short period (P $<$ 1d) dCs?

Previously, there was a dearth of known orbital periods and solutions for dCs. This has made it hard to determine any conclusive evolutionary pathway for dCs. I addressed this question in Chapter 3 by searching ZTF light curves of a sample of 944 dCs for periodic signals. From this sample, I have found 34 dCs with signs of significant photometric variability, with 82% having P$<$ 2 d.

While previously only two dCs were known to have short periods, the dCs found in this chapter provide clear evidence that many dCs may experience a CE phase. I assume in these systems that the photometric variability is related to the orbital period via either tidally locked spot rotation or via irradiation effects. Indeed, due to the rapid expansion of the AGB radius during the late TP-AGB phase, it may be that most dCs experience CEE, but the ZTF cadence makes this type of search much more sensitive to short periods than to the longer periods of hundreds to thousands of days. The dCs with P$<$ 1 d must have experienced a substantial plunge-in while avoiding a merger.

Using binary population synthesis models, I showed that this observed sample of short-period dCs is not well-reconstructed by mass transfer during the CE phase alone. Accretion during the CE phase accounts for 2–3 orders of magnitude less mass than likely required to form a dC. Thus other mass transfer mechanisms, like BHL accretion, wind-RLOF, and RLOF, must play a role in the formation of dCs before the CE phase. This sets constraints on what initial periods can result in any observed dC system, as well as on these short-period dCs.

Progenitor systems with initially close orbits of a few hundred days will enter a CE phase at some point before the TP-AGB phase, likely during the red giant branch. These systems will never become dCs since they never experience the third dredge-up during the TP-AGB phase. Systems in very wide orbits of decades will also likely not become dCs as their wide separations keep the binary components from strongly interacting and will only experience inefficient BHL accretion.

The short-period dCs set a tighter constraint requiring that a CE phase begins after the dCs have formed, as I found that the CE phase itself cannot form a dC. Thus in these short-period dCs the dCs likely experience either wind-RLOF, RLOF, or both before entering the CE phase. Improved constraints on the distribution of dC orbits can help us understand the fraction that undergoes wind-RLOF only vs. wind-RLOF+RLOF+CE. Once this distribution is known, the given orbital periods can allow us to infer what mass transfer mechanisms are responsible for the dC formation. For example, the three dCs with years-long periods from Harris et al. (2018) all must have avoided RLOF and a CE phase; otherwise, we would observe them today at the same short 1 d periods as those found in Chapter 3. While it is possible these long period dCs may have only experienced BHL accretion, it is unlikely. The time frame to gain enough mass during BHL accretion only is typically longer than the time span

of the C star phase of a TP-AGB star. Thus we expect only wind-RLOF for this kind of years-long dC orbital period. The percentage of dCs that overall experience a CE phase is still unknown.

The periodic dCs in Chapter 3 provide a rich new sample to target for spectroscopic follow-up, as well as to study dC formation and properties. They also provide a new and exciting sample for testing other stellar astrophysics phenomena, such as CEE.

Question 5

5 Do the X-ray properties of dCs show they have increased activity from mass transfer spin-up, or rather from tidal locking in close orbits?

I addressed this question in Chapter 4 using *Chandra* observations of the five nearest dCs. From these observations, I detected X-ray emissions in two of the five observed. The two detected dCs had model fits that were consistent with X-ray emission of rapidly rotating stars, suggesting spin-up of dCs from their previous episodes of mass transfer.

However, the two dCs detected are also the only ones with detected photometric variability and periods, linking the X-ray emission to dC rotation, but provides a challenge in determining if accretion induced spin-up alone can rejuvenate dCs. Indeed, five of the six dCs observed in Green et al. (2019b) were found to have short-period orbits in Chapter 3, suggesting the rapid rotation is from tidal locking in these short-period systems.

To truly test for accretion induced spin-up, a sample of dCs that have *not* experienced a CE phase (such as the dCs with orbital periods of a year or more; Harris et al., 2018) may be the best candidates yet for testing if the accretion of carbon-rich

material can cause the rejuvenation of dCs via spin-up to short rotation periods.

Question 6

6 How do the spectral features of dCs change with effective temperature, and how does this affect their detection?

While there are no published dC model atmospheres, there is a large sample of dCs that have been observed in the SDSS. From these, I built three optical dC spectral templates with high signal-to-noise. Splitting the spectra into bins based on optical colors and spectral shapes results in the three templates matching in general to the normal ($C/O < 1$) GKM stars. The dCs span effective temperatures ranging from $\sim 5500\,K$ to $\sim 2500\,K$.

At the hotter (G-type) end, the dCs are characterized by strong and deep C_2 molecular bands in the blue between 4000 Å and 6000 Å with almost no other detectable C bands. In the middle range (K-type) all C bands appear to be weakened, but with identifiable CN bands in the red between 7000 Å and 9000 Å. In the coolest dCs (M-type), there are again strong C_2 lines, as well as impressive CN bands in the red. Given a wide wavelength coverage, such as that of the SDSS spectra, most dCs can be identified due to their unique C bands. However, the K-type dCs having weaker features are relatively harder to detect.

Future large optical spectroscopic surveys will be a prime use for these templates by using them to search for new dCs among the observed stellar populations. The SDSS-V (Kollmeier et al., 2017), WEAVE (Dalton et al., 2012), and 4MOST (de Jong et al., 2012) surveys all will observe millions of stars which may be searched for new dCs. As almost all dCs are in the northern sky (because the SDSS and LAMOST are, which those two surveys account for the source of the majority of dCs), the 4MOST

survey, which will observe the southern sky, is of particular interest. Indeed, 4MOST may be able to find hundreds of dCs that will be within the LSST field of view, allowing the search for numerous more short-period dCs like those in Chapter 3.

6.2 Future Work

The clearest extension of this work is to continue with follow-up observations of dCs. While the 34 new periods found in Chapter 3 are a welcome addition, a more extensive spectroscopic campaign is needed to confirm not only the photometric periods as orbital periods but also to find longer-period orbits. The release of *Gaia* DR3 and its astrometric binary catalog will hopefully contain an excellent sample of new, long-period dCs. The discovery of a sample of dCs in eclipsing binary systems would be particularly useful to obtain dynamical mass estimates crucial for atmospheric models of dCs and also for constraining the amount of mass accreted.

Extending past dCs themselves, the work in this dissertation provides a sample that may be used to constrain some of the most interesting and outstanding questions in stellar astrophysics today. Two of the more interesting cases are in constraining CEE and wind-RLOF.

As mentioned in Chapter 1, CEE is currently still a poorly understood process. However, it is needed to understand many of the most interesting astrophysical phenomena, such as gravitational wave sources, white-dwarf mergers, and cataclysmic variables. The foremost outstanding questions about CEE — what systems lead to a CE phase? how is the CE ejected? what determines if the CE phase leads to a merger? — are focused around some of the most critical phases. Clearly, there is a need to understand CEE in more detail, but something less talked about is also understanding CEE in a wider range of initial systems.

While there have been numerous simulations of CE phases that have tried to answer these questions, there has been a considerable lack of simulations involving AGB stars. During the AGB phase, the stellar radius can extend to many hundreds of that of the sun. If, during the TP-AGB phase, the surface abundance $C/O > 1$, these TP-AGB stars can have more extended radii relative to their O-rich counterparts ($\sim$800 $R_\odot$ compared to $\sim$250 $R_\odot$) and more massive winds up to $10^{-4}\,M_\odot\,yr^{-1}$, both of which are due to the increased opacity from the excess molecular carbon (Marigo et al., 2017). These enhanced radii correspond to a large range of initial orbital periods that can lead to a CE phase involving an AGB primary. These longer orbital periods and more massive winds cover a wider range of the initial parameter space that can lead to a CE phase and make binaries with TP-AGB stars an unexplored space of binary evolution and CEE.

The dCs in Chapter 3 represent an ideal sample of PCEBs for testing future simulations and models of CEE in binaries with a late AGB primary. Every other known PCEB sample (i.e., O-rich MS+WD binaries with periods roughly less than ten days) has the limiting factor that the progenitor system is unknown in the sense that the mass transfer history *prior* to the CE, and therefore by extension the initial orbital period, is unknown. In fact, most CE simulations start with the companion at the surface of the primary, explicitly skipping the initial loss of orbital stability that leads to the CE phase. This limits our ability to compare initial-to-final orbital period relations for most common PCEBs.

In the PCEB dCs, we have a unique advantage that we know, from their C-enhanced spectra, that they have experienced significant amounts of accretion. As I showed in Chapter 3, the CE phase alone can not account for this amount of accretion, and so we know the dCs must have experienced it prior to the CE phase. This, in

combination with the fact that the C star phase of an AGB is remarkably short (at most $\sim 0.5\,\mathrm{Myr}$, after which the AGB star evolves quickly into a post-AGB star and begins evolving toward the WD track; Kalirai et al., 2014), it is required that these dCs be enhanced *before* a CE phase but *after* the AGB surface composition becomes C-enhanced.

This constraint on the beginning of the CE phase is lacking in all other known PCEB samples; we simply do not know when the CE begins outside of loose constraints from single star core mass growth (assuming the CE was fully ejected, which is not always the case in current simulations, and the evolution of the primary truncated at that point). With the dC sample, we know the CE phase must begin during a roughly few hundred-thousand-year time span, with a relatively narrow primary mass range (C stars can only form from stars with masses between roughly $2.0\,\mathrm{M}_\odot$–$3.5\,\mathrm{M}_\odot$; Kalirai et al., 2014).

However, it is not just the CE phase itself that dCs can help constrain. There is a noticeable lack in simulations of binary systems with an AGB primary in the context of pre-CE evolution, with the few simulations only being done recently (Abate et al., 2018; Chen et al., 2018). With their large radii and slow (but massive) winds, AGB stars in binaries are prime candidates for studying the wind-RLOF mechanism where the wind is gravitationally focused into the orbital plane and onto the companion with efficiency much higher than the BHL accretion case. However, even among the few simulations with AGB primaries, there have been *no* simulations to date that use the more evolved TP-AGB stars that have experienced the third dredge-up, so they have atmospheric $\mathrm{C/O} > 1$.

The dCs represent a prime candidate target list for comparison of future simulations of wind-RLOF as we know their progenitor binary systems must have avoided

a CE phase during the red giant branch and during the AGB until after at minimum a few thermal pulses, suggesting wind-RLOF is the dominant mass transfer mechanism. Recent simulations have shown that the other C and *s*-process enhanced stars (e.g., CEMP, CH, Ba) are best modeled by formation via wind-RLOF from an AGB companion (Saladino et al., 2019; Saladino & Pols, 2019), further strengthening the connection to dCs.

In the case of dCs, we know they have been enhanced by C-rich mass from the envelope of a TP-AGB star. Future simulations (like those capable with the MESA suit; Paxton et al., 2011, 2013, 2015, 2018, 2019) will be able to model the accretion of typical TP-AGB C-rich envelope material onto low-mass main-sequence stars, while tracking envelope mixing, giving the needed amount of accreted mass as a function of the initial metallicity and mass of the main-sequence star. Since I have shown, in Chapter 3, that this mass cannot be accreted during the CE phase and must be prior, this mass was likely accreted via wind-RLOF, allowing for constraints on the efficacy and accuracy of past and future detailed simulations of wind-RLOF.

A few example outstanding questions that dCs may help in addressing include: How does the dust composition of an AGB wind affect the wind-RLOF mass transfer efficiencies? What is the stability of wind-RLOF through many thermal pulses during the TP-AGB phase? Under what conditions does wind-RLOF lead to a shortening of the orbital period?

6.3 Concluding Remarks

The dCs detailed throughout this dissertation are a fascinating class of chemically peculiar stars. They span a wide range of orbital periods from thousands of days all the way down to a few hours, with a fairly wide range of inferred masses from

$0.1\,M_\odot$ to up to $1.0\,M_\odot$. They show X-ray emission consistent with fast rotation and chromospheric activity, although the search for accretion induced spin-up requires avoiding the short orbital period dCs from Chapter 3 in a future program. Their C-enhanced atmospheres make dCs part of the larger family of chemically peculiar stars, including the CEMP, CH, and Ba stars, that all show C and *s*-process enhancements from previous mass transfer from an AGB companion. dCs are unique in that many of them (although unclear what true fraction) have short orbital periods implicating them as PCEBs, while the other chemically peculiar stars generally have long periods of hundreds to thousands of days (Jorissen et al., 2016; Abate et al., 2018). The imprints of this C-enhanced mass transfer can give us a sort of roadmap to their histories before the CE phase that brought some to such short orbits. dCs will be key in future studies to help constrain the uncertain physics of both CEE and wind-RLOF, thanks to the rather constrained timing of the onset of the CE phase.

While dCs are a relatively unknown class, with approximately only 27[1] refereed papers concerning them since their discovery in 1977, they represent an extremely important class of post-mass-transfer binaries that warrant further dedicated efforts of study. Understanding their formation, orbital properties, and stellar properties will be key in the community's endeavor to understand the physics of the multitude of binary interactions that lead to the most important astrophysical phenomena of today and the future.

[1]Dahn et al. (1977); Dearborn et al. (1986); Green et al. (1991); Heber et al. (1993); Warren et al. (1993); Liebert et al. (1994); Green & Margon (1994); Deutsch (1994); de Kool & Green (1995); MacConnell (1997); Harris et al. (1998); Lowrance et al. (2003); Plez & Cohen (2005); Miszalski et al. (2013); Green (2013); Si et al. (2014); Li et al. (2018); Margon et al. (2018); Harris et al. (2018); Farihi et al. (2018); Whitehouse et al. (2018); Roulston et al. (2019); Green et al. (2019b); Roulston et al. (2020); Whitehouse et al. (2021); Roulston et al. (2021, 2022)

List of Journal Abbreviations

A&A ..... Astronomy and Astrophysics

A&AS ..... Astronomy and Astrophysics Supplement Series

AJ ..... The Astronomical Journal

ApJ ..... The Astrophysical Journal

ApJL ..... The Astrophysical Journal Letters

ApJS ..... The Astrophysical Journal Supplement

ARA&A ..... Annual Review of Astronomy and Astrophysics

MNRAS ..... Monthly Notices of the Royal Astronomical Society

PASA ..... Publications of the Astronomical Society of Australia

PASJ ..... Publications of the Astronomical Society of Japan

PASP ..... Publications of the Astronomical Society of the Pacific

SoPh ..... Solar Physics

References

Abate, C., Pols, O. R., Izzard, R. G., Mohamed, S. S., & de Mink, S. E. 2013, A&A, 552, A26, doi: 10.1051/0004-6361/201220007

Abate, C., Pols, O. R., & Stancliffe, R. J. 2018, A&A, 620, A63, doi: 10.1051/0004-6361/201833780

Abazajian, K. N., Adelman-McCarthy, J. K., Agüeros, M. A., et al. 2009, ApJS, 182, 543, doi: 10.1088/0067-0049/182/2/543

Abolfathi, B., Aguado, D. S., Aguilar, G., et al. 2018, ApJS, 235, 42, doi: 10.3847/1538-4365/aa9e8a

Ahumada, R., Prieto, C. A., Almeida, A., et al. 2020, ApJS, 249, 3, doi: 10.3847/1538-4365/ab929e

Aihara, H., Allende Prieto, C., An, D., et al. 2011, ApJS, 193, 29, doi: 10.1088/0067-0049/193/2/29

Allard, F., Homeier, D., & Freytag, B. 2011, in Astronomical Society of the Pacific Conference Series, Vol. 448, 16th Cambridge Workshop on Cool Stars, Stellar Systems, and the Sun, ed. C. M. Johns-Krull, M. K. Browning, & A. A. West, 91. https://arxiv.org/abs/1011.5405

Allen, D. A. 1984, PASA, 5, 369

Amaro-Seoane, P., Audley, H., Babak, S., et al. 2017, arXiv e-prints, arXiv:1702.00786. https://arxiv.org/abs/1702.00786

Aoki, W., Beers, T. C., Christlieb, N., et al. 2007, ApJ, 655, 492, doi: 10.1086/509817

Ashley, R. P., Farihi, J., Marsh, T. R., Wilson, D. J., & Gänsicke, B. T. 2019, MNRAS, 484, 5362, doi: 10.1093/mnras/stz298

Asplund, M., Amarsi, A. M., & Grevesse, N. 2021, A&A, 653, A141, doi: 10.1051/0004-6361/202140445

Astropy Collaboration, Price-Whelan, A. M., Sipőcz, B. M., et al. 2018, AJ, 156, 123, doi: 10.3847/1538-3881/aabc4f

Badenes, C., & Maoz, D. 2012, ApJL, 749, L11, doi: 10.1088/2041-8205/749/1/L11

Badenes, C., Mazzola, C., Thompson, T. A., et al. 2018, ApJ, 854, 147, doi: 10.3847/1538-4357/aaa765

Bailer-Jones, C. A. L., Rybizki, J., Fouesneau, M., Demleitner, M., & Andrae, R. 2021, AJ, 161, 147, doi: 10.3847/1538-3881/abd806

Bailer-Jones, C. A. L., Rybizki, J., Fouesneau, M., Mantelet, G., & Andrae, R. 2018, AJ, 156, 58, doi: 10.3847/1538-3881/aacb21

Bédard, A., Bergeron, P., Brassard, P., & Fontaine, G. 2020, ApJ, 901, 93, doi: 10.3847/1538-4357/abafbe

Bellm, E. C., Kulkarni, S. R., Graham, M. J., et al. 2019, PASP, 131, 018002, doi: 10.1088/1538-3873/aaecbe

Bensby, T., Feltzing, S., Lundström, I., & Ilyin, I. 2005, A&A, 433, 185, doi: 10.1051/0004-6361:20040332

Bessell, M. S. 1990, PASP, 102, 1181, doi: 10.1086/132749

Bidelman, W. P., & Keenan, P. C. 1951, ApJ, 114, 473, doi: 10.1086/145488

Blanton, M. R., Bershady, M. A., Abolfathi, B., et al. 2017, AJ, 154, 28, doi: 10.3847/1538-3881/aa7567

Bochanski, J. J., Hawley, S. L., Covey, K. R., et al. 2010, AJ, 139, 2679, doi: 10.1088/0004-6256/139/6/2679

Boissier, S., & Prantzos, N. 1999, MNRAS, 307, 857, doi: 10.1046/j.1365-8711.1999.02699.x

Bondi, H., & Hoyle, F. 1944, MNRAS, 104, 273, doi: 10.1093/mnras/104.5.273

Bovy, J., Hogg, D. W., & Roweis, S. T. 2011, Annals of Applied Statistics, 5, 1657, doi: 10.1214/10-AOAS439

Camacho, J., Torres, S., García-Berro, E., et al. 2014, A&A, 566, A86, doi: 10.1051/0004-6361/201323052

Cardelli, J. A., Clayton, G. C., & Mathis, J. S. 1989, ApJ, 345, 245, doi: 10.1086/167900

Carney, B. W., Latham, D. W., & Laird, J. B. 1988, AJ, 96, 560, doi: 10.1086/114831

Chamandy, L., Blackman, E. G., Frank, A., Carroll-Nellenback, J., & Tu, Y. 2020, MNRAS, 495, 4028, doi: 10.1093/mnras/staa1273

Chamandy, L., Frank, A., Blackman, E. G., et al. 2018, MNRAS, 480, 1898, doi: 10.1093/mnras/sty1950

Chambers, K. C., Magnier, E. A., Metcalfe, N., et al. 2016, arXiv e-prints, arXiv:1612.05560. https://arxiv.org/abs/1612.05560

Chen, X., & Han, Z. 2008, MNRAS, 387, 1416, doi: 10.1111/j.1365-2966.2008.13334.x

Chen, X., Wang, S., Deng, L., et al. 2020, ApJS, 249, 18, doi: 10.3847/1538-4365/ab9cae

Chen, Z., Blackman, E. G., Nordhaus, J., Frank, A., & Carroll-Nellenback, J. 2018, MNRAS, 473, 747, doi: 10.1093/mnras/stx2335

Chernyakova, M., Courvoisier, T. J. L., Rodriguez, J., & Lutovinov, A. 2005, The Astronomer's Telegram, 519, 1

Chilingarian, I. 2020, in Astronomical Society of the Pacific Conference Series, Vol. 522, Astronomical Data Analysis Software and Systems XXVII, ed. P. Ballester, J. Ibsen, M. Solar, & K. Shortridge, 623

Christlieb, N., Green, P. J., Wisotzki, L., & Reimers, D. 2001, A&A, 375, 366, doi: 10.1051/0004-6361:20010814

Corradi, R. L. M., Sabin, L., Miszalski, B., et al. 2011, MNRAS, 410, 1349, doi: 10.1111/j.1365-2966.2010.17523.x

Covey, K. R., Ivezić, Ž., Schlegel, D., et al. 2007, AJ, 134, 2398, doi: 10.1086/522052

Cui, X.-Q., Zhao, Y.-H., Chu, Y.-Q., et al. 2012, Research in Astronomy and Astrophysics, 12, 1197, doi: 10.1088/1674-4527/12/9/003

Dahn, C. C., Liebert, J., Kron, R. G., Spinrad, H., & Hintzen, P. M. 1977, ApJ, 216, 757, doi: 10.1086/155518

Dalton, G., Trager, S. C., Abrams, D. C., et al. 2012, in Society of Photo-Optical Instrumentation Engineers (SPIE) Conference Series, Vol. 8446, Ground-based and Airborne Instrumentation for Astronomy IV, ed. I. S. McLean, S. K. Ramsay, & H. Takami, 84460P, doi: 10.1117/12.925950

Danehkar, A., Karovska, M., Drake, J. J., & Kashyap, V. L. 2021, MNRAS, 500, 4801, doi: 10.1093/mnras/staa3554

Davidsen, A., Malina, R., & Bowyer, S. 1976, ApJ, 203, 448, doi: 10.1086/154096

Dawson, K. S., Kneib, J.-P., Percival, W. J., et al. 2016, AJ, 151, 44, doi: 10.3847/0004-6256/151/2/44

de Jong, R. S., Bellido-Tirado, O., Chiappini, C., et al. 2012, in Society of Photo-Optical Instrumentation Engineers (SPIE) Conference Series, Vol. 8446, Ground-based and Airborne Instrumentation for Astronomy IV, ed. I. S. McLean, S. K. Ramsay, & H. Takami, 84460T, doi: 10.1117/12.926239

de Kool, M. 1990, ApJ, 358, 189, doi: 10.1086/168974

de Kool, M., & Green, P. J. 1995, ApJ, 449, 236, doi: 10.1086/176051

de Kool, M., van den Heuvel, E. P. J., & Pylyser, E. 1987, A&A, 183, 47

Dearborn, D. S. P., Liebert, J., Aaronson, M., et al. 1986, ApJ, 300, 314, doi: 10.1086/163805

Dell'Agli, F., Marini, E., D'Antona, F., et al. 2021, MNRAS, 502, L35, doi: 10.1093/mnrasl/slaa204

Deutsch, E. W. 1994, PASP, 106, 1134, doi: 10.1086/133489

Drake, A. J., Djorgovski, S. G., Mahabal, A., et al. 2009, ApJ, 696, 870, doi: 10.1088/0004-637X/696/1/870

Eggleton, P. P. 1983, ApJ, 268, 368, doi: 10.1086/160960

Eker, Z., Bakış, V., Bilir, S., et al. 2018, MNRAS, 479, 5491, doi: 10.1093/mnras/sty1834

El-Badry, K., Rix, H.-W., Ting, Y.-S., et al. 2018, MNRAS, 473, 5043, doi: 10.1093/mnras/stx2758

Escorza, A., Karinkuzhi, D., Jorissen, A., et al. 2019, A&A, 626, A128, doi: 10.1051/0004-6361/201935390

Fabricant, D., Cheimets, P., Caldwell, N., & Geary, J. 1998, PASP, 110, 79, doi: 10.1086/316111

Fabricant, D., Fata, R., Epps, H., et al. 2019, PASP, 131, 075004, doi: 10.1088/1538-3873/ab1d78

Farihi, J., Arendt, A. R., Machado, H. S., & Whitehouse, L. J. 2018, MNRAS, 477, 3801, doi: 10.1093/mnras/sty890

Farihi, J., Hoard, D. W., & Wachter, S. 2010, ApJS, 190, 275, doi: 10.1088/0067-0049/190/2/275

Filippazzo, J. C., Rice, E. L., Faherty, J., et al. 2015, ApJ, 810, 158, doi: 10.1088/0004-637X/810/2/158

Flewelling, H. A., Magnier, E. A., Chambers, K. C., et al. 2020, ApJS, 251, 7, doi: 10.3847/1538-4365/abb82d

Fontaine, G., Brassard, P., & Bergeron, P. 2001, PASP, 113, 409, doi: 10.1086/319535

Freeman, P., Doe, S., & Siemiginowska, A. 2001, in Society of Photo-Optical Instrumentation Engineers (SPIE) Conference Series, Vol. 4477, Astronomical Data Analysis, ed. J.-L. Starck & F. D. Murtagh, 76–87, doi: 10.1117/12.447161

Fukugita, M., Ichikawa, T., Gunn, J. E., et al. 1996, AJ, 111, 1748, doi: 10.1086/117915

Gaia Collaboration, Brown, A. G. A., Vallenari, A., et al. 2018, A&A, 616, A1, doi: 10.1051/0004-6361/201833051

—. 2021, A&A, 649, A1, doi: 10.1051/0004-6361/202039657

Garraffo, C., Drake, J. J., Alvarado-Gomez, J. D., Moschou, S. P., & Cohen, O. 2018, ApJ, 868, 60, doi: 10.3847/1538-4357/aae589

Gass, H. 1988, Sterne und Weltraum, 27, 147

Gentile Fusillo, N. P., Tremblay, P.-E., Gänsicke, B. T., et al. 2019, MNRAS, 482, 4570, doi: 10.1093/mnras/sty3016

Goodman, J., & Weare, J. 2010, Communications in Applied Mathematics and Computational Science, 5, 65, doi: 10.2140/camcos.2010.5.65

Gosnell, N. M., Leiner, E. M., Mathieu, R. D., et al. 2019, ApJ, 885, 45, doi: 10.3847/1538-4357/ab4273

Gosnell, N. M., Mathieu, R. D., Geller, A. M., et al. 2014, ApJL, 783, L8, doi: 10.1088/2041-8205/783/1/L8

Graham, M. J., Kulkarni, S. R., Bellm, E. C., et al. 2019, PASP, 131, 078001, doi: 10.1088/1538-3873/ab006c

Green, G. M. 2018, The Journal of Open Source Software, 3, 695, doi: 10.21105/joss.00695

Green, G. M., Schlafly, E., Zucker, C., Speagle, J. S., & Finkbeiner, D. 2019a, ApJ, 887, 93, doi: 10.3847/1538-4357/ab5362

Green, G. M., Schlafly, E. F., Finkbeiner, D., et al. 2018, MNRAS, 478, 651, doi: 10.1093/mnras/sty1008

Green, P. 2013, ApJ, 765, 12, doi: 10.1088/0004-637X/765/1/12

Green, P. J., & Margon, B. 1994, ApJ, 423, 723, doi: 10.1086/173851

Green, P. J., Margon, B., & MacConnell, D. J. 1991, ApJL, 380, L31, doi: 10.1086/186166

Green, P. J., Montez, R., Mazzoni, F., et al. 2019b, ApJ, 881, 49, doi: 10.3847/1538-4357/ab2bf4

Gregory, P. C., & Loredo, T. J. 1992, ApJ, 398, 146, doi: 10.1086/171844

Greiss, S., Gänsicke, B. T., Hermes, J. J., et al. 2014, MNRAS, 438, 3086, doi: 10.1093/mnras/stt2420

Gruendl, R. A., Chu, Y. H., Seale, J. P., et al. 2008, ApJL, 688, L9, doi: 10.1086/593979

Habing, H. J., & Olofsson, H. 2004, Asymptotic Giant Branch Stars (Springer), doi: 10.1007/978-1-4757-3876-6

Harris, H. C., Dahn, C. C., Walker, R. L., et al. 1998, ApJ, 502, 437, doi: 10.1086/305908

Harris, H. C., Dahn, C. C., Subasavage, J. P., et al. 2018, AJ, 155, 252, doi: 10.3847/1538-3881/aac100

Heber, U. 1986, A&A, 155, 33

Heber, U., Bade, N., Jordan, S., & Voges, W. 1993, A&A, 267, L31

Hermes, J. J., Montgomery, M. H., Bell, K. J., et al. 2015, ApJL, 810, L5, doi: 10.1088/2041-8205/810/1/L5

Höfner, S. 2015, in Astronomical Society of the Pacific Conference Series, Vol. 497, Why Galaxies Care about AGB Stars III: A Closer Look in Space and Time, ed. F. Kerschbaum, R. F. Wing, & J. Hron, 333. https://arxiv.org/abs/1505.07425

Höfner, S., & Olofsson, H. 2018, A&A Rv, 26, 1, doi: 10.1007/s00159-017-0106-5

Howard, W. S., Corbett, H., Law, N. M., et al. 2019, ApJ, 881, 9, doi: 10.3847/1538-4357/ab2767

Hoyle, F., & Lyttleton, R. A. 1939, Nature, 144, 1019, doi: 10.1038/1441019a0

Hurley, J. R., Tout, C. A., & Pols, O. R. 2002, MNRAS, 329, 897, doi: 10.1046/j.1365-8711.2002.05038.x

Iben, I., J. 1974, ARA&A, 12, 215, doi: 10.1146/annurev.aa.12.090174.001243

Iben, I., J., & Renzini, A. 1983, ARA&A, 21, 271, doi: 10.1146/annurev.aa.21.090183.001415

Iglesias-Marzoa, R., López-Morales, M., & Jesús Arévalo Morales, M. 2015, PASP, 127, 567, doi: 10.1086/682056

Igoshev, A. P., Perets, H. B., & Michaely, E. 2020, MNRAS, 494, 1448, doi: 10.1093/mnras/staa833

Ivanov, V. D., Rieke, M. J., Engelbracht, C. W., et al. 2004, ApJS, 151, 387, doi: 10.1086/381752

Ivanova, N., & Taam, R. E. 2003, ApJ, 599, 516, doi: 10.1086/379192

Ivanova, N., Justham, S., Chen, X., et al. 2013, A&A Rv, 21, 59, doi: 10.1007/s00159-013-0059-2

Ivezić, Ž., Kahn, S. M., Tyson, J. A., et al. 2019, ApJ, 873, 111, doi: 10.3847/1538-4357/ab042c

Jeffries, R. D., & Stevens, I. R. 1996, MNRAS, 279, 180, doi: 10.1093/mnras/279.1.180

Jorissen, A., Van Eck, S., Van Winckel, H., et al. 2016, A&A, 586, A158, doi: 10.1051/0004-6361/201526992

Kalirai, J. S., Marigo, P., & Tremblay, P.-E. 2014, ApJ, 782, 17, doi: 10.1088/0004-637X/782/1/17

Kansky, J., Chilingarian, I., Fabricant, D., et al. 2019, Binospec: Data reduction pipeline for the Binospec imaging spectrograph. http://ascl.net/1905.004

Kennea, J. A., Mukai, K., Sokoloski, J. L., et al. 2009, ApJ, 701, 1992, doi: 10.1088/0004-637X/701/2/1992

Kepler, S. O., Kleinman, S. J., Nitta, A., et al. 2007, MNRAS, 375, 1315, doi: 10.1111/j.1365-2966.2006.11388.x

Kesseli, A. Y., Muirhead, P. S., Mann, A. W., & Mace, G. 2018, AJ, 155, 225, doi: 10.3847/1538-3881/aabccb

Kesseli, A. Y., West, A. A., Veyette, M., et al. 2017, ApJS, 230, 16, doi: 10.3847/1538-4365/aa656d

Kesseli, A. Y., Kirkpatrick, J. D., Fajardo-Acosta, S. B., et al. 2019, AJ, 157, 63, doi: 10.3847/1538-3881/aae982

Kippenhahn, R., & Meyer-Hofmeister, E. 1977, A&A, 54, 539

Kleyna, J., Wilkinson, M. I., Evans, N. W., Gilmore, G., & Frayn, C. 2002, MNRAS, 330, 792, doi: 10.1046/j.1365-8711.2002.05155.x

Knigge, C., Baraffe, I., & Patterson, J. 2011, ApJS, 194, 28, doi: 10.1088/0067-0049/194/2/28

Kollmeier, J. A., Zasowski, G., Rix, H.-W., et al. 2017, arXiv e-prints, arXiv:1711.03234. https://arxiv.org/abs/1711.03234

Kosovichev, A. 2013, Geophysical and Astrophysical Fluid Dynamics, 107, 717, doi: 10.1080/03091929.2013.792633

Kraft, R. P. 1967, ApJ, 150, 551, doi: 10.1086/149359

Kraus, A. L., & Hillenbrand, L. A. 2007, AJ, 134, 2340, doi: 10.1086/522831

Lamers, H. J., & M. Levesque, E. 2017, Understanding Stellar Evolution, 2514-3433 (IOP Publishing), doi: 10.1088/978-0-7503-1278-3

Law, N. M., Kulkarni, S. R., Dekany, R. G., et al. 2009, PASP, 121, 1395, doi: 10.1086/648598

Lee, Y. S., Beers, T. C., Masseron, T., et al. 2013, AJ, 146, 132, doi: 10.1088/0004-6256/146/5/132

Levenhagen, R. S., Diaz, M. P., Coelho, P. R. T., & Hubeny, I. 2017, ApJS, 231, 1, doi: 10.3847/1538-4365/aa7681

Li, Y.-B., Luo, A. L., Du, C.-D., et al. 2018, ApJS, 234, 31, doi: 10.3847/1538-4365/aaa415

Liebert, J., Schmidt, G. D., Lesser, M., et al. 1994, ApJ, 421, 733, doi: 10.1086/173685

Livio, M., & Soker, N. 1988, ApJ, 329, 764, doi: 10.1086/166419

Lloyd Evans, T. 2010, Journal of Astrophysics and Astronomy, 31, 177, doi: 10.1007/s12036-010-0017-6

Lomb, N. R. 1976, Ap&SS, 39, 447, doi: 10.1007/BF00648343

Lowrance, P. J., Kirkpatrick, J. D., Reid, I. N., Cruz, K. L., & Liebert, J. 2003, ApJL, 584, L95, doi: 10.1086/373986

Luna, G. J. M., Sokoloski, J. L., Mukai, K., & Nelson, T. 2013, A&A, 559, A6, doi: 10.1051/0004-6361/201220792

Luna, G. J. M., Mukai, K., Sokoloski, J. L., et al. 2018, A&A, 616, A53, doi: 10.1051/0004-6361/201832592

Luri, X., Brown, A. G. A., Sarro, L. M., et al. 2018, A&A, 616, A9, doi: 10.1051/0004-6361/201832964

MacConnell, D. J. 1997, Baltic Astronomy, 6, 105, doi: 10.1515/astro-1997-0118

MacLeod, C. L., Green, P. J., Anderson, S. F., et al. 2018a, AJ, 155, 6, doi: 10.3847/1538-3881/aa99da

MacLeod, M., Ostriker, E. C., & Stone, J. M. 2018b, ApJ, 868, 136, doi: 10.3847/1538-4357/aae9eb

—. 2018c, ApJ, 863, 5, doi: 10.3847/1538-4357/aacf08

MacLeod, M., & Ramirez-Ruiz, E. 2015, ApJL, 798, L19, doi: 10.1088/2041-8205/798/1/L19

MacLeod, M., Vick, M., & Loeb, A. 2022, arXiv e-prints, arXiv:2203.01947. https://arxiv.org/abs/2203.01947

Magnier, E. A., Chambers, K. C., Flewelling, H. A., et al. 2020a, ApJS, 251, 3, doi: 10.3847/1538-4365/abb829

Magnier, E. A., Sweeney, W. E., Chambers, K. C., et al. 2020b, ApJS, 251, 5, doi: 10.3847/1538-4365/abb82c

Magnier, E. A., Schlafly, E. F., Finkbeiner, D. P., et al. 2020c, ApJS, 251, 6, doi: 10.3847/1538-4365/abb82a

Majewski, S. R., Schiavon, R. P., Frinchaboy, P. M., et al. 2017, AJ, 154, 94, doi: 10.3847/1538-3881/aa784d

Majidi, D., Forbes, J. C., & Loeb, A. 2021, arXiv e-prints, arXiv:2109.06899. https://arxiv.org/abs/2109.06899

Maoz, D., Badenes, C., & Bickerton, S. J. 2012, ApJ, 751, 143, doi: 10.1088/0004-637X/751/2/143

Margon, B., Kupfer, T., Burdge, K., et al. 2018, ApJL, 856, L2, doi: 10.3847/2041-8213/aab42a

Marigo, P., Girardi, L., Bressan, A., et al. 2017, ApJ, 835, 77, doi: 10.3847/1538-4357/835/1/77

Marshall, J. L., Burles, S., Thompson, I. B., et al. 2008, in Society of Photo-Optical Instrumentation Engineers (SPIE) Conference Series, Vol. 7014, Ground-based and Airborne Instrumentation for Astronomy II, ed. I. S. McLean & M. M. Casali, 701454, doi: 10.1117/12.789972

Martin, D. C., Fanson, J., Schiminovich, D., et al. 2005, ApJL, 619, L1, doi: 10.1086/426387

Masci, F. J., Laher, R. R., Rusholme, B., et al. 2019, PASP, 131, 018003, doi: 10.1088/1538-3873/aae8ac

Matrozis, E., Abate, C., & Stancliffe, R. J. 2017, A&A, 606, A137, doi: 10.1051/0004-6361/201730746

Matsuda, T., Isaka, H., & Ohsugi, Y. 2015, Progress of Theoretical and Experimental Physics, 2015, 113E01, doi: 10.1093/ptep/ptv148

Matt, S. P., Brun, A. S., Baraffe, I., Bouvier, J., & Chabrier, G. 2015, ApJL, 799, L23, doi: 10.1088/2041-8205/799/2/L23

Maxted, P. F. L., Heber, U., Marsh, T. R., & North, R. C. 2001, MNRAS, 326, 1391, doi: 10.1111/j.1365-2966.2001.04714.x

McGurk, R. C., Kimball, A. E., & Ivezić, Ž. 2010, AJ, 139, 1261, doi: 10.1088/0004-6256/139/3/1261

Merle, T., Jorissen, A., Van Eck, S., Masseron, T., & Van Winckel, H. 2016, A&A, 586, A151, doi: 10.1051/0004-6361/201526944

Micela, G., Sciortino, S., Serio, S., et al. 1985, ApJ, 292, 172, doi: 10.1086/163143

Michaely, E., & Perets, H. B. 2019, MNRAS, 484, 4711, doi: 10.1093/mnras/stz352

Mikołajewska, J. 2012, Baltic Astronomy, 21, 5, doi: 10.1515/astro-2017-0352

Miszalski, B., Boffin, H. M. J., & Corradi, R. L. M. 2013, MNRAS, 428, L39, doi: 10.1093/mnrasl/sls011

Moe, M., & Di Stefano, R. 2017, ApJS, 230, 15, doi: 10.3847/1538-4365/aa6fb6

Moe, M., Kratter, K. M., & Badenes, C. 2019, ApJ, 875, 61, doi: 10.3847/1538-4357/ab0d88

Mohamed, S., & Podsiadlowski, P. 2007, in Astronomical Society of the Pacific Conference Series, Vol. 372, 15th European Workshop on White Dwarfs, ed. R. Napiwotzki & M. R. Burleigh, 397

Morgan, W. W., Keenan, P. C., & Kellman, E. 1943, An atlas of stellar spectra, with an outline of spectral classification (University of Chicago Press)

Morganson, E., Green, P. J., Anderson, S. F., et al. 2015, ApJ, 806, 244, doi: 10.1088/0004-637X/806/2/244

Morrison, R., & McCammon, D. 1983, ApJ, 270, 119, doi: 10.1086/161102

Mukai, K., Ishida, M., Kilbourne, C., et al. 2007, PASJ, 59, 177, doi: 10.1093/pasj/59.sp1.S177

Munn, J. A., Monet, D. G., Levine, S. E., et al. 2004, AJ, 127, 3034, doi: 10.1086/383292

Nelemans, G., Portegies Zwart, S. F., Verbunt, F., & Yungelson, L. R. 2001, A&A, 368, 939, doi: 10.1051/0004-6361:20010049

Nelemans, G., Verbunt, F., Yungelson, L. R., & Portegies Zwart, S. F. 2000, A&A, 360, 1011. https://arxiv.org/abs/astro-ph/0006216

Neo, S., Miyaji, S., Nomoto, K., & Sugimoto, D. 1977, PASJ, 29, 249

Nissen, P. E., & Schuster, W. J. 2009, in The Galaxy Disk in Cosmological Context, ed. J. Andersen, Nordströara, B. m, & J. Bland-Hawthorn, Vol. 254, 103–108, doi: 10.1017/S1743921308027452

Noyes, R. W., Hartmann, L. W., Baliunas, S. L., Duncan, D. K., & Vaughan, A. H. 1984, ApJ, 279, 763, doi: 10.1086/161945

Ohlmann, S. T., Röpke, F. K., Pakmor, R., & Springel, V. 2016a, ApJL, 816, L9, doi: 10.3847/2041-8205/816/1/L9

Ohlmann, S. T., Röpke, F. K., Pakmor, R., Springel, V., & Müller, E. 2016b, MNRAS, 462, L121, doi: 10.1093/mnrasl/slw144

Ohsugi, Y. 2018, Astronomy and Computing, 25, 44, doi: 10.1016/j.ascom.2018.08.005

Packet, W., & De Greve, J. P. 1979, A&A, 75, 255

Paczyński, B. 1971, ARA&A, 9, 183, doi: 10.1146/annurev.aa.09.090171.001151

Paczynski, B. 1976, in Structure and Evolution of Close Binary Systems, ed. P. Eggleton, S. Mitton, & J. Whelan, Vol. 73, 75

Parker, E. N. 1955, ApJ, 122, 293, doi: 10.1086/146087

Paxton, B., Bildsten, L., Dotter, A., et al. 2011, ApJS, 192, 3, doi: 10.1088/0067-0049/192/1/3

Paxton, B., Cantiello, M., Arras, P., et al. 2013, ApJS, 208, 4, doi: 10.1088/0067-0049/208/1/4

Paxton, B., Marchant, P., Schwab, J., et al. 2015, ApJS, 220, 15, doi: 10.1088/0067-0049/220/1/15

Paxton, B., Schwab, J., Bauer, E. B., et al. 2018, ApJS, 234, 34, doi: 10.3847/1538-4365/aaa5a8

Paxton, B., Smolec, R., Schwab, J., et al. 2019, ApJS, 243, 10, doi: 10.3847/1538-4365/ab2241

Pettersen, B. R. 1989, SoPh, 121, 299, doi: 10.1007/BF00161702

Pickles, A. J. 1998, PASP, 110, 863, doi: 10.1086/316197

Placco, V. M., Frebel, A., Beers, T. C., & Stancliffe, R. J. 2014, ApJ, 797, 21, doi: 10.1088/0004-637X/797/1/21

Plez, B., & Cohen, J. G. 2005, A&A, 434, 1117, doi: 10.1051/0004-6361:20042082

Pols, O. R., & Marinus, M. 1994, A&A, 288, 475

Portegies Zwart, S. F., & Verbunt, F. 1996, A&A, 309, 179

Raghavan, D., McAlister, H. A., Henry, T. J., et al. 2010, ApJS, 190, 1, doi: 10.1088/0067-0049/190/1/1

Rappaport, S., Verbunt, F., & Joss, P. C. 1983, ApJ, 275, 713, doi: 10.1086/161569

Rau, A., Kulkarni, S. R., Law, N. M., et al. 2009, PASP, 121, 1334, doi: 10.1086/605911

Reddy, B. E., Lambert, D. L., & Allende Prieto, C. 2006, MNRAS, 367, 1329, doi: 10.1111/j.1365-2966.2006.10148.x

Ricker, G. R., Winn, J. N., Vanderspek, R., et al. 2015, Journal of Astronomical Telescopes, Instruments, and Systems, 1, 014003, doi: 10.1117/1.JATIS.1.1.014003

Ricker, P. M., & Taam, R. E. 2008, ApJL, 672, L41, doi: 10.1086/526343

Roulston, B. R., Green, P. J., & Kesseli, A. Y. 2020, ApJS, 249, 34, doi: 10.3847/1538-4365/aba1e7

Roulston, B. R., Green, P. J., Toonen, S., & Hermes, J. J. 2021, ApJ, 922, 33, doi: 10.3847/1538-4357/ac157c

Roulston, B. R., Green, P. J., Ruan, J. J., et al. 2019, ApJ, 877, 44, doi: 10.3847/1538-4357/ab1a3e

Roulston, B. R., Green, P. J., Montez, R., et al. 2022, ApJ, 926, 210, doi: 10.3847/1538-4357/ac4706

Ruan, J. J., Anderson, S. F., Green, P. J., et al. 2016, ApJ, 825, 137, doi: 10.3847/0004-637X/825/2/137

Sablowski, D. P., Järvinen, S., & Weber, M. 2019, A&A, 623, A31, doi: 10.1051/0004-6361/201834836

Sablowski, D. P., & Weber, M. 2017, A&A, 597, A125, doi: 10.1051/0004-6361/201628716

Saladino, M. I., & Pols, O. R. 2019, A&A, 629, A103, doi: 10.1051/0004-6361/201935625

Saladino, M. I., Pols, O. R., & Abate, C. 2019, A&A, 626, A68, doi: 10.1051/0004-6361/201834598

Saladino, M. I., Pols, O. R., van der Helm, E., Pelupessy, I., & Portegies Zwart, S. 2018, A&A, 618, A50, doi: 10.1051/0004-6361/201832967

Sand, C., Ohlmann, S. T., Schneider, F. R. N., Pakmor, R., & Röpke, F. K. 2020, A&A, 644, A60, doi: 10.1051/0004-6361/202038992

Scargle, J. D. 1982, ApJ, 263, 835, doi: 10.1086/160554

Scholz, F. W., & Stephens, M. A. 1987, Journal of the American Statistical Association, 82, 918. http://www.jstor.org/stable/2288805

Sharma, K., Kembhavi, A., Kembhavi, A., et al. 2020, MNRAS, 491, 2280, doi: 10.1093/mnras/stz3100

Si, J., Luo, A., Li, Y., et al. 2014, Science China Physics, Mechanics, and Astronomy, 57, 176, doi: 10.1007/s11433-013-5374-0

Singh, H. P., Gulati, R. K., & Gupta, R. 1998, MNRAS, 295, 312, doi: 10.1046/j.1365-8711.1998.01255.x

Sion, E. M., Greenstein, J. L., Landstreet, J. D., et al. 1983, ApJ, 269, 253, doi: 10.1086/161036

Skrutskie, M. F., Cutri, R. M., Stiening, R., et al. 2006, AJ, 131, 1163, doi: 10.1086/498708

Skumanich, A. 1972, ApJ, 171, 565, doi: 10.1086/151310

Smee, S. A., Gunn, J. E., Uomoto, A., et al. 2013, AJ, 146, 32, doi: 10.1088/0004-6256/146/2/32

Smith, M. C., Ruchti, G. R., Helmi, A., et al. 2007, MNRAS, 379, 755, doi: 10.1111/j.1365-2966.2007.11964.x

Smith, R. K., Brickhouse, N. S., Liedahl, D. A., & Raymond, J. C. 2001, ApJL, 556, L91, doi: 10.1086/322992

Smith, R. K., Mushotzky, R., Mukai, K., et al. 2008, PASJ, 60, S43, doi: 10.1093/pasj/60.sp1.S43

Sperauskas, J., Začs, L., Schuster, W. J., & Deveikis, V. 2016, ApJ, 826, 85, doi: 10.3847/0004-637X/826/1/85

Stellingwerf, R. F. 1978, ApJ, 224, 953, doi: 10.1086/156444

Stelzer, B., Damasso, M., Scholz, A., & Matt, S. P. 2016, MNRAS, 463, 1844, doi: 10.1093/mnras/stw1936

Tanaka, M., Letip, A., Nishimaki, Y., et al. 2007, PASJ, 59, 939, doi: 10.1093/pasj/59.5.939

Tody, D. 1986, in Society of Photo-Optical Instrumentation Engineers (SPIE) Conference Series, Vol. 627, Instrumentation in astronomy VI, ed. D. L. Crawford, 733, doi: 10.1117/12.968154

Tonry, J., & Davis, M. 1979, AJ, 84, 1511, doi: 10.1086/112569

Toonen, S., & Nelemans, G. 2013, A&A, 557, A87, doi: 10.1051/0004-6361/201321753

Toonen, S., Nelemans, G., & Portegies Zwart, S. 2012, A&A, 546, A70, doi: 10.1051/0004-6361/201218966

Torrealba, G., Catelan, M., Drake, A. J., et al. 2015, MNRAS, 446, 2251, doi: 10.1093/mnras/stu2274

Tueller, J., Gehrels, N., Mushotzky, R. F., et al. 2005, The Astronomer's Telegram, 591, 1

Tutukov, A., & Yungelson, L. 1979, in Mass Loss and Evolution of O-Type Stars, ed. P. S. Conti & C. W. H. De Loore, Vol. 83, 401–406

VanderPlas, J., Connolly, A. J., Ivezic, Z., & Gray, A. 2012, in Proceedings of Conference on Intelligent Data Understanding (CIDU, 47–54, doi: 10.1109/CIDU.2012.6382200

VanderPlas, J. T. 2018, ApJS, 236, 16, doi: 10.3847/1538-4365/aab766

VanderPlas, J. T., & Ivezić, Ž. 2015, ApJ, 812, 18, doi: 10.1088/0004-637X/812/1/18

Wallerstein, G., & Knapp, G. R. 1998, ARA&A, 36, 369, doi: 10.1146/annurev.astro.36.1.369

Warren, S. J., Irwin, M. J., Evans, D. W., et al. 1993, MNRAS, 261, 185, doi: 10.1093/mnras/261.1.185

Waters, C. Z., Magnier, E. A., Price, P. A., et al. 2020, ApJS, 251, 4, doi: 10.3847/1538-4365/abb82b

Webbink, R. F. 1984, ApJ, 277, 355, doi: 10.1086/161701

Wesemael, F., Greenstein, J. L., Liebert, J., et al. 1993, PASP, 105, 761, doi: 10.1086/133228

West, A. A., Hawley, S. L., Bochanski, J. J., et al. 2008, AJ, 135, 785, doi: 10.1088/0004-6256/135/3/785

Whitehouse, L. J., Farihi, J., Green, P. J., Wilson, T. G., & Subasavage, J. P. 2018, MNRAS, 479, 3873, doi: 10.1093/mnras/sty1622

Whitehouse, L. J., Farihi, J., Howarth, I. D., et al. 2021, MNRAS, doi: 10.1093/mnras/stab1913

Winters, J. G., Henry, T. J., Jao, W.-C., et al. 2019, AJ, 157, 216, doi: 10.3847/1538-3881/ab05dc

Wright, N. J., Drake, J. J., & Civano, F. 2010, ApJ, 725, 480, doi: 10.1088/0004-637X/725/1/480

Wright, N. J., Drake, J. J., Mamajek, E. E., & Henry, G. W. 2011, ApJ, 743, 48, doi: 10.1088/0004-637X/743/1/48

Wright, N. J., Newton, E. R., Williams, P. K. G., Drake, J. J., & Yadav, R. K. 2018, MNRAS, 479, 2351, doi: 10.1093/mnras/sty1670

Xu, X.-J., & Li, X.-D. 2010, ApJ, 716, 114, doi: 10.1088/0004-637X/716/1/114

Yan, R., Chen, Y., Lazarz, D., et al. 2019, ApJ, 883, 175, doi: 10.3847/1538-4357/ab3ebc

Yoon, J., Beers, T. C., Placco, V. M., et al. 2016, ApJ, 833, 20, doi: 10.3847/0004-637X/833/1/20

York, D. G., Adelman, J., Anderson, John E., J., et al. 2000, AJ, 120, 1579, doi: 10.1086/301513

Zorotovic, M., Schreiber, M. R., Gänsicke, B. T., & Nebot Gómez-Morán, A. 2010, A&A, 520, A86, doi: 10.1051/0004-6361/200913658

Curriculum Vitae